Semi-Inclusive Λ Electroproduction in the Target Fragmentation Region at CLAS

Jeffrey John Phillips, M.Sci.

Submitted in fulfilment of the requirements for the

Degree of Doctor of Philosophy

Nuclear Physics Group

School of Physics and Astronomy

College of Science and Engineering

University of Glasgow

October 2015

Abstract

Studies into the spin structure of the proton have been an active area of research after the EMC experiment and others found that only 30% of the total proton spin is carried by the valence quarks. Hadron production in Semi-Inclusive Deep Inelastic Scattering (SIDIS) is one way to study this phenomenon and is the focus of this thesis, which describes the measurement of the polarisation of the Lambda (Λ). Hadron production is generally examined in the Current Fragmentation Region (CFR), where the detected hadron originates from the struck quark, in terms of parton distribution and fragmentation functions. Conversely in the Target Fragmentation Region (TFR), the hadron is produced in the fragmentation of the target remnants. In this region the process is described by Fracture Functions which represent the joint probability of producing the final hadron from the target remnants when a parton of the target nucleon is struck by the virtual photon. We propose to aid in the understanding of these functions by extracting the transferred polarisation of Λ in the SIDIS electroproduction of the hadron from a proton target: $ep \to e'\Lambda X$. In this work, data recorded with the CLAS detector system at Thomas Jefferson National Laboratory during the e1f experimental run with a longitudinally polarised beam on an unpolarised target were analysed. The polarization of the Λ has been extracted by using the Maximum Likelihood Extraction (MLE) and Beam Spin Asymmetry (BSA) methods.

Contents

List of Figures

List of Tables

Chapter 1

Physics Motivation

The analysis presented here is set within the broader context of nucleon structure, which seeks to address the non-point like nature of the nucleon. This chapter presents an overview of the field, outlining the theoretical background and experimental observables describing the concepts relating to the Lambda (Λ) electroproduction in the target fragmentation region. Details relating to the significance of analysing the Λ polarisation will be given and how this connects to the specific physics formalism.

1.1 Historical Overview

The structure of the proton has been under investigation in hadronic physics since the early 20th Century, in both experiment and theory, to understand the fundamental internal structure of matter. From the early experiments that Rutherford performed, with the aid of Marsden and Geiger [1], the idea of the atomic nucleus was born with the scattering of alpha particles using thin gold sheets. The fundamental outcome was that the scattering of the alpha particles could be attributed to the hydrogen atom having a nucleus with charge +1. It was later that the term proton was coined by Rutherford himself [2].

By 1949, the list of elementary particles had grown and amongst them were the electron (e), photon (γ), neutron (n), muon (μ), pion (π), kaon (K) along with the proton (p). Each one of these was assigned quantum numbers to describe their interaction properties including charge, baryon number, spin, parity and strangeness. Conservation of quantum numbers in nuclear reactions was assumed to be a universal law. It was also proposed that all interactions are governed by four forces of nature: strong, weak, electromagnetic and gravitational.

1.1.1 Quark Model and Quantum Chromodynamics

In the mid-20th Century a series of experiments suggested evidence of unstable particles that questioned previously held assumptions. In 1951, particle track reconstruction of cosmic ray interactions revealed an obvious V-shaped track that corresponded to a neutral particle decaying into two charged particles. Later analysis of the charged particles revealed them to correspond to a proton and π^-. The underlying issue of this discovery was that the Λ particle was produced in a strong interaction but the decay time was typical of a weak decay. This discovered property is characteristic of lambda particles, thus, the newly discovered particle was termed a strange baryon.

This evidence along with others, such as Anderson and Fermi [3] [4], kindled an interest in the study of nucleon structure and models were introduced in order to understand these phenomena. In 1961, Gell-Mann and Ne'eman [5] proposed their eightfold way which was a method to classify hadrons according to charge, isospin and strangeness. It was in this model that particles with an integer charge could be members of certain groupings.

It was determined that particles could either belong to one, eight of ten member families. The baryon octet, Figure 1.1, was introduced:

1.1.1 Quark Model and Quantum Chromodynamics

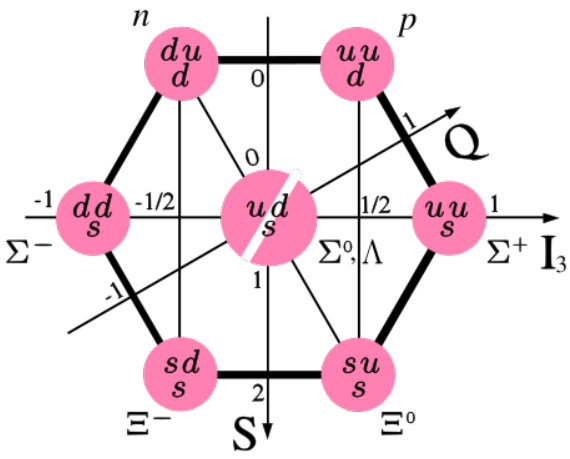

Figure 1.1: *The baryon octet. Each particle is composed of three valence quarks. Charge, Isospin and strangeness separate particles. Charge increases on axis labelled Q, and the x and y axes correspond to increasing strangeness (S) and isospin (I_3) respectively [5].*

Using this model only three fundamental particles were required to make up for and account for the quantum numbers of the baryons: up (u), down(d) and strange(s), as illustrated in Figure 1.1. Gell-Mann's work essentially led to the concept of quarks being elementary particles that formed hadrons such as the proton or Lambda (Λ). In the case of the Λ the composition was u, d, s and that of the proton (p) u,u and d. Independent work by Zweig also arrived at the same conclusion [6]. This non-point like nature of the nucleon was later supported by experimental evidence such as those at SLAC in 1966 [34].

In this eightfold way Gell-Mann constructed mesons from quark-antiquark pairs and baryons from three quarks. Within this framework they were able to model all baryons and mesons known at the time and even predict the Ω^-. The strong objection to this model was the fact that it required three identical quark combinations that were in direct contradiction of the Pauli exclusion principle. This states that no two particles with the same quantum numbers can occupy the same spin state. The answer to this puzzle was solved within the framework of Quantum Chromodynamics (QCD) which assigned colour charge (red, green and blue) to quarks and helped aid the understanding of the strong force which binds the nucleus from pos-

itively charged protons repelling against each other. The strong interaction is experienced by quark-based particles such as mesons or baryons and is mediated by gluons through the colour charge exchange. Colour in the context of QCD represents the equivalent to charge in Quantum Electrodynamics (QED). It is a property which is used to describe how the strong force interacting particles behave. The introduction of this colour charge gave quantum chronodynamics its name (QCD).

An interesting feature of QCD is known as confinement. This is a phenomenon where free quarks connot be experimentally observed [7]. This is presumed to be due to the strength of the interaction increasing as separation distance increases. For this reason, it is impossible to remove a quark from a nucleon. In addition, whilst QCD is successful in describing the strong interaction for quarks and gluons within a nucleon at high energies, complications arise when applied to a larger scale such as the interactions and properties of nucleons. Thus, unlike other couplings the strong interaction becomes weaker as the distance between interacting particles decreases, a property known as asymptotic freedom. This is demonstrated in Figure 1.2, wherein the value of the strong interaction's coupling constant (α_s) decreases as energies increase towards the perturbation region, but increases towards unity as the energy decreases to the energy scale (Q) of the nucleons [8].

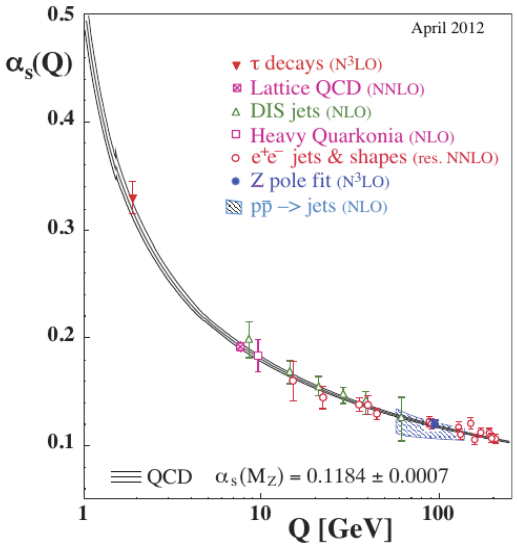

Figure 1.2: *Data for the strong coupling constant (α_s) as a function of energy scale (Q) [8].*

This prevents soft QCD processes from being solved perturbatively. Theoretical descriptions of soft hadronic processes are instead formulated using quark models, sum rules, effective field theories and lattice QCD calculations.

1.1.2 Nucleon Structure

Most of the information detailing the structure of the nucleon has been obtained from lepton-nucleon scattering. Initial theories that described the non point-like nature of the nucleon were Form Factors and Structure Functions. Form Factors measure the deviation of a nucleon from a point-like particle, therefore detailing information about the composite nature of the nucleon. For example, the electromagnetic form factors (G_E and G_M) [9] encode information on the electric and magnetic charge distributions inside the nucleon as seen through a scattering probe of resolution Q^2 (four-momentum of the probe).

There have been many results relating to form factors determined over a range of Q^2 [10] [11] [12] [13]. A surprising difference is observed when the ratio of the electric and magnetic form factors for unpolarised and polarised measurements are compared. For unpolarised results the ratio ap-

pears to be constant [14] as a function of Q^2, this is not the case in the polarised results, Figure 1.3 below.

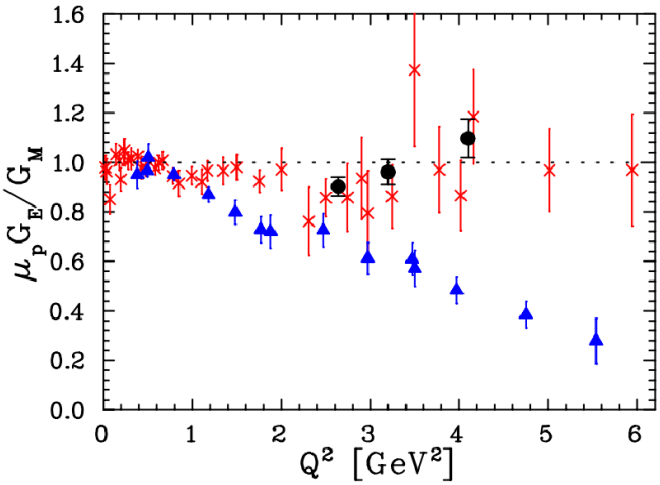

Figure 1.3: *Rosenbluth (unpolarised) (red) and polarised (blue) results for the ratio between the electric (G_E) and magnetic (G_M) form factors as a function of Q^2 [14].*

This discovery in the 1990s was termed the "Form Factor puzzle" and the reason for the disagreement is still to be resolved. Current thought is that the two-photon exchange effects usually ignored in the standard treatment of radiative corrections [15] [16] might determine the most probable explanation for the discrepancy [17] [18] [19].

As the Form Factors describe charge densities, a comparable concept for quark density distributions are introduced via structure functions. The cross-section for unpolarised inclusive Deep Inelastic Scattering (DIS), a specific type of lepton nucleon scattering experiment which will be detailed later, is a function of the structure functions W_1 and W_2. However, it is common to describe the functions in terms of the dimensionless structure functions:

$$F_1(x, Q^2) = MW_1(\nu, Q^2) \tag{1.1}$$

$$F_2(x, Q^2) = \nu W_2(\nu, Q^2) \tag{1.2}$$

1.1.2 Nucleon Structure

Where ν is the probe's energy, M the mass of the nucleon and x the longitudinal fraction of the nucleon's momentum. It is also noted in the Callan-Gross relation, which holds true for spin-1/2 particles, that the structure functions are related:

$$F_2(x) = 2xF_1(x) \tag{1.3}$$

A connection between both structure functions enables the cross section to rely on just one structure function F_2. Figure 1.4 demonstrates the structure function F_2 as a function of Q^2, measured at HERA and compared to other experiments, for different x values.

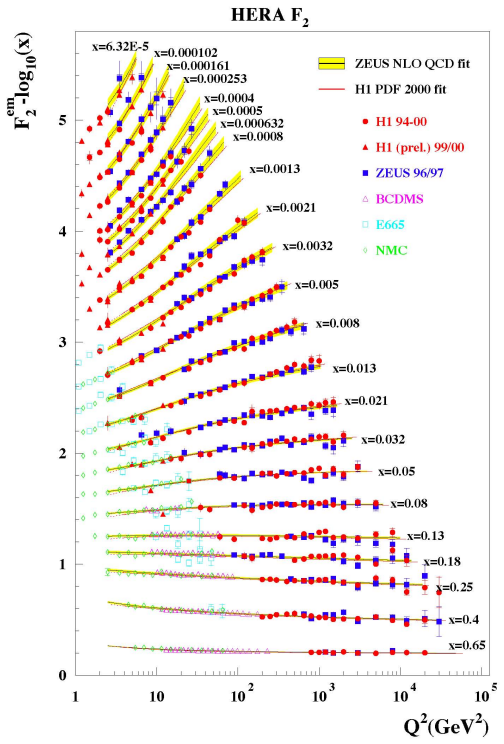

Figure 1.4: *Proton structure function F_2 measured using DIS [20].*

At values $0.08 < x < 0.4$, F_2 is relatively stable when plotted against Q^2. This was termed scaling and was predicted by Bjorken [20]. This important observation led to profoundly important conclusions about nucleon structure. As the scaling behaviour was observed experimentally it gave strong evidence for the nucleon as being made up of point-like charged particles (now identified as quarks). Also, because the Callan-Gross relation holds true for the scattering

of spin-1/2 particles, the experimental observation of this behaviour confirmed that the point like constituents of the nucleon must be spin 1/2 particles. This information give evidence for the extended picture of the nucleon structure which is currently described in terms of partons. Partons are generic descriptions of any particle constituent within the nucleon or other hadron. They can consist of quarks, as well as gluons, the force carriers of the strong force, along with a sea of quark-antiquark pairs that are constantly created and annihilated inside the hadron.

In the parton model the structure functions are related to the sum over each quark type i, charge e_q and the number densities of the partons $q_i(x)$ [21]:

$$F_1(x) = \frac{1}{2}\sum_i e_q^2 q_i(x) \tag{1.4}$$

$$F_2(x) = x\sum_i e_q^2 q_i(x) \tag{1.5}$$

Where the number densities are the parton distribution functions (PDFs) which describe the momentum distribution of the partons within the nucleon, and are later noted in the Wigner distributions.

Figure 1.5 [22] illustrates proton PDFs for partons of different flavours including gluons. It can be seen that at lower x the up and down valence quarks (u_ν, d_ν) are seen to be the main contributors. However, as x gets smaller there is an increasing contribution from sea quarks and gluons.

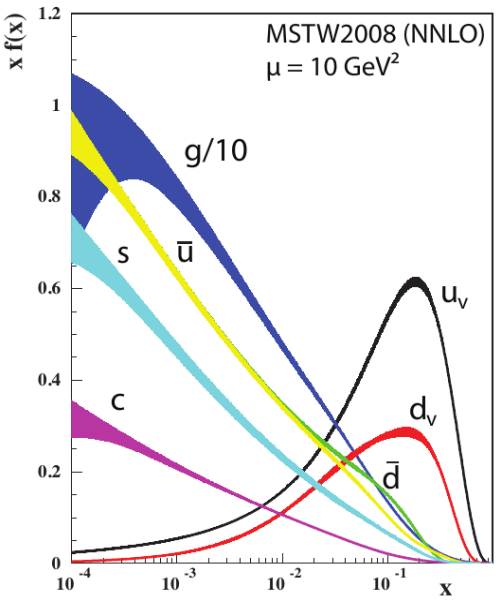

Figure 1.5: *Parton Distribution Functions (PDFs) [22].*

From the initial measurements of Form Factors and structure functions, information concerning the extended nature of the proton was revealed. Many measurements [23] [24] [25] [26] have compounded the idea of the deviation of a nucleon from a point-like particle. Parton distribution functions and Form Factors enabled a one dimensional insight into nucleon structure, however from these initial measurements a significant effort has moved into understanding a three-dimensional picture of the nucleon explained in terms of position and momentum of the partons in order to understand the true composite nature of the nucleon. These concepts will be detailed in more depth in the section on extended nucleon structure.

1.1.3 Spin Crisis

Spin is a quantum number that accounts for the portion of angular momentum that a particle has which does not arise from its orbital motion. Protons are classified as fermions, half odd integer spin particles, with quarks too being fermions. This led the assumption that the proton's spin of 1/2 was the result of the addition of the spins from the two up quarks and the down quark.

In 1987, the EMC experiment at CERN detailed the contribution of the quark spin to the total spin of the proton [27], concluding that the valence quarks contribute about 30% of the total [28] [29]. This surprising result was dubbed the "Spin Crisis". One of the major goals in the study of nucleon structure is to understand this phenomenon.

The three-dimensional structure of the proton plays an important role in understanding this phenomenon and has been the subject of experimental and theoretical work since. The three likely candidates that also contribute to the proton spin were identified. The first was the spin carried by the gluons in the proton, the second was the orbital angular momentum of the gluons and the third the orbital angular momentum of the quarks. The Jaffe and Manohar spin sum rule was one such sum rule that was conceived to illustrate the contributions of the protons spin shown in Equation 1.6 below [30]:

$$S_N = \frac{1}{2} = \frac{1}{2}\Delta\Sigma + \Delta G + L_g + \sum_q L_q \tag{1.6}$$

Where, $\Delta\Sigma$ is the contribution from the quark spin, ΔG from the gluon spin, and L_g and L_q from the gluon and quark orbital angular momentum respectively. Therefore, a substantial fraction is due to the gluon spin and orbital angular momentum components or other phenomena. The contribution of the gluon spin, ΔG, has been measured in PHENIX, COMPASS and STAR but currently is in agreement with zero [31] [32] [33]. This suggests that the orbital angular momentum of the quarks is the most likely candidate. In order to study these fundamental questions and quark orbital angular momentum, it is necessary to understand how these quarks move inside the proton in three dimensions to probe nucleon structure.

1.1.4 Facilities for Nucleon Structure Research

Previously held assumptions that the nucleon did not have extended structure were changed by experiments confirming the hypothesis that protons (and other hadrons) could be composed of much smaller point-like elements. Electron (lepton) proton scattering experiments at the

1.1.4 Facilities for Nucleon Structure Research

Stanford Linear Accelerator Center (SLAC) introduced a prominent shifting of view of hadron structure. Results from SLAC and other experiments (COMPASS, HERMES, DESY, JLAB and RHIC) [34] were important in discovering the non-interacting point-like constituents of nucleon structure and confirming that the quark spin contributed only 30%. Only within the last few decades have beam and target polarisations along with higher luminosity beams, essential for these lepton scattering experiments, become advanced enough in order to probe the kinematical regions of interest. This has enabled an increase in our understanding of nucleon structure through measurement techniques such as Deep Virtual Compton Scattering (DVCS), Deep Inelastic Scattering (DIS) or Semi-Inclusive Deep Inelastic Scattering (SIDIS). Figure 1.6 below demonstrates various facilities and the kinematical range of coverage in Q^2 and x_B (Equation 1.9). In the current analysis data is taken from CEBAF, however, with the final upgrade of CEBAF to $11GeV$ (Upgraded CEBAF) greater regions of interest will be able to be covered and explored.

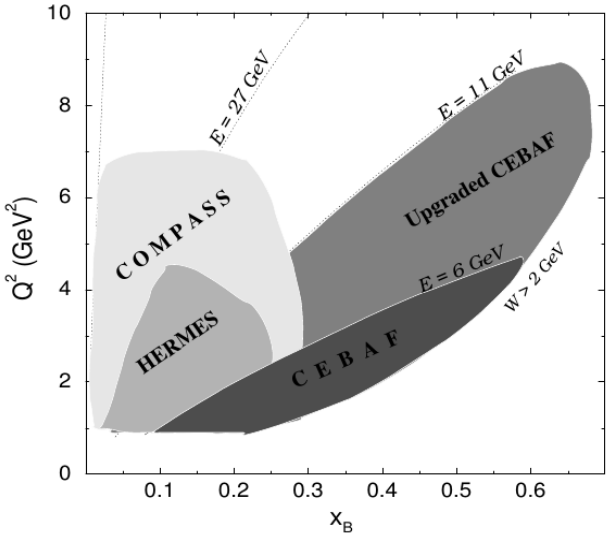

Figure 1.6: *Kinematical coverage accessible through different facilities [34].*

1.2 Extended Nucleon Structure

A more detailed description of nucleon structure in three dimensions is given in terms of the position and momentum distributions of quarks inside a nucleon. These are realised through the most general type of parton distribution: Wigner distributions or functions [35], Equation 1.7, which are functions of momentum and position distributions of partons in a nucleon. The expectation value of any physical observable can be extracted from the Wigner distribution. Due to this property it can be inferred that they encode the maximum information on the partonic structure of the nucleon. The first steps in measurements that correspond to Wigner distributions were charge, Parton Distribution Functions (PDFs) and Form Factors (FF). Form Factors are integrals of Generalised Parton Distributions (GPDs) and describe the spatial distributions of electric charge and current inside the nucleon. GPDs are intrepreted in terms of transverse postion and longitudinal momenta of partons [36].

$$W(p,x) = \int d^4\eta e^{ip\eta}\psi^*(x+\eta/2)\psi(x-\eta/2) \tag{1.7}$$

Where momentum is given by p and position by x.

However, due to the Heisenberg uncertainty principle, Equation 1.8, limits are imposed on position and momentum observations as these components cannot be known simultaneously. Hence position and momentum distribution measurements must be made separately.

$$\Delta x \Delta p \geq \frac{\hbar}{2} \tag{1.8}$$

Where Δx is the uncertainty in position and Δp in momentum.

Measurements of the parton's position in two-dimensional transverse planes, with a third in the longitudinal momentum fraction are calculated by assessing Generalised Parton Distributions (GPDs) by methods such as Deeply Virtual Compton Scattering (DVCS) and Deeply Virtual Meson Production (DVMP). Measurements of the partons three dimensional structure in mo-

mentum space are performed by accessing transverse momentum dependent parton distribution functions (TMDs) using methods such as Semi-Inclusive Deep Inelastic Scattering (SIDIS) or Drell-Yan. Collectively TMDs and GPDs are related to Generalised Transverse Momentum Distributions (GTMDS) [37] [38]. Figure 1.7 illustrates how these functions are related to each other [39].

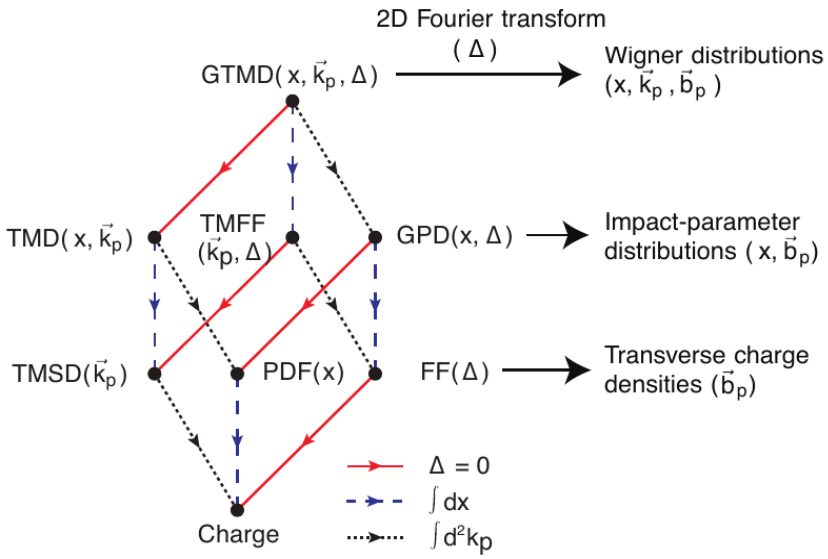

Figure 1.7: *Wigner Distributions in the context of nucleon structure and how different physical components are linked [39].*

Where, x is the longitudinal momentum fraction, Δ is the transverse momentum transferred to the nucleon, $\vec{k_p}$ is the parton transverse momentum and $\vec{b_p}$ is the position in the transverse plane defined with respect to the centre of mass of the nucleon. From Figure 1.7 it is evident that generalised transverse momentum distributions (GTMDs) would then allow access to to Wigner Distributions for partons in the proton in five dimensions (two postion and three momentum) via a Fourier transform where Δ quantifies the transfer of momentum to the nucleon $(p^{'} - p)$.

In the forward limit ($\Delta = 0$) GTMDs are the transverse momentum distributions (TMDs), with measurements of them accessible through Semi-inclusive Deep Inelastic Scattering [40]. Analogously, integrating GTMDs over the transverse momentum of partons leads to GPDs

which are probability amplitudes in longitudinal momentum space. As this is a complex field, expansions into transverse momentum spin densities (TMSDs) and transverse momentum form factors (TMFFs) are given for the reader's interest [41]. Figure 1.7 illustrates how form factors, parton distribution functions, transverse momentum dependent parton distribution functions and generalised parton distribution functions originate from the same generalised transverse momentum distribution (GTMD) which is connected to Wigner distribution by a Fourier transform.

1.3 Experimental approaches in Nucleon Structure

Most of the currently known detailed information about nucleon structure has been obtained from various types of lepton scattering experiments with different types of scattering processes accessing different aspects of the nucleon structure. An overview into some of the different type of techniques that are used to probe nucleon structure are detailed, namely, inclusive Deep Inelastic Scattering (DIS) and Semi-Inclusive Deep Inelastic Scattering (SIDIS). A description will be given into the types of kinematics observed from the methods and how these relate to the physics formalism.

1.3.1 Inclusive DIS and collinear nucleon structure

Deep inelastic scattering (DIS) [42], as mentioned previously, is a tool for probing the internal nucleon structure by scattering a lepton off a proton to investigate parton distributions. In the simplest case of DIS, the electron is scattered off the proton target and only the scattered electron is detected in the final state. In this scenario all states in the photon-nucleon system are included in the final output. Hence, this is termed inclusive and can be represented by Figure 1.8.

1.3.1 Inclusive DIS and collinear nucleon structure

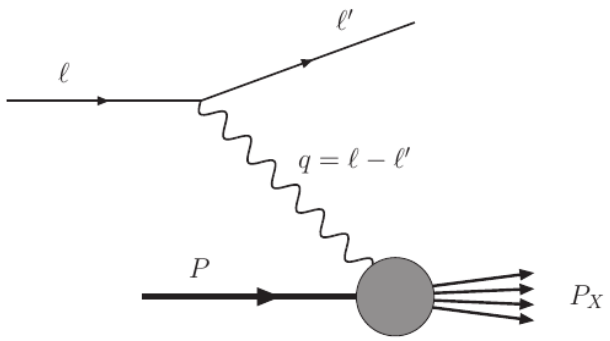

Figure 1.8: *Schematic diagram of Deep Inelastic Scattering (DIS). A lepton (l) scatters of a nucleon (p) by exchanging a virtual photon (q) with the scattered lepton (l′) measured and p_X remaining unknown.*

The remarkable results of these inclusive scattering experiments confirmed a concept known as scaling that had been predicted, as mentioned previously [43]. With regards to scaling an important parameter to consider is Bjorken-x (x_B), which is understood via the parton model [44], and equates to the fraction of the nucleon's momentum held by the struck quark in the infinite momentum frame. Bjorken-x is a variable that is used to quantify the inelastic nature of the scattering process and is given by Equation 1.9.

$$x_B = \frac{Q^2}{2p.q} = \frac{Q^2}{2M\nu} \tag{1.9}$$

Where p is the proton four-momentum, q the virtual photon four-momentum, M the mass of the nucleon and ν the virtual photon energy. In this model of DIS if you consider the infinite momentum frame, in which the momentum of the proton approaches infinity in the longitudinal direction, the invariant of the system can be described by:

$$(xp + q)^2 = x^2M - Q^2 + 2xp.q \tag{1.10}$$

where x is the fraction of the proton's momentum. In the infinite momentum frame the photon momentum remains unchanged by applying the conditions $q^2 = -Q^2$ with the invariant mass of the parton-virtual system approximately equal to zero. This implies $x = x_B$ as x^2M^2 is

much smaller than Q^2 and ν. The parton model is termed valid in the Bjorken limit which states $Q^2 \to \infty$ at finite x_B.

Results from DIS allowed the mapping of mono-dimensional momentum distributions of the individual partons by measuring parton distribution functions (PDFs). However, many aspects of the structure of the nucleon are not exposed by PDFs, as these functions are averaged over all degrees of freedom except the longitudinal component. For this reason they were termed collinear. More specifically, PDFs do not address how quarks are spatially distributed within the proton (which is essentially a three-dimensional issue). These questions have been at the heart of nucleon structure study and an effort has gone into looking at the transverse structure of the nucleon which, along with the longitudinal efforts, will allow a true three dimensional understanding of the proton structure. Techniques such as Semi-inclusive Deep Inelastic Scattering (SIDIS) enabled access into the transverse nature of the nucleon.

1.3.2 SIDIS and transverse nucleon structure

By extension of DIS, SIDIS [45] [46] is the process of scattering a lepton from a nucleon with the scattered lepton and the hadron measured and some final state particles remaining unmeasured (X):

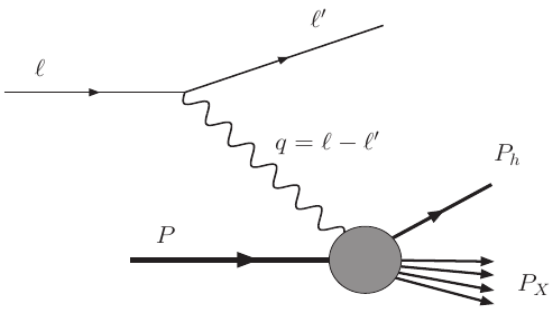

Figure 1.9: *Schematic diagram of Semi Inclusive Deep Inelastic Scattering (SIDIS). A lepton (l) scatters of a nucleon (P) by exchanging a virtual photon q. Scattered lepton (l'), produced hadron (P_h) are measured and X is unknown.*

1.3.2 SIDIS and transverse nucleon structure

Figure 1.10 below, depicts this single detected hadron case where l, l' are the initial and scattered lepton four-vectors, p is the proton (nucleon) four-vector, and p_h is the measured hadron four-vector with $p_\perp$ its transverse component. The angle between the lepton plane and the hadron (or production) plane is denoted by ϕ_h with the angle between the proton spin ($S_\perp$) and the lepton plane given by ϕ_S.

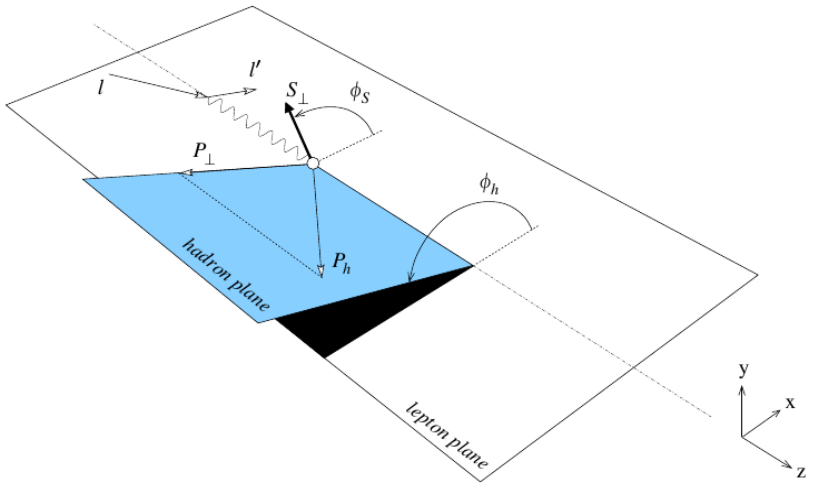

Figure 1.10: *Depiction of semi– inclusive DIS, with single – hadron production [40].*

In Figure 1.10, the incoming and scattered electrons define the electron scattering plane, while the virtual photon (q) and the scattered hadron define the production or hadron plane. The virtual photon mediating the scattering must have high energy, hence, low wavelength. Thus, allowing individual partons (quarks and gluons) to be probed, and proton structure to be analysed.

Consider the single hadron case, within the framework of SIDIS, the scattered hadron is generated by the fragmentation of the scattered quark. For such processes, the kinematics of this SIDIS process are described by the invariants [47] l, l', p and q and give rise to six lorentz invariant quantities:

1.3.2 SIDIS and transverse nucleon structure

$$l^2, \;\; p^2, \;\; q^2, \;\; p \cdot q, \;\; l \cdot q, \;\; l \cdot p \tag{1.11}$$

The initial two represent the mass of the incoming lepton (electron) $l^2 = m_e^2$ and proton $p^2 = m_p^2$ respectively. The middle two invariant quantities are used to describe the scattering process, with the third invariant derived as:

$$q^2 = (l - l')^2 = 2m_e^2 + 2(|\mathbf{l}||\mathbf{l'}|cos(\theta)) \tag{1.12}$$

Where θ is the polar angle between the lepton beam and scattered lepton. In the relativistic limit, $m_e << E$ and $E \approx l$, therefore:

$$-q^2 = Q^2 \overset{lab}{=} 4EE'sin^2(\frac{\theta}{2}) \tag{1.13}$$

The quantity Q^2 is defined as the negative squared four-momentum of the virtual photon with E and E' are incident lepton and scattered lepton energy respectively. The third invariant quantity is normalised by the proton mass m_p and illustrated as:

$$\nu \overset{lab}{=} E - E' \tag{1.14}$$

Where the energy transfer in the laboratory frame is termed ν and otherwise known as the virtual photon energy. From the last two equations the quantities Q^2 and ν can be defined such that the dimensionless variable y is introduced:

$$y = \frac{p \cdot q}{p \cdot l} \overset{lab}{=} \frac{E - E'}{E} = \frac{\nu}{E} \tag{1.15}$$

and

$$z_h \overset{lab}{=} \frac{E_h}{\nu} \tag{1.16}$$

1.3.2 SIDIS and transverse nucleon structure

Where the variables y and z_h are the fraction of the beam energy carried by the virtual photon and the momentum fraction carried by the produced hadron respectively. E and E' are incident lepton and scattered lepton energy with E_h the energy of the produced hadron system in the lab frame. The last two lorentz invariants depend on the mass of the nucleon (m_p) and the lepton variables:

$$l \cdot q = l \cdot (l - l') = m_e - (EE' - |\mathbf{l}||\mathbf{l}'|cos(\theta)) \tag{1.17}$$

$$l \cdot p = Em_p \tag{1.18}$$

In SIDIS the struck quark or remnant target quarks are ejected in the scattering process and form hadrons which are measured in the experiment. This is termed hadronization. To distinguish between the hadronization types (struck or target remnants) the variable Feynman-x (x_F) is introduced.

$$x_F = \frac{p_{||}}{p_{||}^{max}} = \frac{2p_{||}}{W} \tag{1.19}$$

Where W is the invariant mass (squared) of the hadronic state given by:

$$W^2 = (p + q)^2 = M^2 + 2M\nu - Q^2 \tag{1.20}$$

and

$$p_{||} = \frac{\mathbf{p_h} \cdot \mathbf{q}}{|\mathbf{q}|} \tag{1.21}$$

is the component of the momentum ($\mathbf{p_h}$) of the hadron parallel to the momentum of the virtual photon ($\mathbf{q}$).

1.3.3 Current and Target Fragmentation Regions (CFR, TFR) in SIDIS

As stated before the production of a hadron h in the final state from SIDIS can in principle arise from two hadronisation mechanisms: it can originate from the struck parton or from the target remnants [48], hence the cross section is:

$$\sigma = \sigma^{CFR} + \sigma^{TFR} \tag{1.22}$$

With these two contributions being represented below in Figure 1.11.

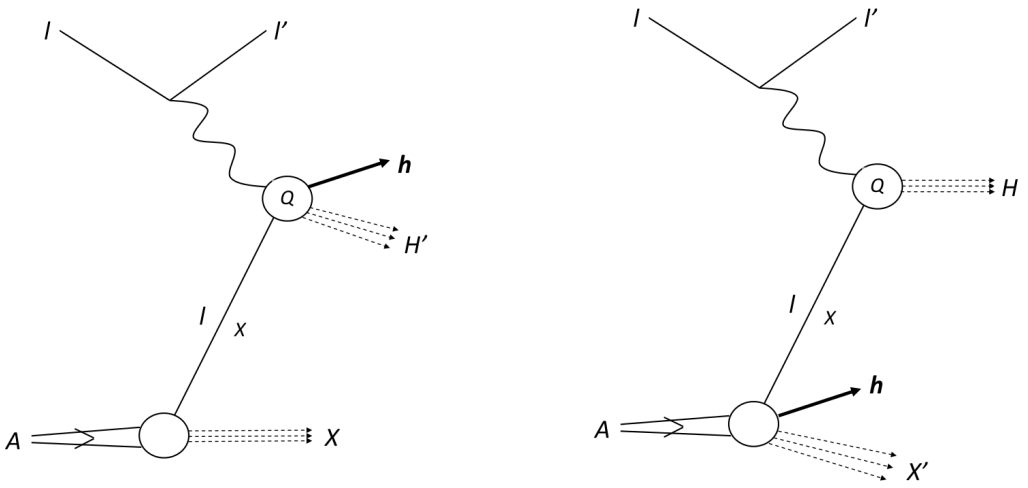

Figure 1.11: *Semi inclusive production of the hadron h in the current a) and target b) fragmentation regions [50].*

Separation of these two processes is performed by means of the Feynman variable x_F, Equation 1.19. Hadrons with $x_F > 0$ are produced in the current fragmentation region (CFR) and indicate that the produced hadron originates from the struck quark, whilst hadrons with $x_F < 0$

are produced in the target fragmentation region (TFR) and indicate that the hadron originates from the target remnant. In the current analysis the majority of the hadrons (Λ) are produced in the TFR (see Figure 3.31a later). However the cross sections in the two regions should be considered.

In the CFR the SIDIS cross section can be written in terms of Transverse Momentum Dependent (TMD) Parton Distribution and Fragmentation Functions and after integration of all the transverse momenta [49]:

$$\begin{aligned}\frac{d\sigma^{CFR}}{dx_B dy dz_\Lambda d\phi_S d\phi} = \frac{\alpha_{em}^2}{\pi Q^2 y} \sum_a e_a^2 \\ (1 - y + \frac{y^2}{2})[f_1(x_B)G_1(z_\Lambda) + S_{N\parallel} S_\parallel g_1(x_B)G_1(z_\Lambda)] \\ - (1-y)|\mathbf{S}_{N\perp}||\mathbf{S}_\perp| h_1(x_B)H_1(z_\Lambda)\cos(\phi + \phi_S) \\ + hy(1 - \frac{y}{2})[S_{N\parallel} g_1(x_B)D_1(z_\Lambda) + S_\parallel f_1(x_B)G_1(z_\Lambda)] \end{aligned} \quad (1.23)$$

Where $\mathbf{S}_N$ is the target nucleon spin and ϕ_S the azimuthal angle of its transverse component, $\mathbf{S}$ is the hadron's spin, f_1, g_1 and h_1 are the parton distribution functions, D_1, G_1 and H_1 are the fragmentation functions. The sum runs over the quark flavours a with electric charge e_a. Both the parton distribution functions and fragmentation functions will be detailed in more depth in the subsequent section.

In the Target Fragmentation Region (TFR), where $x_F < 0$, the cross section is expressed via *Fracture Functions*, which represent the joint distribution to find a parton i in the target nucleon and to produce a final hadron [50].

1.3.3 Current and Target Fragmentation Regions (CFR, TFR) in SIDIS

The SIDIS cross section can be written in the TFR as [49]:

$$\begin{aligned}\frac{d\sigma^{TFR}}{dx_B dy d\zeta d\phi_S d\phi} = \frac{\alpha_{em}^2}{\pi Q^2 y}\sum_a e_a^2 \\ (1-y+\frac{y^2}{2})[M(x_B,\zeta) + S_{N\parallel}S_\parallel M_L^L(x_B,\zeta) \\ + |\mathbf{S}_{N\perp}||\mathbf{S}_\perp| M_T^T(x_B,\zeta)\cos(\phi-\phi_S)] \\ + hy(1-\frac{y}{2})[S_{N\parallel}\Delta M_L(x_B,\zeta) + S_\parallel \Delta M^L(x_B,\zeta) \\ + |\mathbf{S}_{N\perp}||\mathbf{S}_\perp| \Delta M_T^T(x_B,\zeta)\sin(\phi-\phi_S)] \end{aligned} \quad (1.24)$$

Where the six fracture functions M, M_L^L, M_T^T, ΔM_L, ΔM^L and ΔM_T^T (for each quark flavour a) depend on the Bjorken-x(x_B) and on the variable ζ which represents the fraction of the nucleon's longitudinal energy carried by the final hadron. There are three sets of fracture functions, M, ΔM and $\Delta_T M$ for unpolarised, longitudinally or transversely polarised quarks (the latter not contributing to the process). Each fracture function has a subscript L or T for a longitudinally or transversely polarised nucleon target, and similarly a superscript referring to the final hadron polarisation. More details relating to the Fracture functions will be given in the subsequent section.

From Equation 1.23 in the CFR there is only one modulation of the type $\cos(\phi+\phi_S)$, in the TFR two modulations exist: $\cos(\phi-\phi_S)$ involving unpolarised quarks and the second $\sin(\phi-\phi_S)$ involving longitudinally polarised quarks (Equation 1.24). Thus, non-zero modulations of this type would indicate evidence of a target fragmentation process.

When neglecting the target polarisation (integrating over ϕ_S), the 4-fold differential cross section of Equations 1.23 and 1.24 can be written as [51].

$$\frac{d\sigma}{d\vec{X}} = \sigma_0(1 + hS_\parallel A_{LL}) \quad (1.25)$$

Where σ_0 is the unpolarised cross section and the spin-dependent terms expressed by the Asymmetry coefficient for the CFR and TFR are:

$$A_{LL}^{CFR} = P_B \frac{y(1-\frac{y}{2})\sum_a e_a^2 f_1 G_1}{(1-y+\frac{y_2}{2})\sum_a e_a^2 f_1 D_1} \tag{1.26}$$

and

$$A_{LL}^{TFR} = P_B \frac{y(1-\frac{y}{2})\sum_a e_a^2 \Delta M^L}{(1-y+\frac{y_2}{2})\sum_a e_a^2 M} \tag{1.27}$$

The kinematic factor $D(y) = y(1-y/2)/(1-y-y^2)$ is the depolarisation factor and accounts for the polarisation transfer from the initial electron to the virtual photon and P_B is the beam polarisation.

The cross section of both the TFR and CFR have been considered and have been shown to contain structure terms via their spin dependent terms. For the CFR these have been TMD parton distribution functions and fragmentation functions and for the TFR these have been Fracture functions. The next section will look into greater depth at the TMD structure functions.

1.3.4 TMD structure functions in SIDIS

Transverse Momentum dependent distributions (TMDs) are an important tool for studying nucleon structure. TMDs describe the distributions of quarks in a nucleon in momentum space: $f(x, k_\perp)$, which is important to understanding quark orbital angular momentum and the three dimensional nature of nucleon structure as these correspond to the momentum dependent part of the Wigner Distributions.

In the hadron production process for the CFR the cross section (Equation 1.23) is represented by (TMD) parton distribution functions (f_1) and fragmentation functions (G_1,D_1) [52] [53]. Details relating to proton structure are described by Partonic Distribution Functions (PDFs), which depend on the type of parton being struck. Information regarding the hadronization process are described by Fragmentation Functions, which depend on the type of parton be-

ing struck and the actual produced particles, demonstrated by Figure 1.12, where f are the distribution functions and D are the fragmentation functions.

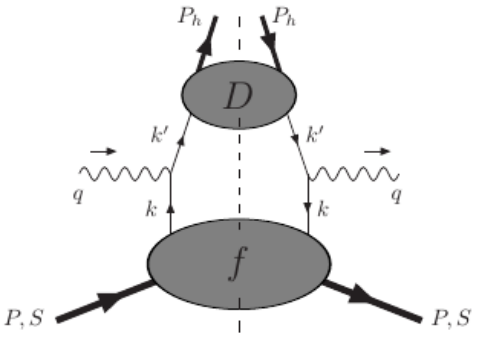

Figure 1.12: *The handbag diagram for SIDIS production of hadron in the CFR.*

There are eight TMD parton distribution functions and fragmentation functions as summarised in Appendix A. These demonstrate different combinations of nucleon or quark polarisation states.

In the hadron production process for the TFR the cross section (Equation 1.24) is represented by (TMD) via *Fracture Functions* (M), which represent the probability to produce a hadron h in the TFR when hard scattering occurs on a quark q from target nucleon, N, with fractional momentum ζ [51]. These fracture functions are illustrated below in the handbag diagram for the SIDIS production of a hadron in the TFR (Figure 1.13).

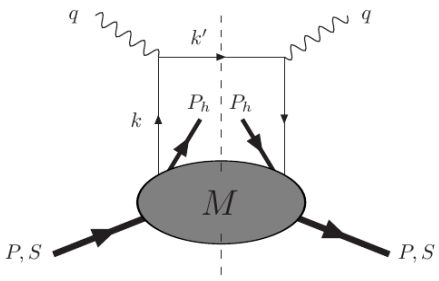

Figure 1.13: *The handbag diagram for SIDIS production of hadron in the TFR.*

1.3.4 TMD structure functions in SIDIS

The set of fracture functions for unpolarised (M), longitudinally polarised (ΔM) and transversely polarised ($\Delta_T M$) quarks for different polarisation states of the nucleon listed as subscripts, are represented in Tables 1.1, 1.2 and 1.3. These are for unpolarised, longitudinally and transversely polarised hadrons respectively in the expansion of the leading twist projections [49] [54]:

N/q	**U**	**L**	**T**
U	M	ΔM	$\Delta_T M$
L	M_L	ΔM_L	$\Delta_T M_L$
T	M_T	ΔM_T	$\Delta_T M_T$

Table 1.1: *Fracture functions for an unpolarised hadron. U,L and T represent Unpolarised, Longitudinally polarised, and Transversely polarised nucleons (rows) and quarks (columns).*

N/q	**U**	**L**	**T**
U		ΔM^L	
L	M_L^L		
T			

Table 1.2: *Fracture functions for a longitudinally polarised hadron. U,L and T represent Unpolarised, Longitudinally polarised, and Transversely polarised nucleons (rows) and quarks (columns).*

N/q	**U**	**L**	**T**
U			
L			
T	M_T^T	ΔM_T^T	

Table 1.3: *Fracture functions for a transversely polarised hadron. U,L and T represent Unpolarised, Longitudinally polarised, and Transversely polarised nucleons (rows) and quarks (columns).*

In the case of a longitudinally or transversely polarised hadron (Tables 1.2 and 1.3) only the relevant Fracture Functions noted in the TFR cross section are noted, namely: ΔM^L,M_L^L,M_T^T and ΔM_T^T [54]. Appendix B details the extended composition of these Fracture Functions.

1.4 Polarisation of the Λ with SIDIS in the TFR

This section will detail how polarisation measurements, precisely a Lambda (Λ) polarisation extraction, can relate to the Fracture Function formalism and hence allow an experimental insight into nucleon structure. As spin is a quantum number that accounts for the portion of angular momentum that a particle has, that does not arise from orbital motion, polarisation is the degree to which the angular momentum is aligned. Polarisation measurements would therefore provide a sensitive test of models of strong-interaction particle dynamics and the spin related nature of nucleon structure. A Λ measurement, in particular, is interesting due to the polarisation mainly being confined to the strange quark. This means that a Λ polarisation extraction is equivalent to s quark polarimetry [57]. Due to the composition of the Λ (u, d, s) being similar to that of the proton (u, u, d) measurements may also shed light on the spin puzzle or crisis and would also provide an important probe of the strange sea in the nucleon [55] [56]. It is for these reasons that that the current analysis of a Λ polarisation extraction in SIDIS was performed.

For baryon production, and in particular Λ, a clear excess in the yield with respect to mesons has been measured for the TFR, as shown in Figure 1.14 a). This Figure shows the normalised x_F distribution of hadrons produced in the semi-inclusive reaction $\mu + p \rightarrow \mu + h + X$ where h symbolises a π, K, p or Λ. A clear signal in the TFR [58] for Λ compared to mesons demonstrates the usefulness in analysing Λ production for studies into the TFR (and hence measurements of Fracture Functions). In addition, the comparison of the distributions of the Λ and p indicates a similar production method for both.

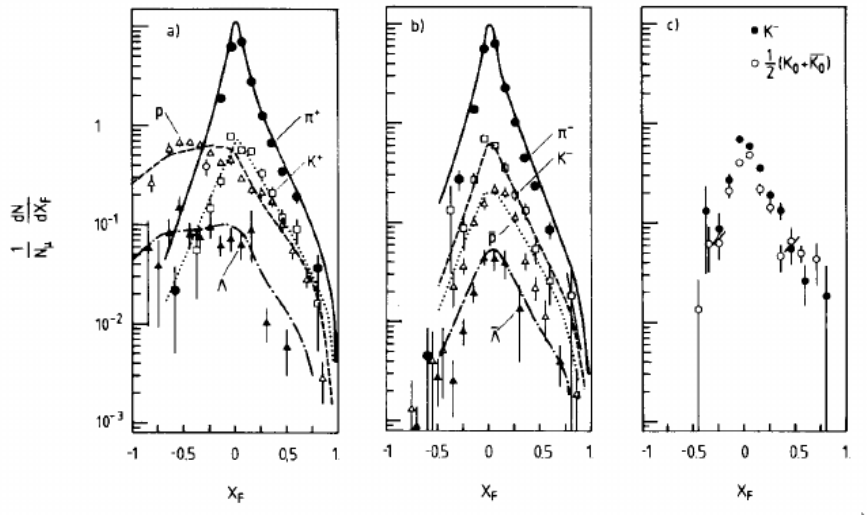

Figure 1.14: *Feynman x distributions normalised to the number of scattered muons (N_μ) for positive and negative hadrons. A) π^+, K^+, p and Λ, B) π^-, K^-, $\bar{p}$ and $\bar{\Lambda}$, C) $K^-$and$(K^0 + \bar{K^0})/2$. The curve represents the Lund Model [58].*

In terms of a polarisation extraction, the Λ baryon is a good candidate. Firstly, it is the lightest hyperon and is thus relatively easily produced. Secondly, and more importantly, the Λ decays into a proton and π^- in a parity violating weak decay. It is this decay which enables the determination of the Λ hyperon polarisation from the measurement of the angular distribution of its decay products. This is otherwise known as the Λ particle's self-analysing nature [34].

To extract the polarisation of the Λ, in its rest frame, a coordinate system is chosen with $\hat{z}$ parallel to the virtual photon direction, $\hat{y}$ normal to the electron plane and $\hat{x} = \hat{y} \times \hat{z}$ (Figure 1.15) . The advantage of this is that most of the polarisation of the virtual photon transferred to the Λ will be along $\hat{z}$.

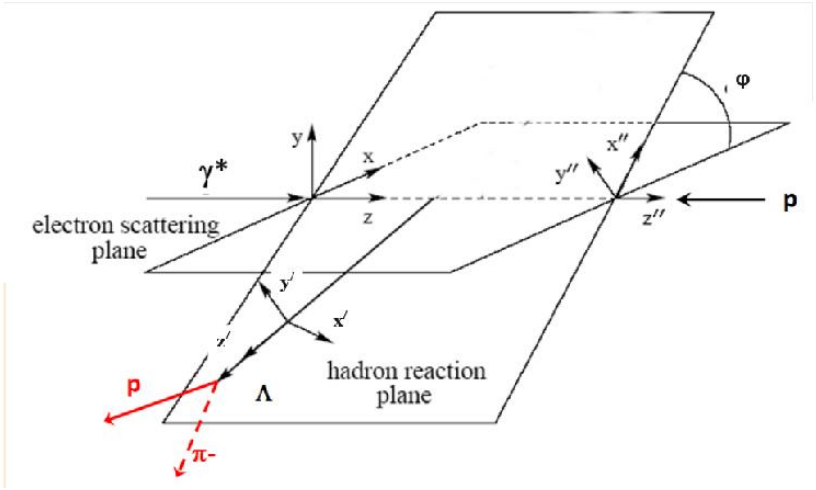

Figure 1.15: *Kinematic plane of the* $ep \to e^{'}\Lambda X$ *reaction in the* $\gamma^{*}\Lambda$ *centre of mass reference frame.*

The hadron polarisation dependent part of the SIDIS cross section can be written as [47]

$$\left(\frac{d\sigma}{d\Omega_{e'} d\Omega_{\Lambda} dE_{e'} dM_X} \propto V_{\mu} P_{\Lambda}^{\mu}\right) \tag{1.28}$$

Where $V_{\mu} = (1, V_x, V_y, V_z)$ is the spin projector and P_{Λ}^{μ} represents the Λ polarisation.

Isolating the coefficents of V_{μ}, the three components $i = x, y, z$ of Λ, the polarisation transfer can be spilt into an induced and a beam polarisation dependent part [59]

$$P_{\Lambda,i} = P_{\Lambda,i}^{I} + h P_{\Lambda,i}^{T} \tag{1.29}$$

with h the helicity of the incoming electron.

The induced component represented by:

$$P_{\Lambda,x}^{I} = C_x^{s} \sin\phi + C_x^{s2} \sin 2\phi \tag{1.30}$$

$$P_{\Lambda,y}^{I} = C_y^{0} + C_y^{c} \cos\phi + C_x^{c2} \cos 2\phi \tag{1.31}$$

$$P_{\Lambda,z}^{I} = C_z^{s} \sin\phi + C_z^{s2} \sin 2\phi \tag{1.32}$$

whilst the transferred parts are governed by:

$$P^T_{\Lambda,x} = D^0_x + D^c_x \cos\phi \tag{1.33}$$

$$P^T_{\Lambda,y} = D^s_y \sin\phi \tag{1.34}$$

$$P^T_{\Lambda,z} = D^0_z + D^c_z \cos\phi \tag{1.35}$$

All the 12 coefficients in Equations 1.30 to 1.35 are functions of relevant measurable kinematics such as Q^2, x_B etc. After integration over the azimuthal angle, the ϕ modulations average to zero and the only surviving components are the normal induced polarisation C^0_y and in the electron scattering plane the transferred polarisation D^0_x and D^0_z.

By comparison with the general expression of the Λ polarisation transfer in SIDIS, Equations 1.30 to 1.35, to the spin dependent term A^{TFR}_{LL} (Equation 1.27), we see that the only non zero term is D^0_z, all the remaining valid terms vanish after integration over the transverse momenta. Hence, unfolding from Equation 1.27 the beam polarisation and the depolarisation factor the polarisation transfer coefficient is obtained (Equation 1.36).

$$D^{LL} = \frac{\sum_a e^2 \Delta M^L}{\sum_a e^2 M} \tag{1.36}$$

This highlights how the polarisation coefficient (D^{LL}) can be related to a ratio of fracture functions in SIDIS for the production of a hadron (Λ) in the TFR.

Relatively few experiments in SIDIS kinematics have measured the polarisation transfer to Λ, see Figure 1.16 below. The NOMAD experiment [60] used neutrino beams, whilst SLAC [61], Hermes [62] and COMPASS [63] used charged lepton beams. For the Λ, NOMAD is the only experiment that explored both the TFR and CFR. It was noted that they found an increase in the polarisation transfer in the TFR ($P_\Lambda = 0.21 \pm 0.04(stat) \pm 0.02(syst)$) with respect to the CFR ($P_\Lambda = 0.09 \pm 0.06(stat) \pm 0.03(syst)$).

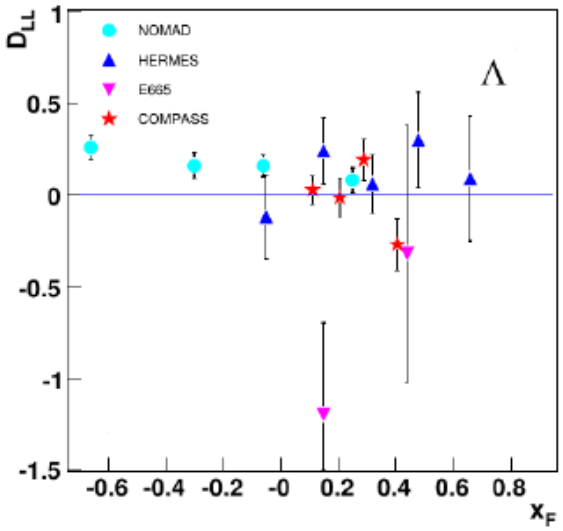

Figure 1.16: *x_F dependence in the longitudinal spin transfer to* Λ *for the COMPASS, NOMAD, SLAC and Hermes experiments [60] [61] [62] [63].*

1.5 Summary

The purpose of this chapter was to review some of the defining properties of nucleon structure and illustrate how knowledge in this field has been extended by electron scattering experiments. An overview of proton structure was given from the point of view of Wigner functions, which describe the maximum amount of nucleon structure information theoretically. From the extended structure of Wigner distributions the one-dimensional form factors and structure functions were described along with the more complete multi-dimensional concepts of Transverse Momentum Dependent distributions (TMDs) or Generalised Parton Distributions (GPDs).

Details on how we can relate these TMDs, notably Fracture Functions, to the polarisation and cross section with observable kinematics, such as x_F was given. Fundamentally, the analysis will concentrate on the following concepts:

- The spin structure of the Λ can be studied on the basis of measuring the Λ polarisation in the Target Fragmentation Region (TFR)
- Measurements of the Λ polarisation in SIDIS experiments can provide information not only on the spin structure of the different baryons, but also on the nucleon strange sea.
- As the polarisation of the Λ is mainly confined to the strange quark, it can be thought of as s quark polarimetry.
- The polarisation of the Λ can be used to understand nucleon structure through the formalism of Fracture Functions.

The remainder of the thesis will discuss the experimental set-up and target (Chapter 2) used to determine the polarisation of Λ from the technique of a Semi-Inclusive Deep Inelastic Scattering measurement. Details will be given on how the data was manipulated to describe a SIDIS measurement (Chapter 3) along with the analysis of the data with two procedures: the Beam spin Asymmetry (BSA) Method and Maximum Likelihood Extraction (MLE), Chapter 5. A Monte Carlo simulation is also performed to be used in conjunction with the data for the MLE method and to check the polarisation extraction method of the BSA (Chapter 4). Finally an overview of the results will be given with previous measurements and theoretical predictions (Chapter 6).

Chapter 2

Experimental Set-up

The analysis presented in this work was performed on data that was taken in the e1f experiment conducted at Thomas Jefferson National Accelerator Facility (JLab), Virginia, USA. This chapter commences with an overview of the facility and then continues in more detail with the sub-detector systems in Hall-B where the CLAS detector is located. Details specific to the e1f experiment will be highlighted and the equipment used to aid in the identification of charged particles, namely the proton, electron and π^-.

2.1 Jefferson Laboratory Facility

The current analysis is being performed using the e1f data set, collected between April and July of 2003, at the Thomas Jefferson National Laboratory (Hall B). Jefferson Laboratory, located in Newport News, Virginia is a US Department of Energy (DOE) nuclear research facility which has resident the Continuous Electron Beam Accelerator Facility (CEBAF). The electron beam produced by CEBAF is delivered into three experimental halls simultaneously (A, B and C), where it is used to probe the internal matter of the nucleus. One such experimental area, Hall B, accommodates the CEBAF Large Angle Spectrometer (CLAS), Figure 2.1 [64], which is a "multi-gap magnetic spectrometer equipped with drift chambers for track reconstruction, scin-

tillator counters for time-of-flight measurements, electromagnetic calorimeters (EC) to identify electrons, and Cherenkov counters (CC) for electron identification" [65].

Figure 2.1: *Photograph of the CLAS detector in Hall-B at JLab. Namely the TOF paddles and Region 3 of the Drift Chambers [64].*

2.1.1 The Accelerator

The electron beam is produced in the injector after which it is injected, with an energy of $45MeV$, into two accelerator linacs and nine recirculation arcs, Figure 2.2. The maximum beam energy achievable is about $6GeV$ with a beam spot size of $250\mu m$. This beam is produced by laser light being sent through a linear polariser before entering a pocket cell which changes the polarisation state from linear to circular. This enables the helicity to be flipped at a rate of up to $60Hz$. A half-wave plate can also be placed prior to the pocket cell to change the phase by 180°, to allow the minimisation of false systematic asymmetries. Acceleration is performed in the linacs using a series of superconducting niobium RF cavities (cryomodules, Figure 2.3) which boost the energy of the electrons as they pass. The angles of the recirculation arcs are varied to allow different energy electrons to be focussed. Magnets are used to steer the electron beam with lower energy electrons passed to the highest arc. Electrons are then focussed on lower arcs after subsequent circulations and increases in energy. Up to five passes are allowed in the accelerator facility with increases in beam energy by about $1.2GeV$ each time. After the

desired energy is reached an RF system then divides the beam into $2ns$ bunches that can be delivered simultaneously into each hall.

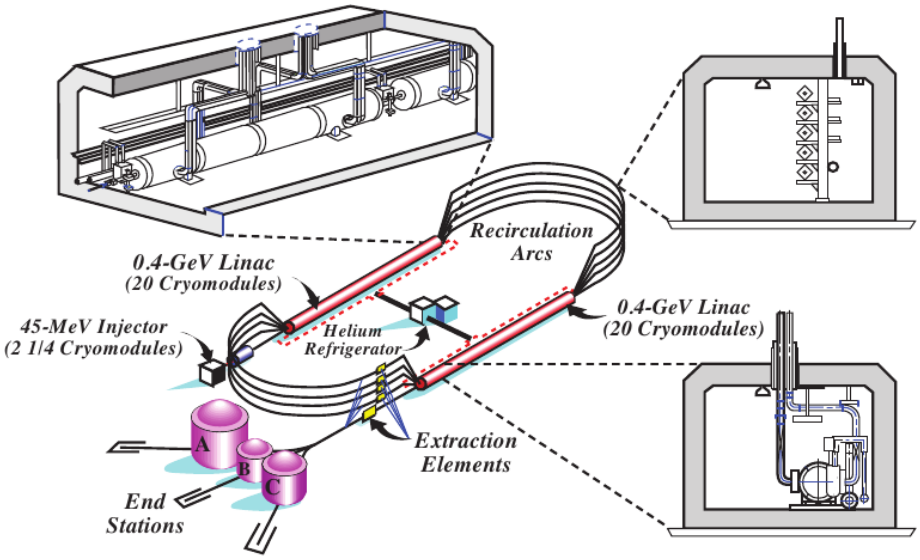

Figure 2.2: *The Continuous Electron Beam Accelerator Facility (CEBAF) [64].*

Figure 2.3: *Image of Cryomodule [65].*

2.1.2 CEBAF Large Acceptance Spectrometer (CLAS)

The CEBAF Large Acceptance Spectrometer (CLAS) is located in Hall B. This experimental set up consists of four types of detector arranged in layers to cover almost the full 4π solid angle with six independent sectors, Figure 2.4 illustrates the set up. The apparatus includes drift chambers for track reconstruction, scintillator counters for time-of-flight measurements, electromagnetic calorimeters (EC) to identify electrons, and Cherenkov counters (CC) for electron identification [65].

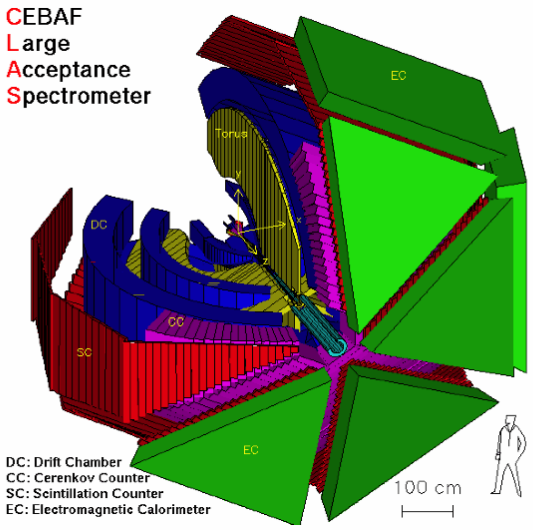

Figure 2.4: *Schematic of CLAS in Hall-B at Jefferson Laboratory*

Main Torus

The primary magnetic field of the CLAS detector, which is used for the reconstruction of charged particles and momenta, is provided by six superconducting coils [66] which produce an azimuthal magnetic field. Figure 2.5 illustrates the arrangement of the coils around the beam line. The magnetic field is calculated from the current in the coils. The coils are capable of generating magnetic fields of up to 2.5T at a maximum torus current of 3680A at forward angles compared to 0.6T at large scattering angles ($\theta = 90°$ at 3680A). The toroidal magnet

allows a magnetic field free region in the target area to enable polarised target experiments. During the e1f run period the torus magnet was set at 2250A with a polarity such that negative particles were bent toward the forward hole. Since the magnetic field is azimuthal, the tracks are only bent in the polar region (θ) while the azimuthal components (ϕ) of the particle tracks remain unchanged.

Figure 2.5: *Photograph of torus in Hall B.*

Mini Torus

In electron scattering experiments low momentum electrons can reach the inner layers of the drift chambers which will reduce the life time of the drift chambers and increase rates. This is caused by Moller scattering of electrons from the target. To combat this and improve drift chamber detection a mini-torus or small magnetic coils are located near region one of the drift chambers, Figure 2.6 (right: the mini torus magnetic field re-directs away low momentum electrons into the forward direction and out of the fiducial gaps). During the e1f run period the mini-torus current was 5995A.

2.1.2 CEBAF Large Acceptance Spectrometer (CLAS)

Drift Chambers

The purpose of the CLAS drift chambers (DC) is to determine the momentum of a charged particle by measuring the curvature of its path as the particle travels through the toroidal magnetic field [68]. The magnetic field created by the CLAS torus is approximately uniform in the azimuthal (ϕ) direction which keeps the angle constant. However, the polar angle (θ) of the particle's are affected by this magnetic field and are used to relate the particle's charge and momentum which produced the curved effect. There are three regions of drift chambers in CLAS, Figure 2.6, to aid in this particle identification procedure, each split into six sectors.

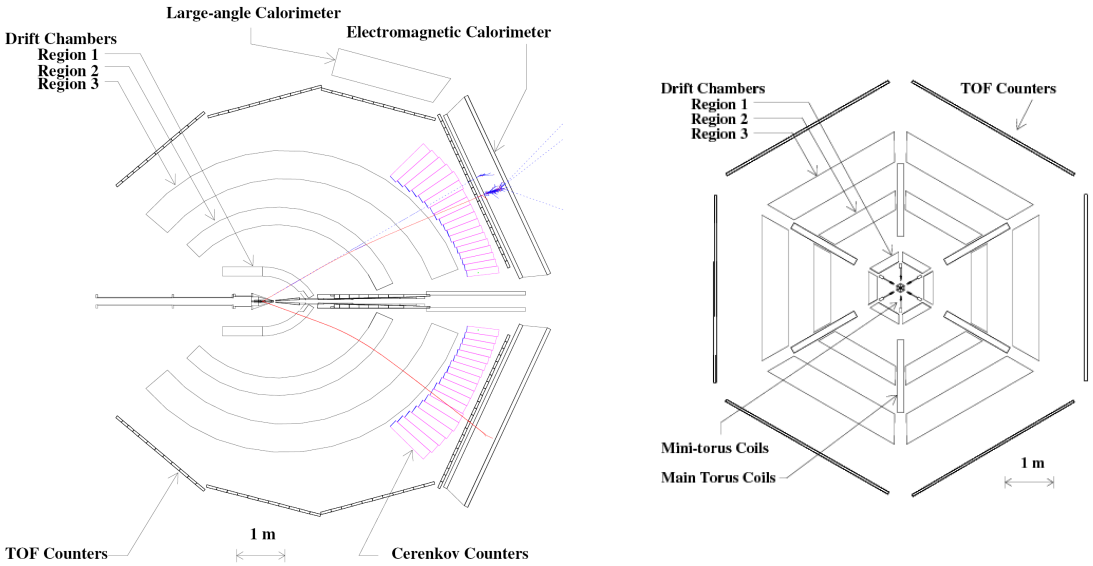

Figure 2.6: *Side view of CLAS (left) with beam line view (right).*

Equation 2.1 states how this process is achieved, where B is the magnetic field, q is the charge and ρ is the curvature of the track:

$$p = qB\rho \tag{2.1}$$

The three regions are located at different distances from the target, region 1 is closest and region 3 the furthest. Each chamber is filled with an ionizing gas (90% argon and 10% CO_2) that enables the charged particle to leave a trail of charged ions. The electric field directs the

ions to drift to a sensing wire (gold-plated tungsten with an electric field 280 KV/cm) where they are detected. Each wire in a region is aligned parallel to the adjacent wires. The sensing wires are located at the centre of a hexagon with six wires surrounding them to provide the electric field. The magnetic field lay-out is understood well which enables the path of the particle from its source to be reconstructed. Hence, the drift chambers are used in this manner to determine particle charge and momentum.

Cherenkov Counter

The CLAS cherenkov counter (CC) [69] is used primarily to discriminate between negative pions and electrons. The operation of this system is governed by the detection of Cherenkov radiation, which is produced when a particle passes through a medium with a velocity (v) faster than the speed of light (c) in that medium, Equation 2.2.

$$v > c/n \tag{2.2}$$

Where n is the index of refraction in the medium. The threshold momentum for Cherenkov radiation is dependent of the particle mass. The medium used in the CLAS CC is Per-fluorobutane C_4F_{10} which has a refractive index $n = 1.00153$. As electrons are less massive than pions, they have a smaller threshold momentum $p_e \approx 9.0MeV/c$ compared to pions $p \approx 2.5GeV/c$. Hence, if the momentum of a negatively charged particle is measured in the drift chambers to be greater than $2.5GeV/c$ and there is subsequent Cherenkov detection in the CC, this is strong indication that the particle is a pion and not an electron. Each CC sector is constructed of a light collecting cone, three adjustable mirrors and a 5-inch photomultiplier tube [70], see Figure 2.7. In addition to momentum identification, position and timing signals are also recorded in the CC. These are used in conjunction with other timing and position signals in other sub-detector systems to aid in the identification of particles.

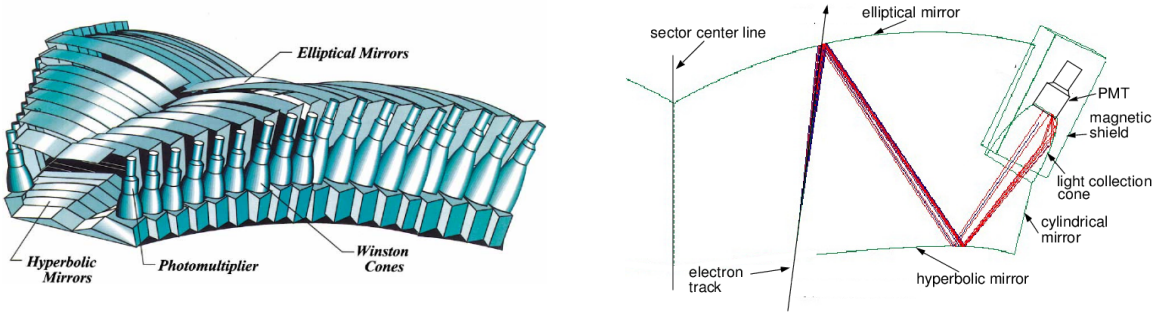

Figure 2.7: *Optical mirrors for one sector of the CC (left) and diagram of the path of an electron along with PMT (right) [70].*

Time-of-Flight

The CLAS time of flight (TOF) or scintillation Counters (SC) are used to measure the velocity of charged hadrons in CLAS [71]. They are constructed of rectangular bars of plastic scintillator material (Bicron BC-408) with photo-multiplier tubes (PMTs) at either end. They are positioned outside of the tracking system and Cherenkov Counters, but before the electromagnetic calorimeters and there are 57 paddles in each sector mounted in four panels covering the range 8° to 142°. The dimensions of the paddles are chosen to enable a timing resolution of approximately $100ps$ and allow the TOF system to operate at rates approximately $100kHz$. When a particle traverses a bar it deposits energy, which is absorbed and then re-emitted through a process of fluorescence and phosphorescence. This allows the light wavelength to be shifted in order to be in the operating range for the PMT. Thus, measurements of time and charge are used to determine the time and position of the interaction:

$$T_{start} = T_{SC} - \frac{D_{SC}}{c} \tag{2.3}$$

Where T_{start} is the start time, T_{SC} is the time of electron interaction and D_{SC} the path length from the target location to the interaction point in the SC. This enables a system with which to determine event velocities. In combination with momentum measured in the drift chamber, it is possible to determine the mass of charged particles.

2.1.2 CEBAF Large Acceptance Spectrometer (CLAS)

Electromagnetic Calorimeter

The CLAS electromagnetic calorimeter (EC) [72] is utilised for electron, photon and π^- identification. Figure 2.8 illustrates the setup. In CLAS, pions and electrons are separated by Cherenkov Counters up to $2.5GeV$. Above this threshold pions exceed the Cherenkov radiation threshold making separation not possible by the Cherenkov detector.

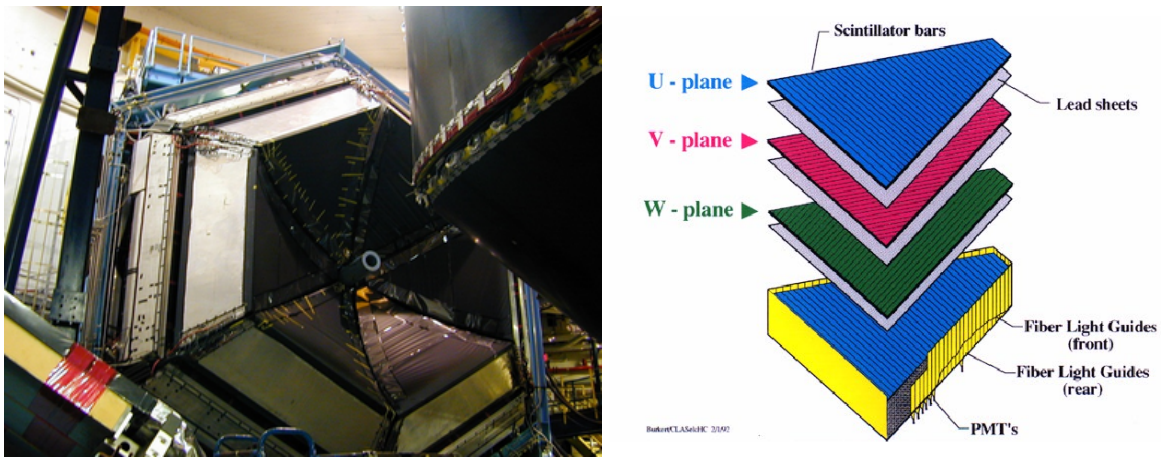

Figure 2.8: *Photograph of EC divided into U, V and W planes.*

In this instance the EC is used for separating fast moving pions from electrons. To aid in this process the EC is segmented into an inner system of about six radiation lengths and positioned in front of the target, and an outer construction part of about nine radiation lengths, positioned away from the target. The energy accumulated in these sub-systems are called EC_{inner} and EC_{outer} respectively. The EC is constructed of six independent spectrometers made up of sampling fraction calorimeters embedded with thirteen alternating layers of lead and scintillator material. The scintillating Bicstrips (36 in each sector) are arranged in three planes U, V and W. Each plane is of offset by an angle of 120° to enable triangulation of hits. Each sector consists of 39 layers, with 10mm thick BC412 scintillator subsequently followed by 2.2, thick lead. The process is detailed by photons producing particle and antiparticle pairs

and electrons decelerate in the field of the high-Z nuclei producing bremsstrahlung photons. In these instances the produced particles re-interact causing a chain effect and an electromagnetic shower of electrons, photons and positrons. The energy from this shower is deposited in the scintillator layers. In order to meet the desired resolution in energy and timing Bicron BC412 was selected. The de-excitement of visible light is then collected by PMTs. The thirteen layers of each plane are further grouped into five (inner) and eight (outer) layer stacks intended for obtaining information on the progress of showers and improving hadron identification. Electron identification is performed by comparing the energy deposited to the momentum recorded in the drift chambers. Since pions deposit approximately a fixed amount of energy ($\approx 40MeV$) by ionisation which is independent of their momentum, threshold values are incorporated for identification. Since the calorimeter can only measure a proportion of the particle's energy, as it also interacts with lead, this fraction is termed the sampling fraction (SF). This provides a method to separate events with high energy negative pions from electrons. Each sector therefore includes 36(strips) x 3(U,V and W) x 2(inner and outer parts) = 216 PMTs.

2.1.3 Trigger and data aquisition

To select and read signals from events originating from the different detector subsystems in CLAS a trigger system is employed. The CLAS event readout is initiated by a two-level trigger [66] and a trigger supervisor. The level-1 trigger operates when there is a signal above threshold in the Cherenkov counters and energy deposited in the electromagnetic calorimeters. When these conditions are met, the PMT signals are processed and used to gate PMT analogue-to-digital converters and time-to-digital converters.

The level 2 trigger attempts to find suitable tracks in the drift chambers before declaring the event valid. A decision is then based on whether to accept or reject a possible trajectory. If no possible solutions are found then the events satisfying the level 1 trigger are cleared from the trigger supervisor. The trigger supervisor produces all common start and stop signals, busy

gates, and required resets. It can be configured to require only a level 1 input or both level 1 and 2 inputs.

If possible candidate tracks are found the trigger supervisor confirms the acceptance and information is collected from the CLAS subsystems, digitally processed and sent to the Event Builder (EB). The time taken to digitise the signal and confirm the trigger is known as the dead time as no new events can be accepted. The EB then collates the information from all the CLAS subsystems into banks. This enables a complete event to be reconstructed. This event will have a unique event number, event type and identification such as run number. Groups of run numbers illustrate the portion of the data that make up one successful run. This information and those of the run conditions such as beam energy, applied high voltages etc are then passed to the Event Recorder (ER) to store the information for subsequent analysis.

2.2 The e1f experiment at Jefferson Laboratory

For the e1f experiment the electron beam was longitudinally polarised, with energy of 5.5 GeV and average polarisation, measured frequently with a Moller polarimeter, $P_b = 0.74 \pm 0.03$. Average beam current was 7nA. The electrons were scattered off a cylindrical target, 5cm long, of liquid hydrogen shown in Figure 2.9. The target was positioned 25cm upstream to the nominal centre of CLAS. The target has a diameter of 12mm (at the base) and 7mm at the downstream end. The target entrance and exit windows are $15\mu m$ and composed of Al and 4mm in diameter. Target wall contributions were removed in Z-Vertex target cuts as expressed in Section 3.2. Various target parameters are summarised in Table 2.1 which were maintained during the e1f run period.

Figure 2.9: *The e1f cryogenic target*

Temperature	$20.5K$
Pressure	$1230mb$
Length	$50mm$
Z-location	$-25cm$
Density	$0.0704g/cm^3$

Table 2.1: *Hydrogen cryogenic parameters during e1f run period.*

About 2×10^{11} total triggers were recorded, for a total integrated luminosity of about $2.1pb^{-1}$. The scattered electron and final hadrons were detected in CLAS.

2.2.1 Data calibration for e1f

Experimental data is written onto a tape silo after initial basic particle identification and trigger requirements have been met. At this point the data for the run period has to be processed or "cooked" before any analysis or event selection procedure can be initialised. All CLAS sub-detector systems have to be calibrated [67] separately by acquiring a small subset of the data in order to get better quality results. The specific calibration variables for each CLAS sub-component are saved in the CLAS calibration database.

During cooking the calibration database is accessed to apply the calibration constants and to create the necessary banks for subsequent analysis. At this stage ntuples and root trees are created which are used to extract the final information for more detailed event selections and physics analyses.

These new files are large in size, and in the case of the e1f run period, it is convenient to filter the data with pre selected events with likely particle candidates. This process is known as "skimming". These filtering scripts reduce the data files and keep events with some loose particle identification cuts. The filtering process for the e1f run period skimmed final event candidates into a positive and two negative particles, along with anything else to incorporate the semi-inclusive nature of the channel being analysed. Detailed event selections are then performed, chapter 3, before the final Λ polarisation extraction can take place. Full details of the cooking and skimming procedure can be found [73].

2.3 Summary

The experiment was carried out using the CLAS detector located in Hall B at Jefferson Laboratory. Descriptions of this facility and its sub-detector systems were presented in this chapter along with specific information relating to the target and data collection procedure for the e1f run period. In the following chapters the analysis procedure to extract a Λ polarisation from a SIDIS framework will be discussed from event selection procedures to polarisation extraction techniques.

Chapter 3

Event Selection

This chapter explains the procedure that was implemented to select a sample of events that the subsequent analysis of the extraction of Λ polarisation was conducted on. This involves identifying the three final state particles in the semi-inclusive electroproduction of Λ: $e + p \rightarrow e' + p' + \pi^- + X$. As the Λ particle is detected through its charged decay $\Lambda \rightarrow p\pi^-$, the final state contains the scattered electron and the proton and pion from the Λ decay. As the interest is in a semi-inclusive final state, no kinematic constraints are applied to clean up the event sample. For this reason, stringent identification cuts for the electrons have been applied.

Event selection commenced from the root files produced in the recooking of the whole e1f data set performed in 2008 [74] with the first event selection procedure taking the form of a skim of the data by selecting events with at least two negative and one positive charged track. As no particle identification is performed at this level, each one of the two negative tracks can be either an electron or a π^- candidate.

The subsequent particle identification and semi-inclusive cuts used to identify the reaction will be described in detail in this chapter.

The event selection procedure was performed in the following sequence:

- Fiducial Cuts.
- Event vertex cuts.
- Particle identification: Electron, proton and π^-.
- Electron and momentum corrections.
- Deep Inelastic Scattering (DIS) cuts.
- Semi Inclusive Deep Inelastic Scattering (SIDIS) cuts.
- Λ identification.

3.1 Fiducial cuts

A set of standard functions [75] for selecting regions with flat acceptance has been developed for the e1f data set. These functions have been applied to the final electron and the two hadrons.

Particle detection in CLAS is dependent upon the geometry and layout of the detector and its efficiency is illustrated by the kinematics of the particles i.e. momentum, azimuthal angle and polar angle. This is highlighted if a showering particle reaches the EC near to the edges. In this circumstance some of the shower generated in the calorimeter by the particle can escape the detection of the EC. Thus, energy detection will be incomplete.

In addition, in the CC a similar circumstance to inefficient region coverage as in the EC are noted. In these regions the optical system of light collection does not focus well the Cherenkov light on the PMT, see Figure 2.8. This ultimately reflects poor particle identification in these regions. In both cases these are described through fiducial loss regions. In CLAS particle detection efficiency is calculated using GEANT [76] and GSIM [77]. GSIM, chapter 4, is a detector simulation program that evaluates CLAS detector geometry and response to different charged particles. However, for fiducial loss regions GSIM and CLAS can have discrepancies.

Therefore, to avoid regions where CLAS response cannot be reliably reproduced by simulation fiducial volumes are created. In addition to dead detector areas different types of charged particles have different fiducial regions depending on the charge of the particle track in the magnetic field (out-bending or in-bending).

For determination of the fiducial volume it is common to express the regions by the azimuthal (ϕ) and polar (θ) angles. For this analysis three detected particles in the final state i.e p, e^- and π^- are considered for fiducial region selection.

3.1.1 Electron Geometrical Fiducial Cuts

Geometric fiducial cuts are employed to render regions of the detector that do not have flat acceptance, and hence low efficiency, redundant. These cuts are applied to all final state particles and depend on momentum. These so called redundant fiducial volumes for the electron are specified by applying cuts in the detector on ranges of polar (θ) and azimuthal (ϕ) ranges. Standard electron geometric fiducial cuts are defined by [78]:

$$\theta_{min} = \frac{\theta_1 + \theta_2}{(p_e + p_0)\frac{I_{max}}{I}} \tag{3.1}$$

$$\Delta\phi_e = \phi_0 \sin(\theta - \theta_{min})^x \tag{3.2}$$

$$x = \alpha(p_e \frac{I_{max}}{I})^\beta \tag{3.3}$$

Where for the e1f run period $I_{max}/I = 1.5$ and $I = 2250A$ and p_e was the electrons momentum. To minimise the loss of statistics only lose fiducial cuts were employed in the e1f run period. A list of parameters in the above equations are given in Table 3.1.

3.1.1 Electron Geometrical Fiducial Cuts

Parameter	Electon FC values
θ_1	9.5
θ_2	26.0
p_0	0.5
ϕ_0	24.0
α	0.01
β	1.2

Table 3.1: *List of parameters for electron geometrical fiducial region cuts given in Equations 3.1-3.3. All Momenta are in GeV and angles in degrees.*

In addition to the above mentioned cuts, inefficient or faulty scitillator paddles were also taken into account as they were not reliable [79]. These are listed in Table 3.2.

Sectors	Non-reliable SC paddles
1	24
2	16, 18
3	2, 11, 22, 27, 28, 40
4	19, 30, 34
5	7, 18, 20
6	1, 18, 40

Table 3.2: *List of non-reliable SC paddes by sector.*

Figure 3.1 demonstrates the above mentioned fiducial cuts for the electron illustrating its polar (θ) and azimuthal (ϕ) region coverage before geometrical fiducial cuts and after. Non-working SC paddles explain the variation between sectors for low θ events.

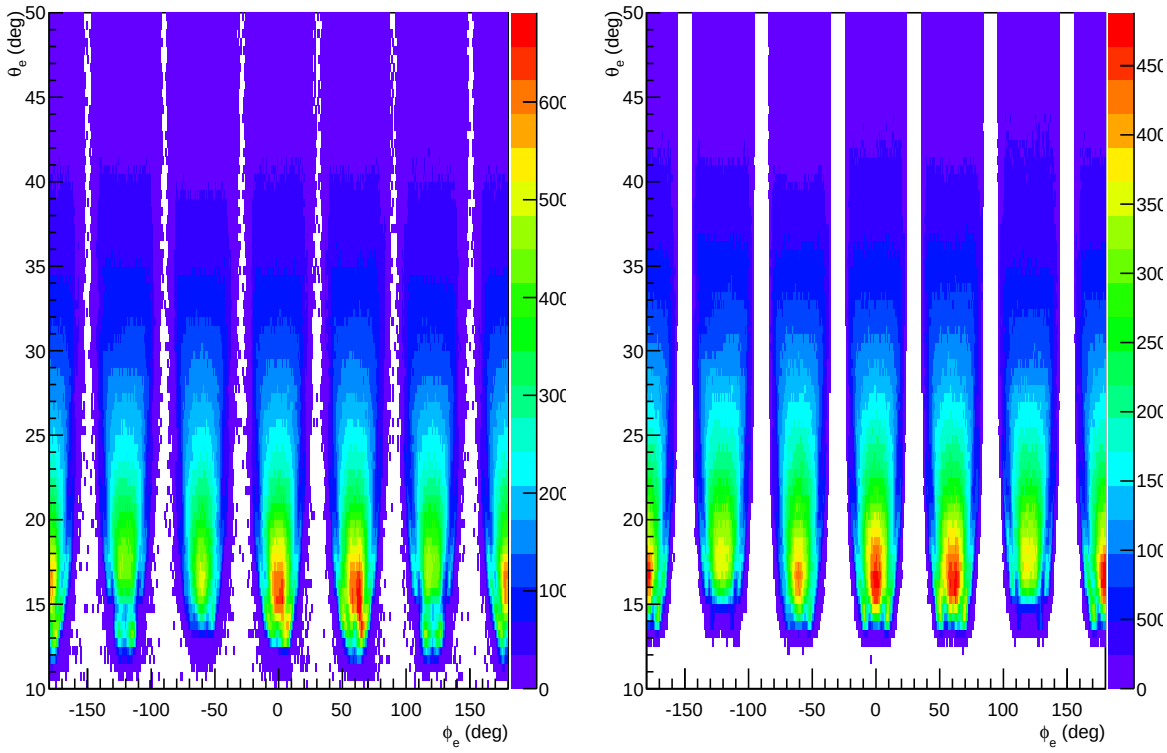

Figure 3.1: *Polar(θ) and Azimuthal (ϕ) angle coverage of the electron for the 6 CLAS sectors before (left) and after (right) geometrical fiducial cuts*

3.1.2 Electromagnetic Calorimeter Fiducial Cuts

As described before, the EC is used for particle identification, namely to allow separation of electron and pion candidates for energies greater than 2.5 GeV (at lower energies the CC is employed). This is to create a clean confinement of showering particles in the EC fiducial volume i.e. in the region that has greatest efficiencies. The procedure implemented in this fiducial region cut ensured that the electromagnetic shower centroid appears at least 10cm away from the U, V and W plane edges [80].

3.1.2 Electromagnetic Calorimeter Fiducial Cuts

The selection areas were:

$$20 \leq U_{EC} \leq 400cm \tag{3.4}$$

$$V_{EC} \leq 375cm, \tag{3.5}$$

$$W_{EC} \leq 410cm \tag{3.6}$$

An example of these fiducial cuts is illustrated in Figure 3.2 which demonstrates the Y and X distributions of the electrons on the calorimeter surface before and after EC fiducial cuts.

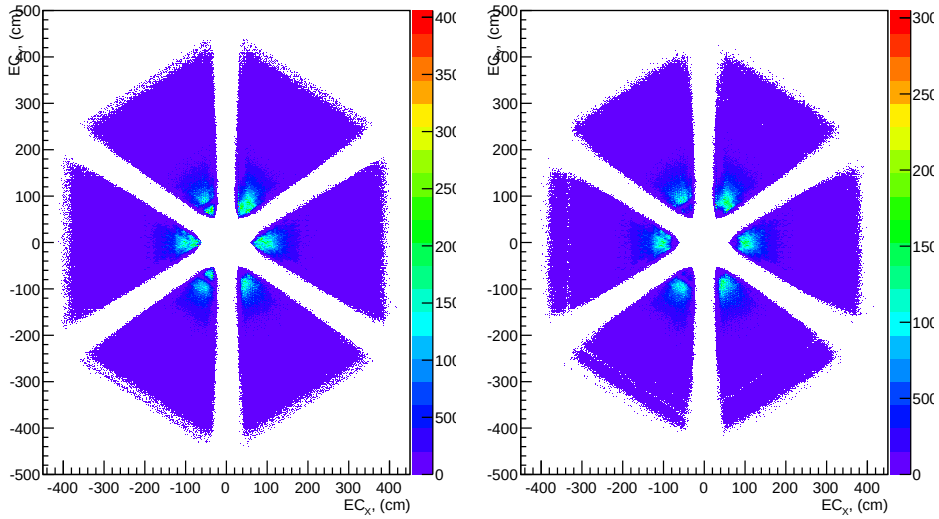

Figure 3.2: *Electron Y vs X distributions projected onto the calorimeter surface. This is before (left) and after (right) Electromagnetic Calorimeter fiducial cuts.*

Figure 3.3 represents the polar (θ) and electron momentum (P_e) distributions as a function of the CLAS sectors, before and after EC fiducial cuts . These illustrate both the electron geometrical and EC calorimeter fiducial region acceptance volumes for areas of flat acceptance for the electron.

3.1.2 Electromagnetic Calorimeter Fiducial Cuts

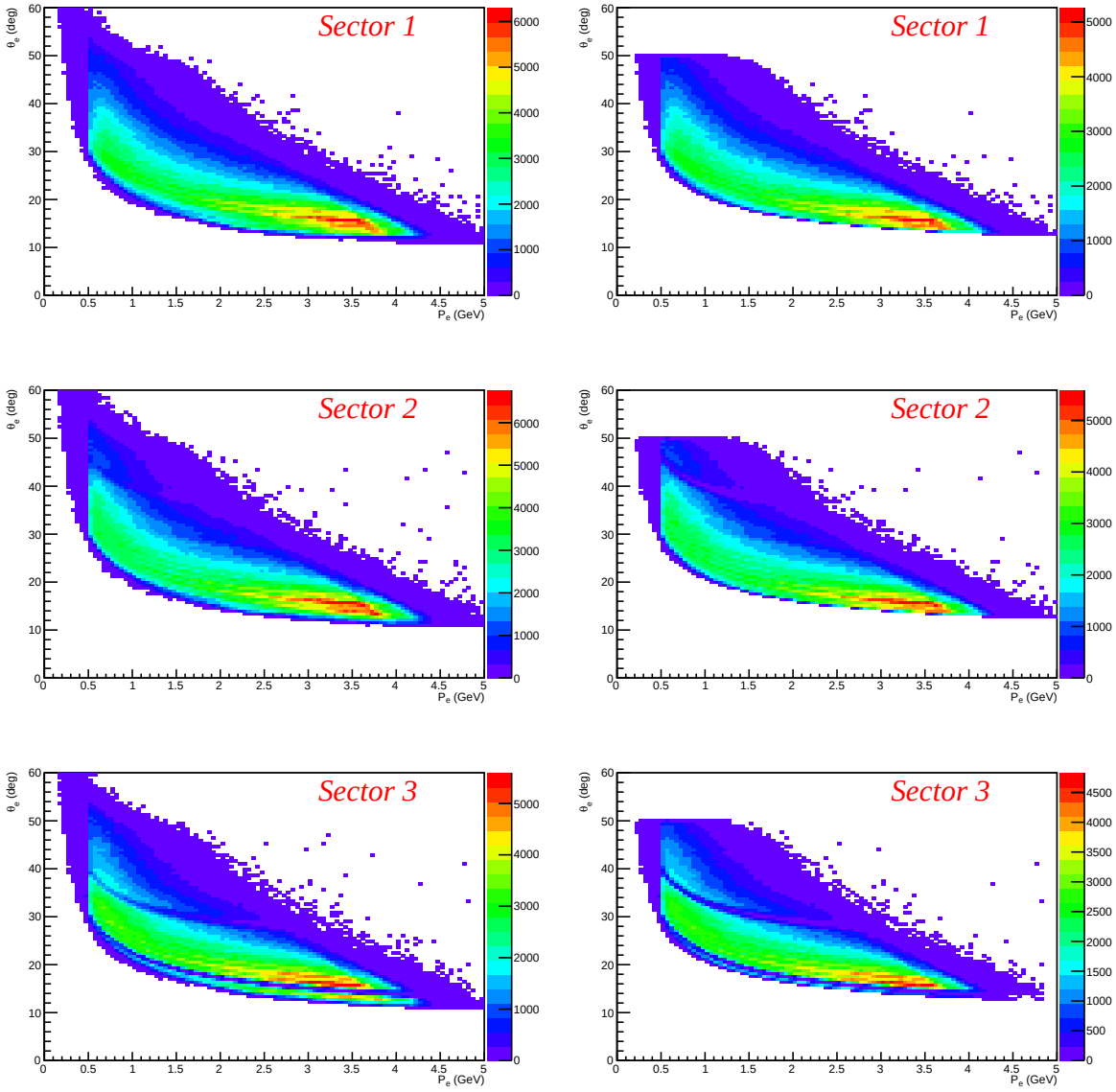

Figure 3.3: *Electron polar (θ) angles against momentum (P_e) for CLAS sectors 1 to 3. This is before (left) and after (right) Electromagnetic Calorimeter and electron fiducial cuts.*

3.1.3 Hadron Geometrical Fiducial Cuts

Hadron geometrical fiducial cuts are employed to remove low-acceptance volumes in CLAS, thus, improving detector efficiency and reliability in particle reconstruction for hadrons. This selection process is performed to the proton and π^- and is momentum dependent. The same process is performed as in the electron geometrical fiducial cuts i.e selecting a fiducial volume by specifying specific ranges on the polar(θ) and azimuthal(ϕ) angles of the hadron. The procedure to implement these geometrical fiducial cuts are given by the following expressions:

$$\theta_{min} = \theta_0 + \theta_1(\frac{P_h}{c}\frac{I_{max}}{I})^d \tag{3.7}$$

$$\Delta\phi_h = \phi_0 \sin(\theta_h - \theta_{min})^x \tag{3.8}$$

$$x = \alpha(P_h\frac{I_{max}}{I})^\beta \tag{3.9}$$

Where P_h is the hadrons momentum, θ_h and ϕ_h its polar and azimuthal angle respectively. For the e1f data set $I = 2250A$ so that $I_{max}/I = 1.5$. A list of the parameters for the hadron geometrical fiducial cuts are given in Table 3.3. Similar cuts for e1f experimental data are found at [81] [82].

3.1.3 Hadron Geometrical Fiducial Cuts

Parameter	**proton FC values**	π^- **FC values**
θ_0	4.0	6.0
θ_1	20.0	20.0
d	15.0	15.0
α	0.22	0.22
c	8.0	8.0
ϕ_0	32.0	30.0
β	0.15	0.15

Table 3.3: *List of parameters for hadron geometrical fiducial region cuts given in Equations 3.7-3.9. All Momenta are in GeV and angles in degrees.*

Figure 3.4 illustrates the polar (θ) against azimuthal (ϕ) distributions for the proton (a) and the π^- (b), before and after geometrical hadron fiducial region cuts. Non-working SC paddles explain the variation between sectors for low θ events.

3.1.3 Hadron Geometrical Fiducial Cuts

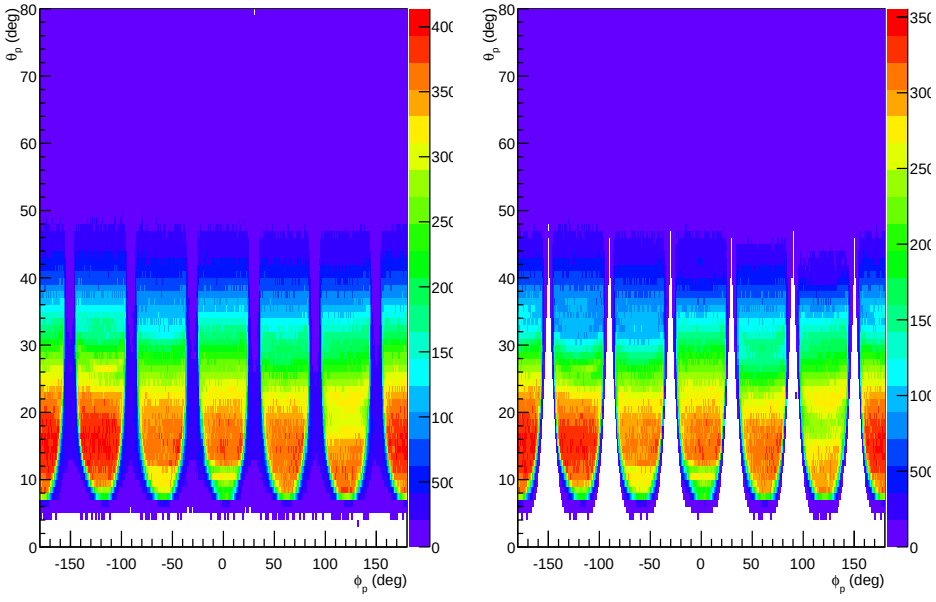

(a)

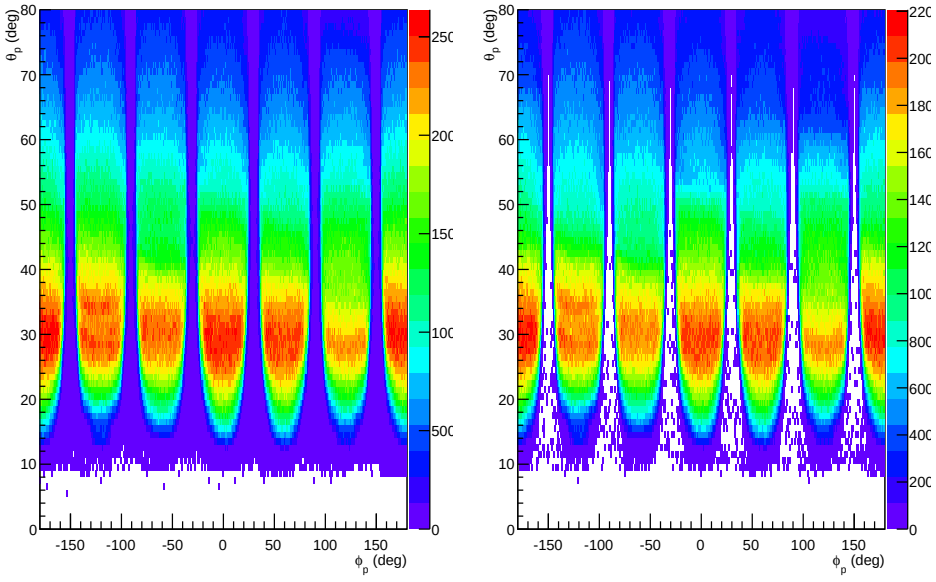

(b)

Figure 3.4: *Proton (a) and pion (b) polar (θ) angles against azimuthal (ϕ) for all CLAS sectors. This is before (left) and after (right) hadron geometrical fiducial cuts.*

3.1.3 Hadron Geometrical Fiducial Cuts

Figure 3.5 illustrates θ against momentum for the proton before and after geometrical fiducial region cuts for certain CLAS sectors with Figure 3.6 the π^-.

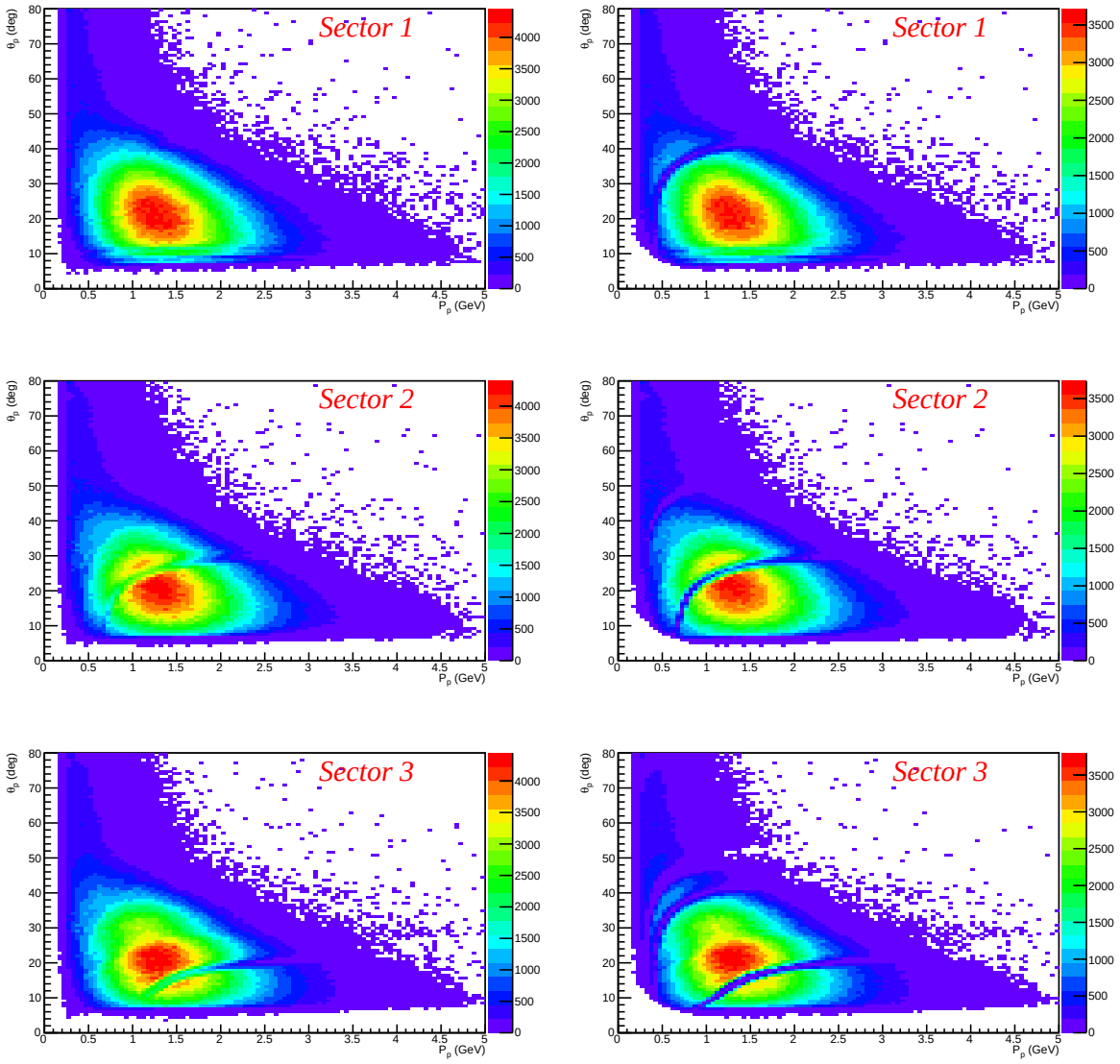

Figure 3.5: *Proton polar (θ) angle against momentum (P_p) for CLAS sectors 1 to 3. This is before (left) and after (right) hadron geometrical fiducial cuts.*

3.1.3 Hadron Geometrical Fiducial Cuts

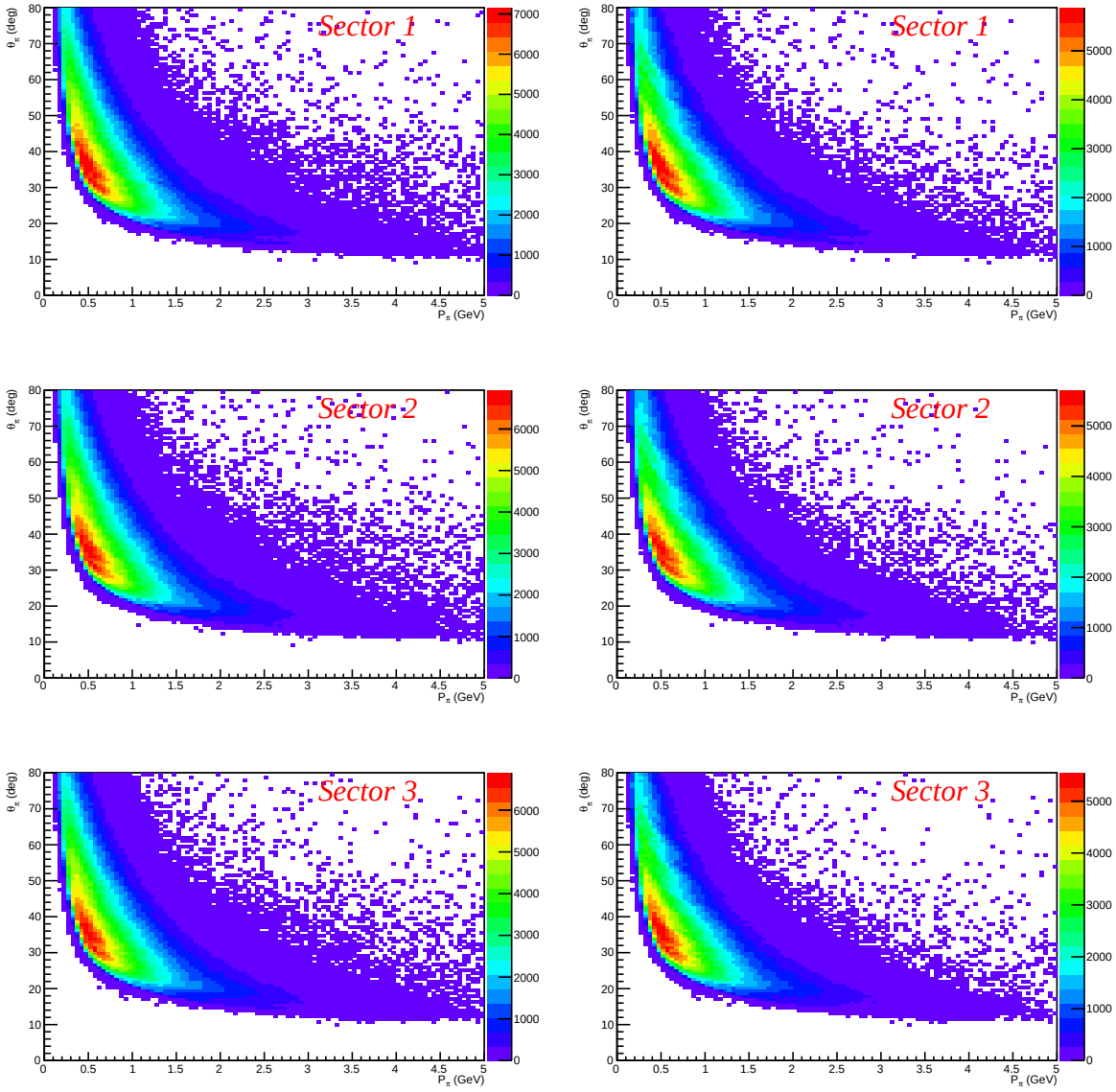

Figure 3.6: *π^- polar (θ) angle against momentum (P_{π^-}) for CLAS sectors 1 to 3. This is before (left) and after (right) hadron geometrical fiducial cuts.*

3.2 Event Vertex reconstruction

The primary interaction vertex is reconstructed by calculating the mid point between the scattered electron track provided by the drift chambers (DC) and the beam line. The beam line has been calculated, run by run, making use of the electrons scattered off the beam exit window about 25cm downstream of the target. In Figure 3.7, an example of the distribution of the z component of the electron, (V_z), of the DC electron vertex is shown for the 6 CLAS sectors. Small discrepancies among the sectors are due to the small displacement of the beam line from the nominal transverse position $(0, 0)$ used in DC reconstruction. This issue was solved by evaluating the precise position (X,Y) of the beam run by run.

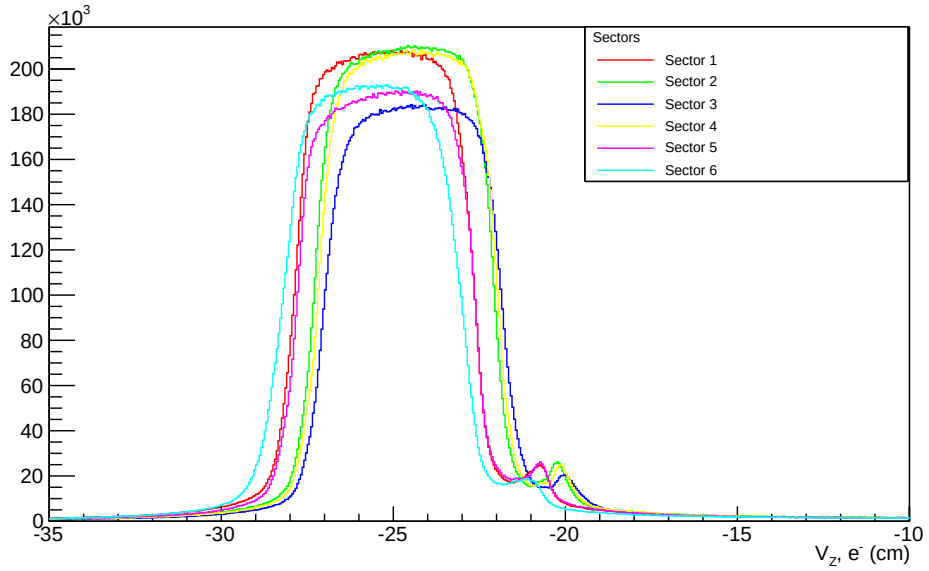

Figure 3.7: *The z component of the Electron, V_z, for the 6 CLAS sectors. Shoulder to the right is due to the Aluminium clamps on the exit window.*

The electron V_Z sector dependent cuts were evaluated by fitting the sector dependant distributions (Figure 3.7) with half-Gaussians at each edge, and the cut values chosen to be $+/-3\sigma$ from the mean. The final sector dependent cuts on the reconstructed electron z-vertex V_z are shown in Table 3.4 and illustrated in Figure 3.8.

Sector	V_z cut min (cm)	V_z Cut max (cm)
1	-28.5	-21.9
2	-27.5	-21.0
3	-27.25	-20.5
4	-27.5	-21.0
5	-28.5	-21.5
6	-29.25	-22.0

Table 3.4: *List of electron Z-Vertex cut values to ensure measured scattered electron is from the target region.*

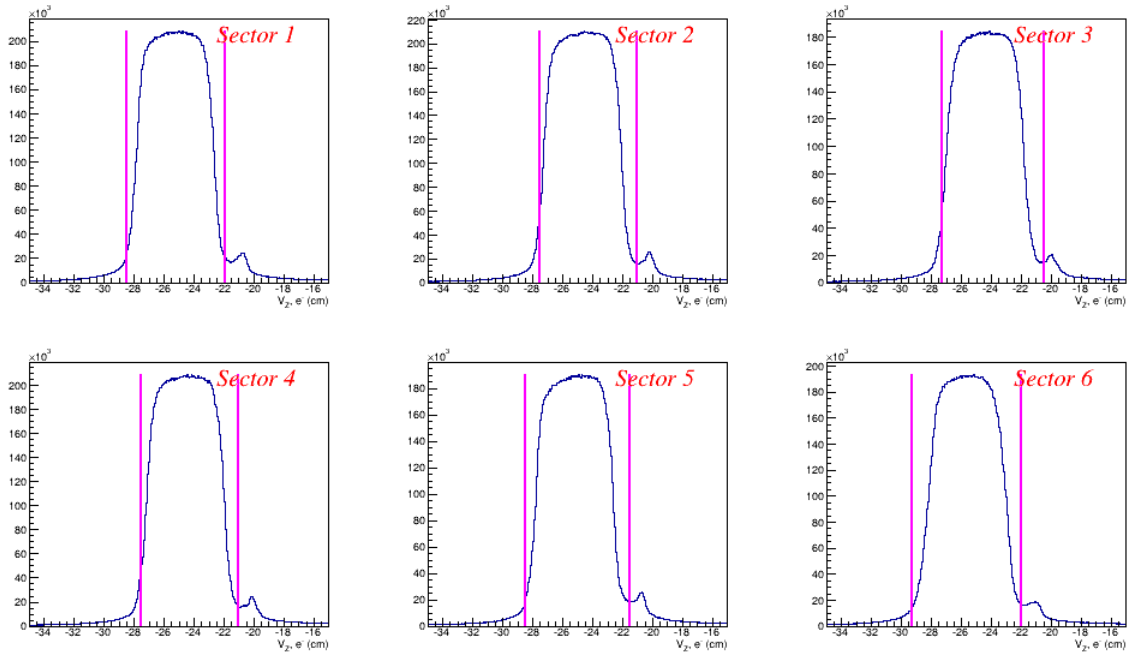

Figure 3.8: *The z component of the Electron, V_z, for the 6 CLAS sectors with the magenta lines indicating the z-vertex cuts on the electron. Shoulder to the right is due to the Aluminium clamps on the exit window.*

3.3 Particle Identification

The final state particles in the reaction $e + p \rightarrow e' + p' + \pi^- + X$ were identified by applying further particle data cuts to the sample. The particle identification procedure was performed on the data set in the following order:

- selection of exclusive events.
- electron identification: Cut on the number of photoelectrons in the CC.
- electron identification: EC energy cuts.
- proton mass cuts.
- π^- mass cuts.

For the particle identification cuts stated above an exclusive channel has been employed, in this case all final state particles are identified. This was used to aid in particle identification as there would be no unknown (X) contributions, like in the semi-inclusive channel, and thus particle identification would be cleaner.

3.3.1 Selection of $ep \rightarrow ep\pi^-(\pi^+)$ events

From the skimmed event with two negative and one positive track, all possible assignment of the $ep \rightarrow ep\pi^- X$ have been performed. Fiducial cuts as well as the target vertex cuts have been applied. The resulting missing mass distribution is shown in Figure 3.9.

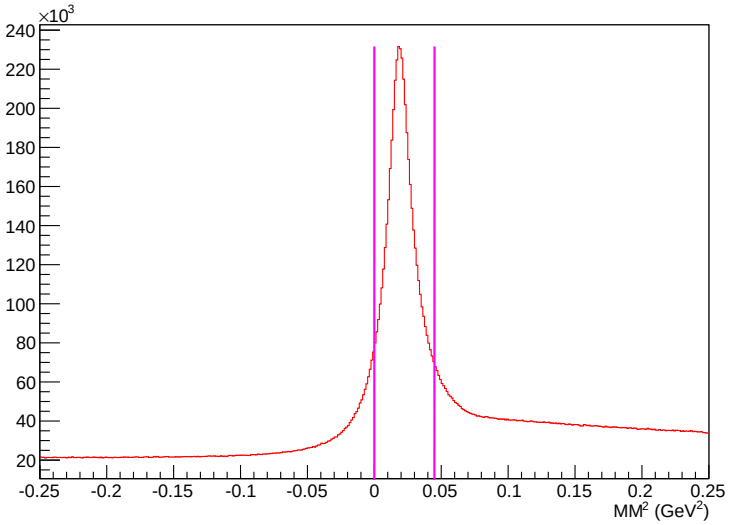

Figure 3.9: *Missing mass distribution for* $ep \rightarrow ep\pi^-(\pi^+)$

From the Missing Mass squared plot, Figure 3.9, the π^+ exclusive cut is:

$$0.0 \leq MM^2 \geq 0.045(GeV^2) \tag{3.10}$$

Selecting this missing mass region enables the $\pi+$ to be identified instead of the previously unknown (X) component in SIDIS, Equation 3.11. This allows an exclusive channel to be selected which was used primarily for electron/pion separation.

$$ep \rightarrow ep\pi^-(\pi^+) \tag{3.11}$$

3.3.2 Electron Identification

The main background in the particle identification stage arises from negative pions misidentified as electrons. As the initial skim of the data selected two negative particles, mentioned previously, these could include either an electron or a π^-. Thus, a set of cuts to separate electrons from pions in the signals in the Cherenkov Counter (CC) and the Electromagnetic Calorimeter (EC) produced by electrons and pions have been analysed.

3.3.2 Electron Identification

Cherenkov Counter

The CC signals generated by electrons and pions from the exclusive channel (Equation 3.11) were compared. The distributions of the number of photoelectrons detected in the CC for electrons (red histograms) and pions (blue histograms) are illustrated in Figure 3.10 for the 6 CLAS sectors. The vertical magenta line shows the normal cut $N_{pe} > 2.5$ used to separate electrons from pions. A loose cut was applied to the Cherenkov as a non negligible fraction of good electrons and at the same time pions can produce a large number of photoelectrons in the CC. For this reason, the only requirement for the electron identification is (Similar cuts for e1f experimental data are found at [81] [82]):

•*CC cut* : $N_{pe} > 2.5$ *in the same sector of the DC track.*

3.3.2 Electron Identification

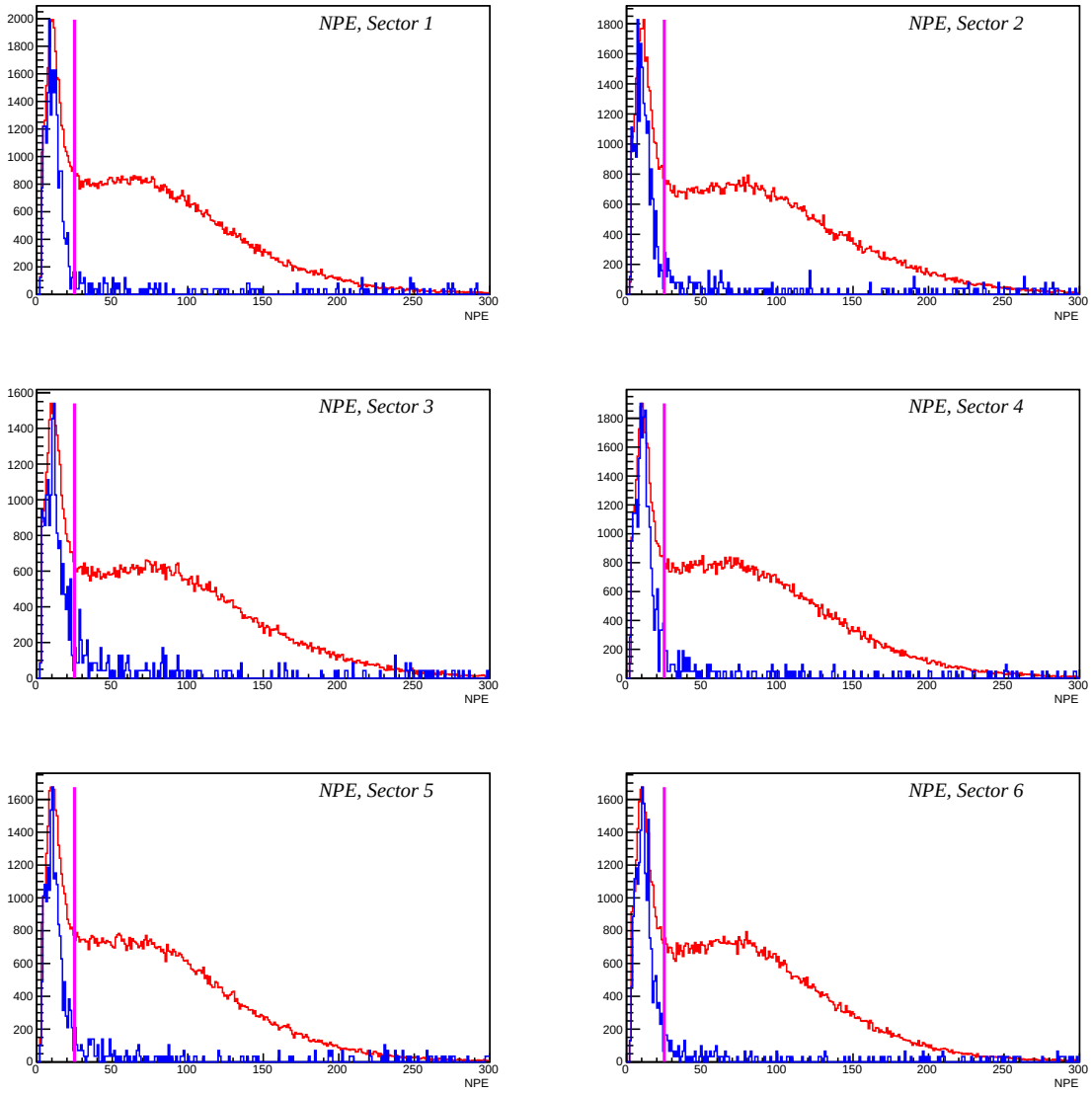

Figure 3.10: *Number of photoelectrons (times 10) produced in the CC from electrons (red histogram) and negative pions (blue histograms) from the* $ep \rightarrow ep\pi^-(\pi^+)$ *events dependent upon the CLAS sectors. No EC cuts were applied.*

3.3.2 Electron Identification

Electromagnetic Calorimeter Energy Cuts

For the calorimeter the total (EC_{tot}) and inner (EC_{in}) deposited energies, inner to outer ratio (EC_{in}/EC_{out}) and total (EC_{tot}/P) and inner (EC_{in}/P) sampling fractions were considered. The EC deposited energies employ the assumption that charged particles deposit their energy differently into the calorimeter by different mechanisms. In the case of the electron this is understood by the electron depositing their energy by creating e^+e^- pairs, thus, creating electromagnetic showers.

Total Energy

The total deposited energy by electrons (red) and negative pions (blue) from the exclusive channel (Equation 3.11) events for the 6 CLAS sectors are represented in Figure 3.11. The vertical magenta line illustrates the cut $EC_{tot} > 0.2\ GeV$ for good electron candidates.

•*EC Total Energy Cut* : $EC_{tot} > 0.2\ GeV$.

3.3.2 Electron Identification

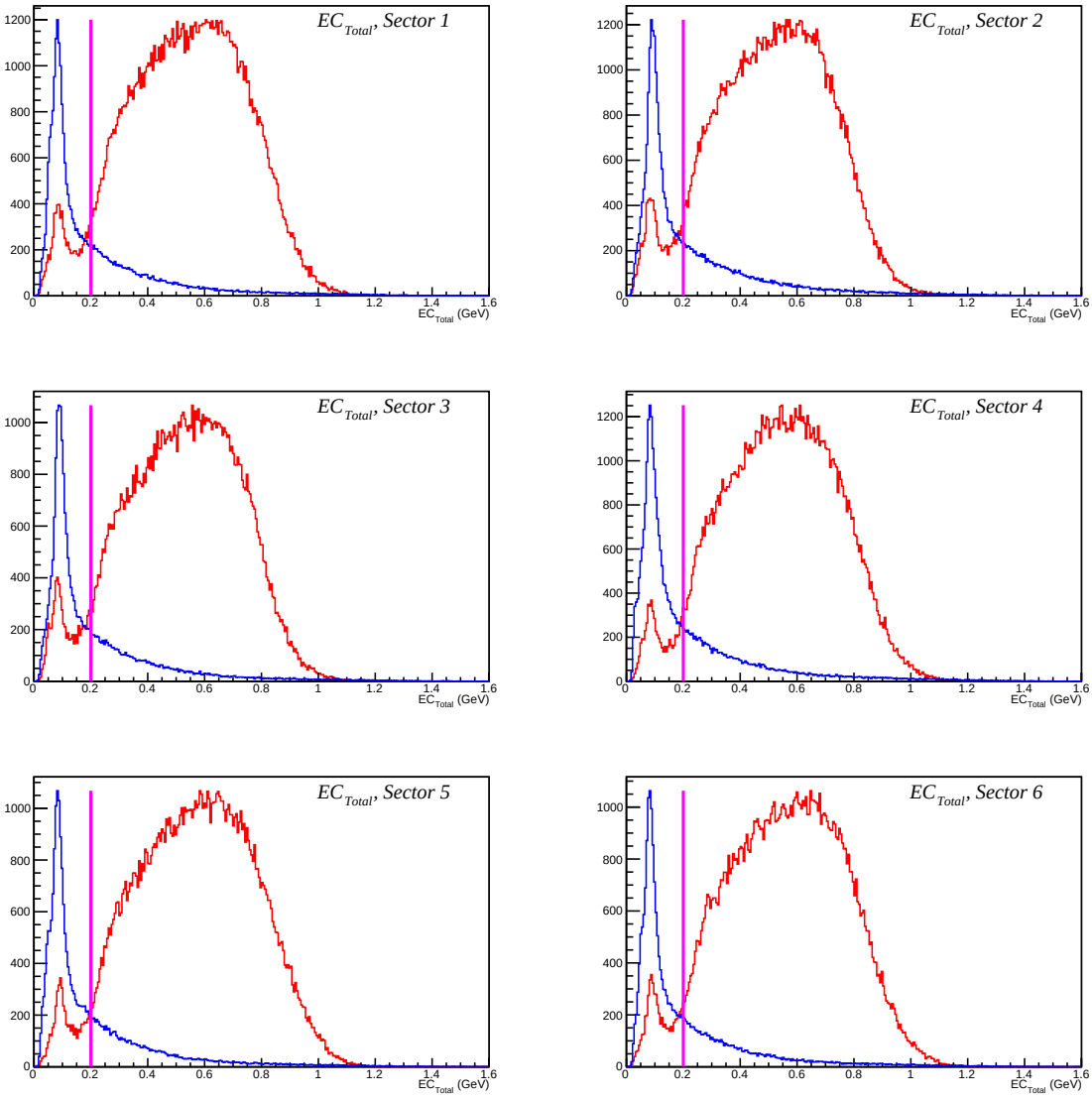

Figure 3.11: *Total EC energy for electrons (red) and negative pions (blue) for the 6 CLAS sectors. The vertical magenta line illustrates the candidates for good electrons. No CC cuts have been applied*

3.3.2 Electron Identification

Inner Energy

The inner deposited energy of the electromagnetic calorimeter by electrons (red) and negative pions (blue) from the exclusive channel (Equation 3.11) events are compared for 3 CLAS sectors, Figure 3.12. The vertical magenta lines illustrate the cut $EC_{in} > 0.1\ GeV$ for good electron candidates.

•*EC Inner Energy Cut* : $EC_{in} > 0.1\ GeV$.

3.3.2 Electron Identification

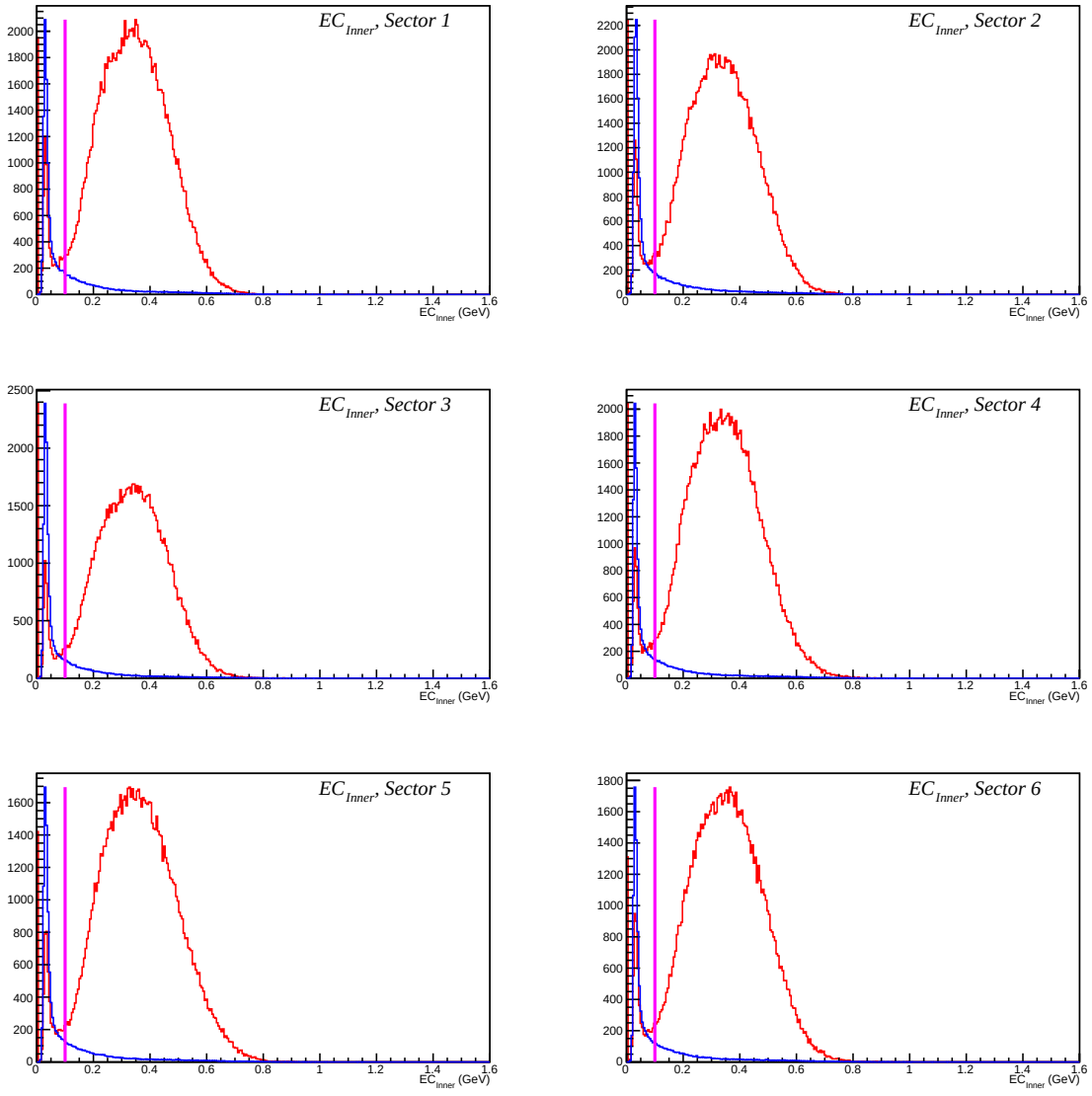

Figure 3.12: *Inner EC energy for electrons (red) and negative pions (blue) for the 6 CLAS sectors. The vertical magenta line illustrates the candidates for good electrons. No CC cuts have been applied.*

3.3.2 Electron Identification

Inner to Outer Energy Ratio

In Figure 3.13, the ratio between the inner and outer energies deposited in the EC is shown as a function of momentum by electrons (left) and negative pions (right) for 3 CLAS sectors. Events above the magenta line indicates a electron candidate, whereas a pion is represented below.

•*EC Inner to Outer Energy Ratio* :

$$\begin{aligned} \frac{EC_{in}}{EC_{out}} &> 1, & P < 1GeV/c \\ \frac{EC_{in}}{EC_{out}} &> 1.5 - \frac{P}{2}, & P > 1GeV/c \end{aligned} \tag{3.12}$$

3.3.2 Electron Identification

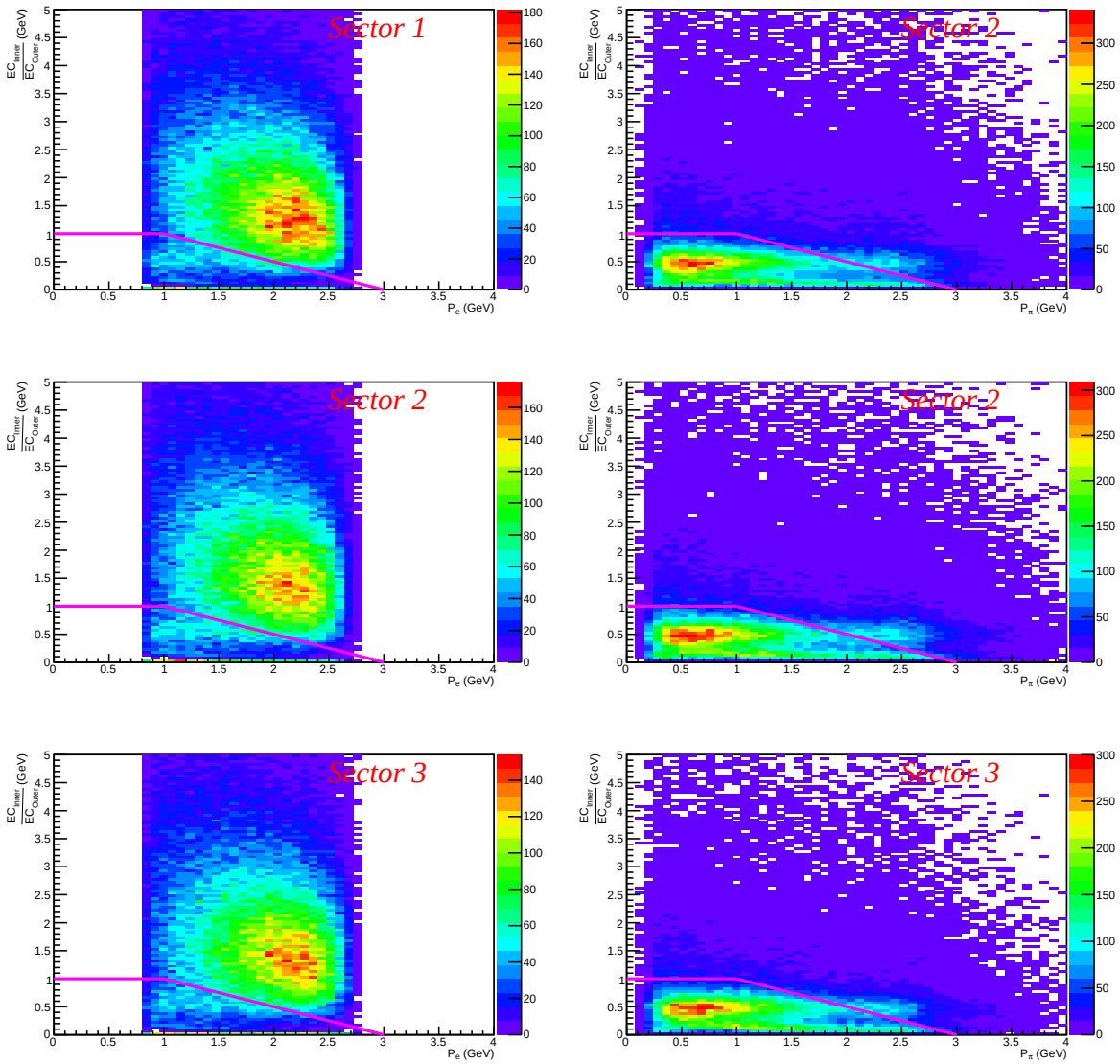

Figure 3.13: *The ratio between the energies deposited in the inner and outer EC versus the momentum by the electrons (left) and pions (right) for the CLAS sectors 1 to 3. The magenta line indicates the cut to separate pions from electrons.*

3.3.2 Electron Identification

Total Sampling Fraction

The EC total sampling fraction $SF_{tot} = EC_{tot}/P$ is a function of momentum (P) for electrons and negative pions, see Figure 3.14. Cuts were incorporated like Figure 3.13 for electron and pion identification. Similar cuts for e1f experimental data are found at [81] [82].

•*EC total Sampling Fraction Cut* :

$$\begin{aligned} SF_{tot} &> 0.3 - 0.0625, \quad P < 2GeV/c \\ SF_{tot} &> 0.75, \qquad\qquad P > 2GeV/c \end{aligned} \tag{3.13}$$

3.3.2 Electron Identification

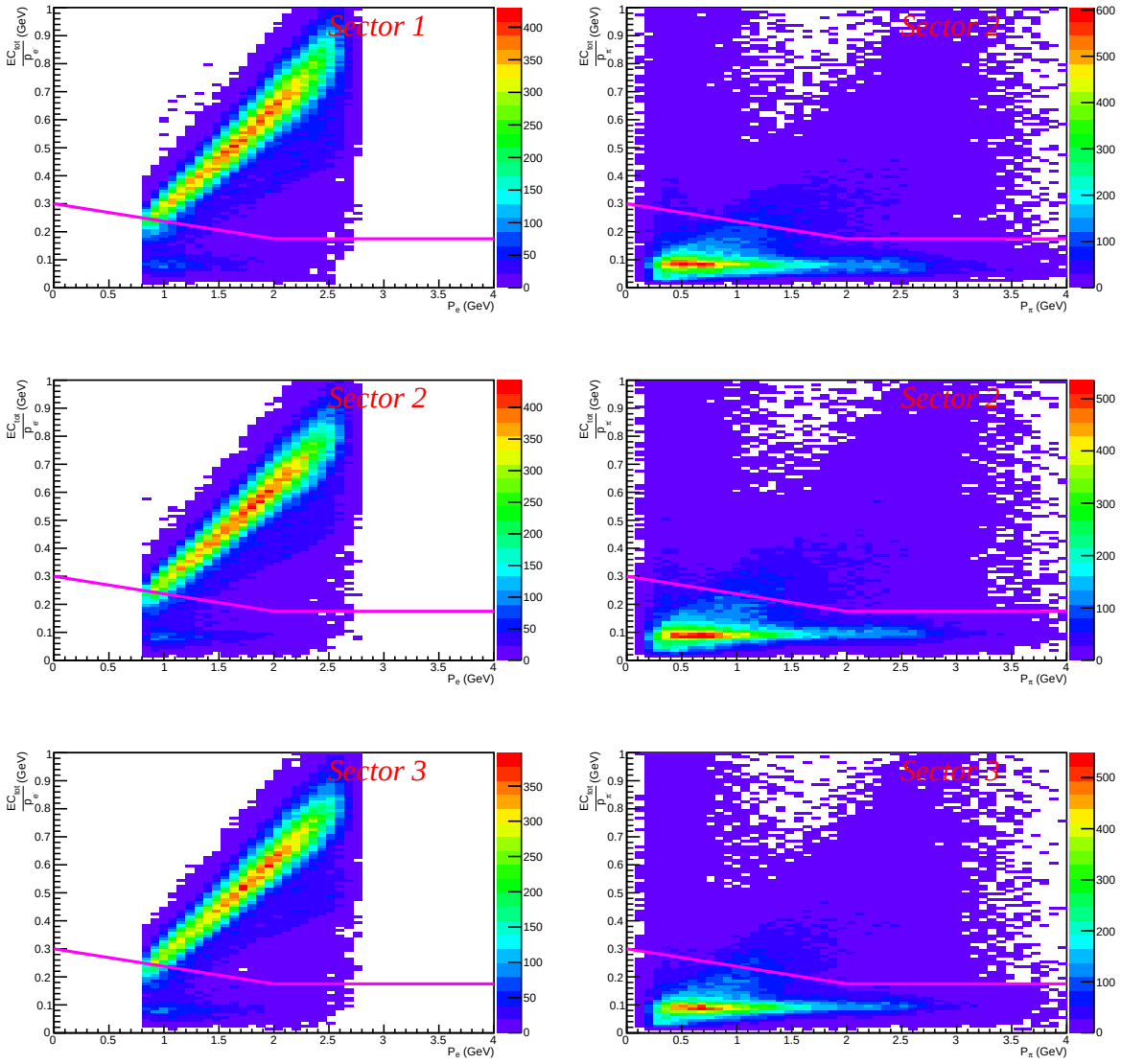

Figure 3.14: *The EC total sampling fraction versus the momentum for electrons (left) and pions (right) for the CLAS sectors 1 to 3. The magenta line indicates the cut to separate pions from electrons.*

3.3.2 Electron Identification

Inner Sampling Fraction

The EC inner sampling fraction $SF_{in} = EC_{in}/P$ is a function of momentum (P) of electrons and negative pions, Figure 3.15. Cuts were incorporated like in Figure 3.14 for electron and pion identification. Similar cuts for e1f experimental data are found at [81] [82].

•*EC inner Sampling Fraction Cut* :

$$SF_{in} > 0.2 - 0.5P \tag{3.14}$$

3.3.2 Electron Identification

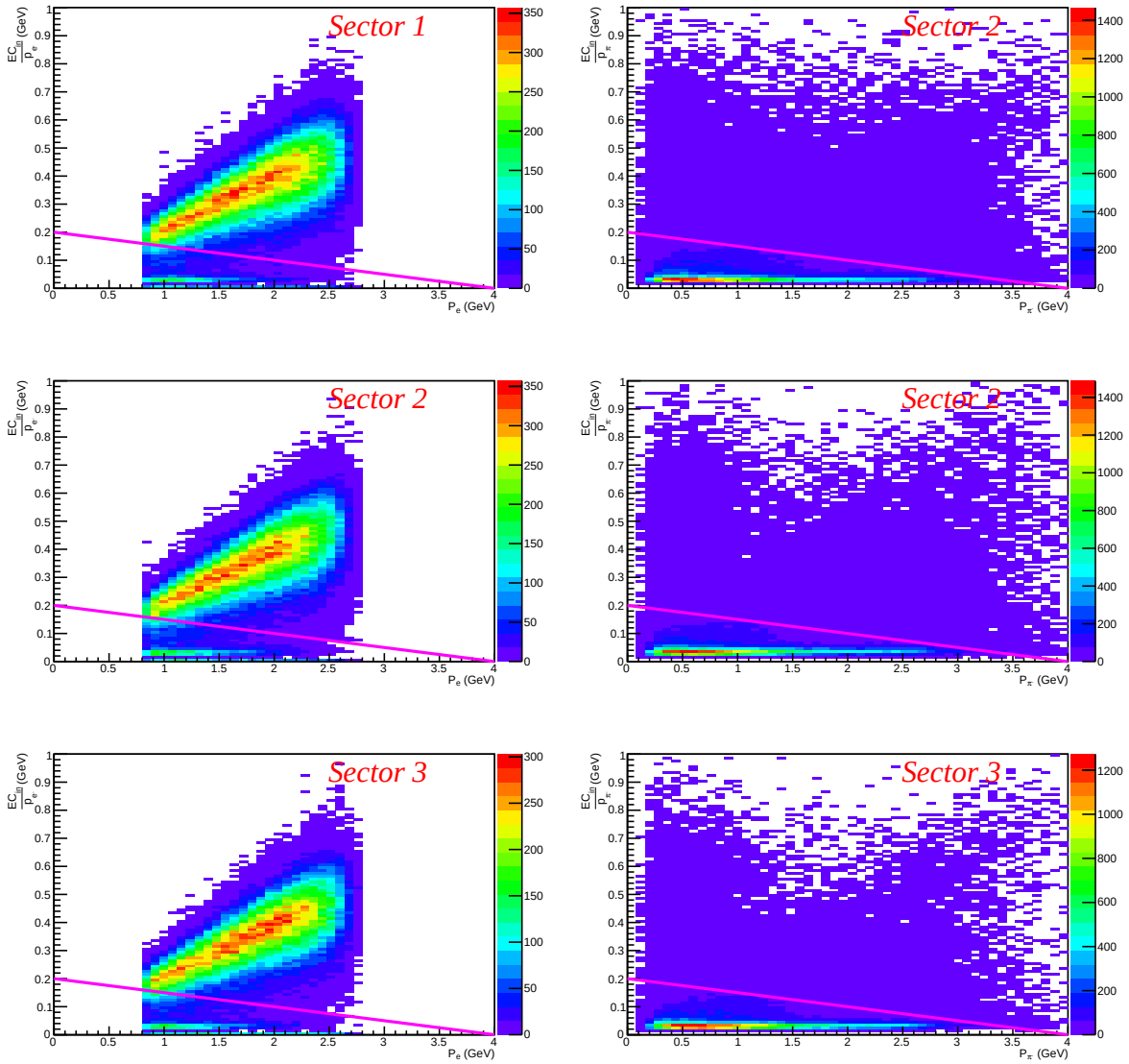

Figure 3.15: *The EC inner sampling fraction versus the momentum for electrons(left) and pions(right) for CLAS sectors 1 to 3. The magenta line indicates the cut to separate pions from electrons.*

3.3.3 Hadron Identification

To minimise the loss of statistics very loose hadron cuts have been applied. Hadrons are required to have a valid trajectory in the drift chamber detector corresponding to a correctly charged particle and a hit time in the time-of-flight that coincides with that of the DC. The consideration in identifying proton or π^- candidates will now be discussed.

Proton Identification

Positive tracks in CLAS are based on their direction of curvature in the toroidal magnetic field with positive tracks bending away from the beam line. When CLAS is operating at 6 GeV positive tracks correspond to protons, kaons and pions. To minimise the loss of statistics protons (p) are defined as positive charged tracks with a Time Of Flight (TOF) mass between 0.8 and $1.2GeV$. Figure 3.16 below illustrates the cut employed to identify proton candidates by analysing the positive x-Missing Mass plot of $ep \rightarrow eX$.

3.3.3 Hadron Identification

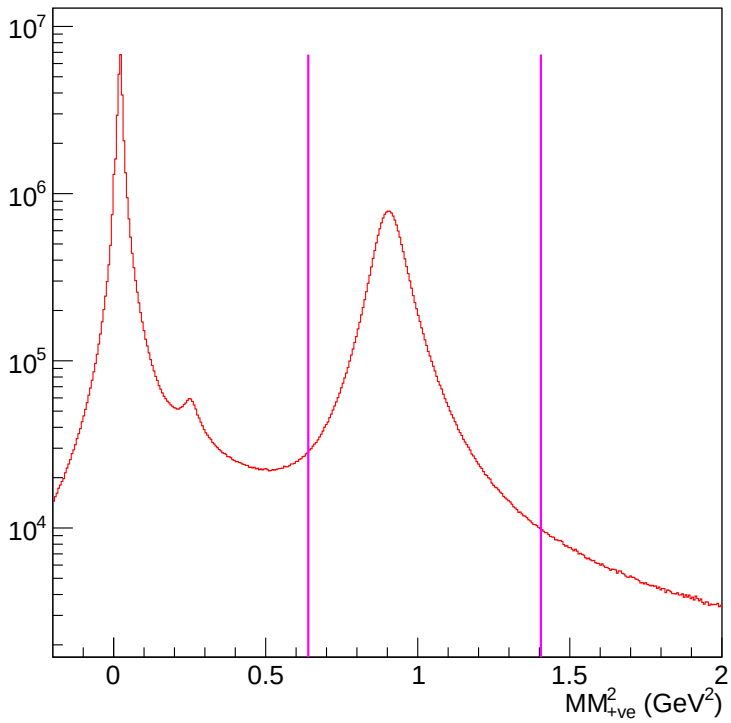

Figure 3.16: *Missing Mass (squared) distribution. Magenta lines indicate proton candidate cuts.*

π^- Identification

To minimise the loss of statistics, like in the proton identification, negative pions (π^-) are defined as negative charged tracks not passing electron cuts, as described in Section 3.3.2, with TOF mass squared below $0.09GeV^2$. Figure 3.17 illustrates the cut employed to identify π^- candidates by analysing the negative x-Missing Mass plot of $ep \rightarrow eX$.

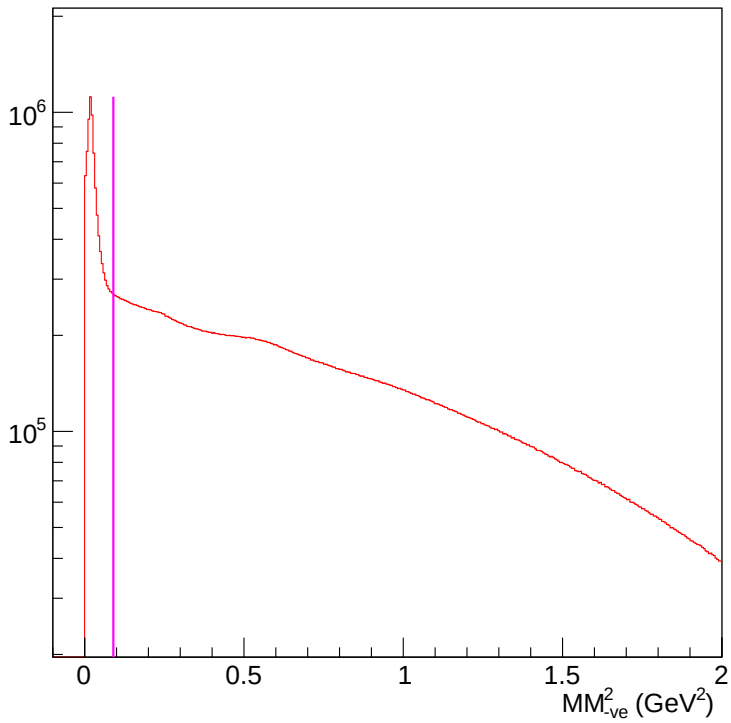

Figure 3.17: *Logarithmic Missing Mass (squared) distribution. Magenta lines indicates the* $0.09GeV^2$ *cut for* π^- *candidates.*

3.3.4 Energy and Momentum corrections

Energy loss can be understood by charged particles losing energy as they traverse target material or detector equipment such as the drift chambers. This is not accounted for in the standard event reconstruction and should therefore be taken into consideration. Energy loss corrections have been applied to the two hadrons using a modified version [85] of the *Eloss* package usually used for photon experiments. Here the program takes a four-vector, along with the particles vertex, mass and experimental conditions and develops a new four-vector with corrected energy. Since the proton arises from the decay of the Λ into a proton and π^- there are two vertex locations. One being the vertex of the proton and electron scattering point v_1 and the other the decay of the Λ into its constituent components, namely the proton and π^- (v_2).

3.3.4 Energy and Momentum corrections

- $\mathbf{v}_1$, The vertex where the electron scatters from the proton. Found from looking at the interaction point of the nominal electron beam vector and the measured scattered electron vector.

- $\mathbf{v}_2$, The vertex where the Λ decays into the proton and π^-. Found at the interaction point of the measured proton and π^- vector.

This enables the vertex positions of the detected particles to be correctly incorporated into the *Eloss* package. In this version the changes represent the differences of this e1f experiment such as the start counter being removed and some of the geometry parameters illustrating the differences of the e1f target from the g11 target.

Momentum correction functions [86] have been developed in order to take into account the inaccurate knowledge of the torus magnet field map and that of the Drift Chamber positions. Correction has only been applied to the electron, and not the hadrons, as it has been found that it does not improve the resolution of the Λ invariant mass. The Λ peak is so narrow ($\sigma \approx 1MeV$) and close to the sum of the proton and pion masses, that the momenta of the decay proton and pion are strongly correlated. Thus, their momenta always lay in a kinematic region not well covered by the available corrections [86].

The effect of these momentum corrections can be illustrated by comparing the X missing Mass distributions for semi-inclusive Λ events i.e. $ep \rightarrow ep\pi^- X$. By fitting the K^+ and K^* regions with a Gaussian (peak) and 4th order polynomial (background) before and after electron momentum corrections it is evident that the resolution of the peaks is enhanced as the sigma of the fits decreases. Figures 3.18, 3.19 and Table 3.5 lists the fitted parameters. The quoted values for the K^+ is 0.494 ± 0.016 (GeV) and for K^* it is 0.892 ± 0.26 (GeV).

3.3.4 Energy and Momentum corrections

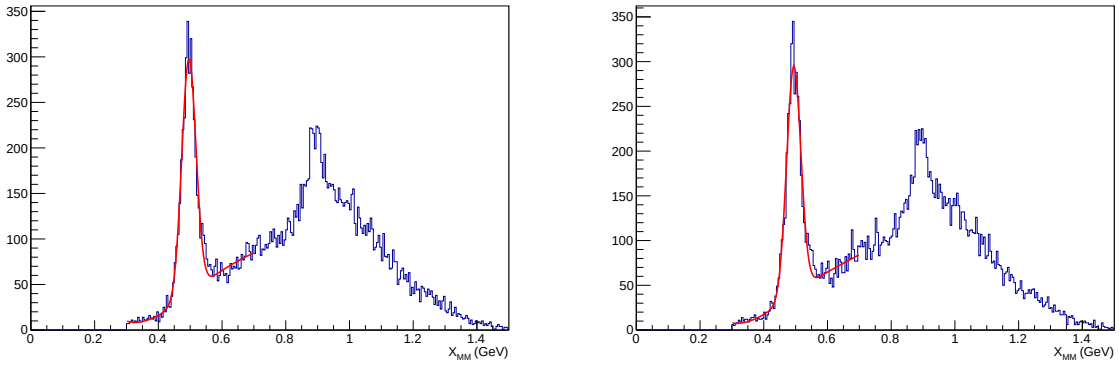

Figure 3.18: *X missing mass(X_{MM}) distribution with Gaussian plus 4th order polynomial fit to the K^+ region for before (left) and after (right) electron momentum corrections.*

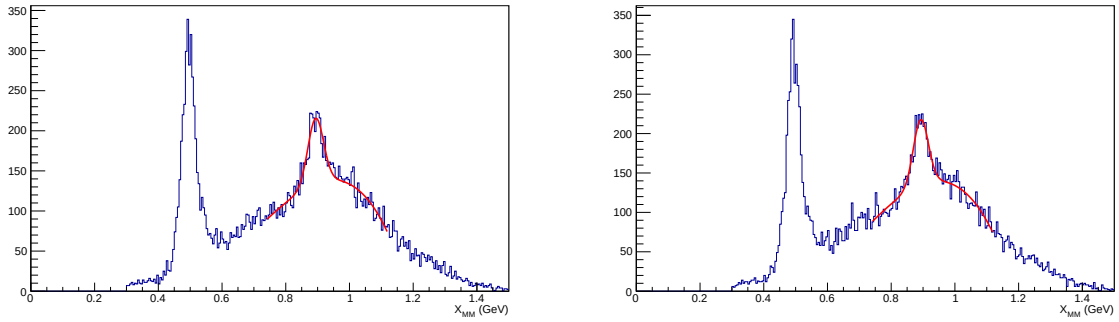

Figure 3.19: *X missing mass(X_{MM}) distribution with Gaussian plus 4th order polynomial fit to the K^* region for before (left) and after (right) electron momentum corrections.*

Parameter	**K+ before**	**K+ after**	**K* before**	**K* after**
Mean (μ)	0.496	0.495	0.894	0.893
Sigma (σ)	0.025491	0.015723	0.02485	0.01357

Table 3.5: *X missing mass (X_{MM}) Gaussian fit parameters (GeV) to the K^+ and K^* peaks for before and after electron momentum corrections.*

3.3.5 DIS region cuts

The Deep Inelastic scattering region is defined by high Q^2 and W^2 (Section 1.3). The cuts used in this analysis to select the DIS events are $Q^2 > 1GeV^2$, $W^2 > 5GeV^2$ and $y < 0.86GeV$. Distributions of Q^2, W^2 and y before and after DIS cuts are shown in Figure 3.20, 3.21 and 3.22 respectively. The Feynman-x variable x_F against Q^2, W^2 and y before and after DIS cuts is also illustrated in Figures 3.23, 3.24 and 3.25.

3.3.5 DIS region cuts

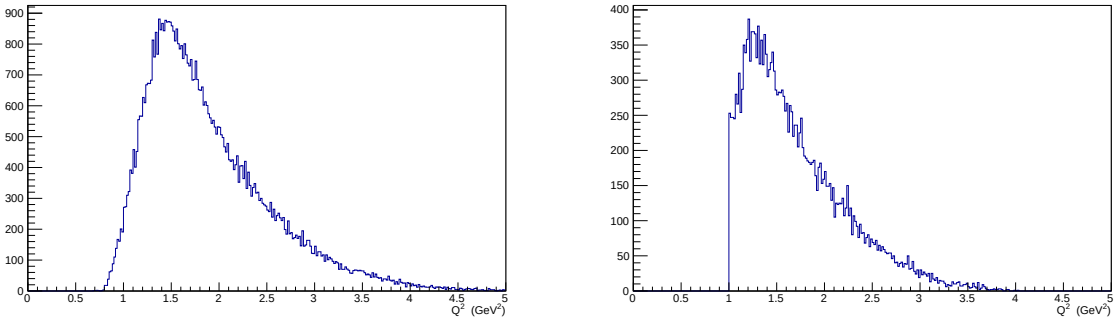

Figure 3.20: Q^2 *kinematic distributions for* $e\Lambda X$ *events before (left) and after (right) DIS cuts.*

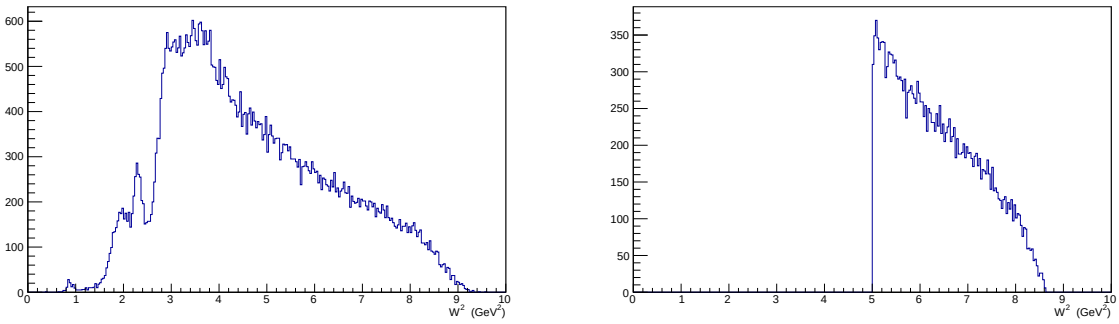

Figure 3.21: W^2 *kinematic distributions for* $e\Lambda X$ *events before (left) and after (right) DIS cuts.*

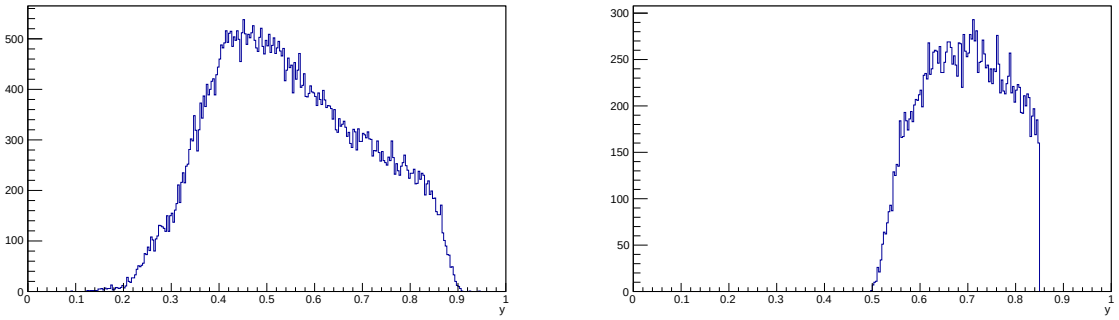

Figure 3.22: Y *kinematic distributions for* $e\Lambda X$ *events before (left) and after (right) DIS cuts.*

3.3.5 DIS region cuts

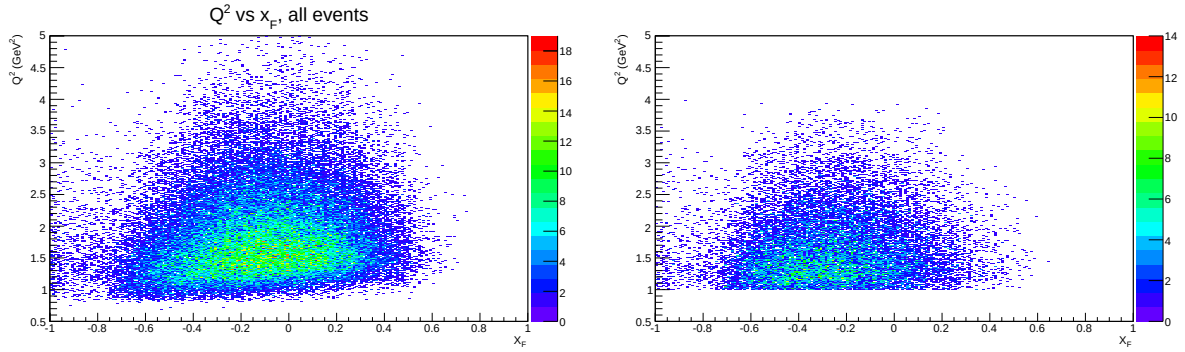

Figure 3.23: *Q^2 against x_F kinematic distributions for $e\Lambda X$ events before (left) and after (right) DIS cuts.*

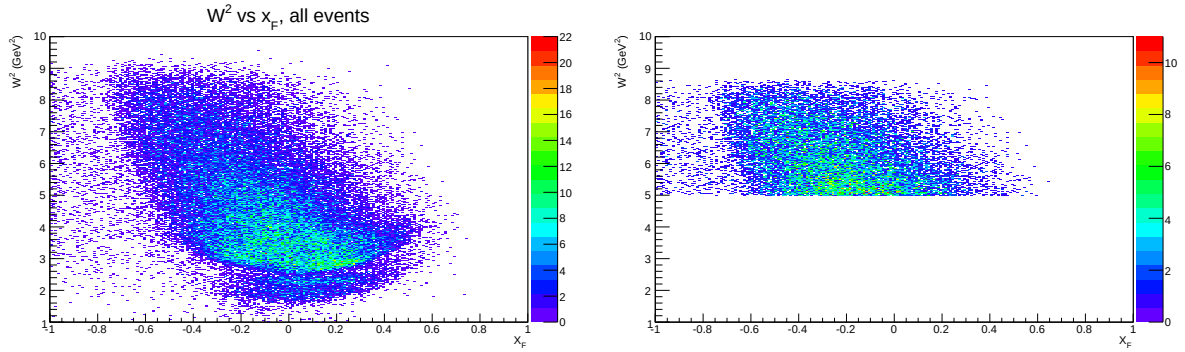

Figure 3.24: *W^2 against x_F kinematic distributions for $e\Lambda X$ events before (left) and after (right) DIS cuts.*

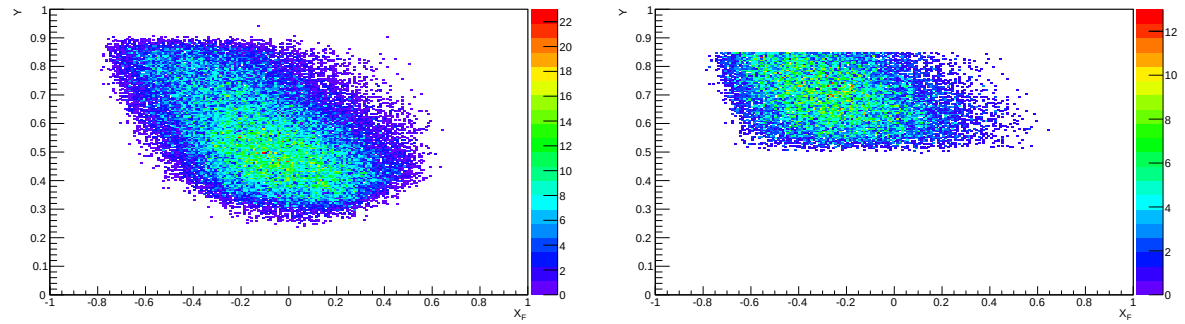

Figure 3.25: *y against x_F kinematic distributions for $e\Lambda X$ events before (left) and after (right) DIS cuts.*

3.3.6 SIDIS region cuts

The distribution of the missing mass (MM) of $e\Lambda X$ events after DIS cuts is illustrated in Figure 3.26. A prominent peak of exclusive $e\Lambda(K^+)$ can be seen with the missing mass peak $M = 494.2 \pm 0.5 MeV$ with a width $\sigma = 22.8 \pm 0.6 MeV$. After this exclusive peak, there is a broad distribution of events, with a smaller peak at $MM \approx 0.9 GeV$ corresponding to $e\Lambda(K^*)$ events. The missing $K^*(890)^+$ peak is $M = 893.2 \pm 1.6 MeV$ with a width $\sigma = 24.7 \pm 2.2 MeV$.

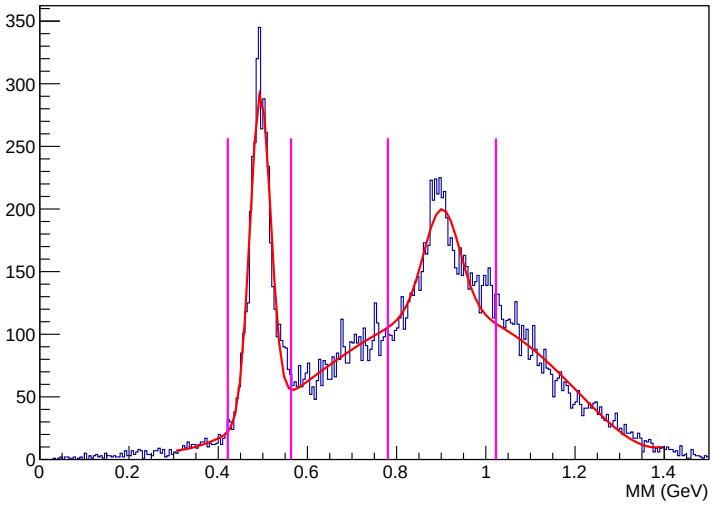

Figure 3.26: *Missing mass of* $ep \rightarrow e\Lambda X$ *after DIS cuts. Magenta lines illustrate* 3σ *regions about both the* K *and* $K*$

The issue whether the large fraction of $e\Lambda(K^+)$ events should be incorporated into the analysis is now evident. From a theoretical angle, requiring the inclusive final states requires that one has to sum over all the possible exclusive channels. For this argument the $e\Lambda(K^+)$ events have to be included in the analysis. However, it is also known that at CLAS energies and after DIS cuts a large proportion of the observed $e\Lambda(K^+)$ could be produced in a completely different mechanism, i.e. high mass resonance decay. It is for this reason that $e\Lambda(K^+)$ events will be excluded from the analysis. However, a missing mass dependence of the Λ polarisation will also be incorporated into the analysis.

3.3.7 Λ identification and background analysis

Monte Carlo simulations [85], chapter 4, have shown that the missing mass region between the missing K^+ peak and the threshold for an additional pion production is dominated by the exclusive $e\Sigma^0(K^+)$ events with subsequent $\Sigma^0 \rightarrow \Lambda\gamma$ decay. This can be seen in Figure 3.27 with the missing mass of all Monte Carlo Λ events with $e\Lambda K^+$ events removed (blue) compared with that of Σ^0 events (red). A region to select inclusive Λ DIS is established through the cut $MM > 0.65$, as shown by the vertical magenta line, hence minimising the Σ^0 contribution.

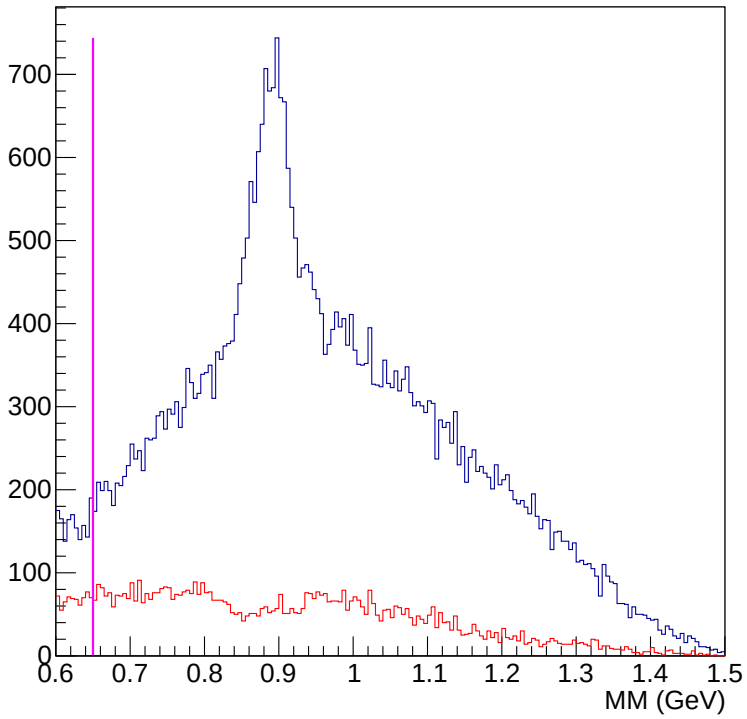

Figure 3.27: *Missing mass of $ep \rightarrow e\Lambda X$ events after DIS cuts from the simulation (blue) compared with the contribution from the Σ^0 events only (red). The magenta line is the cut to select inclusive Λ events.*

3.3.7 Λ identification and background analysis

The selection of the $ep\pi^-X$ events enables the Λ to be available in the invariant mass distribution of the proton and pion. The result is illustrated in Figure 3.28. A clear peak is visible on top of a background. A small shoulder probably due to badly reconstructed particles can

be seen on the right side of the peak. A fit of this distribution with a Gaussian plus a second order polynomial background (red line) produces $M = 1115.89 \pm 0.01 MeV$ with a width $\sigma = 0.99 \pm 0.01 MeV$.

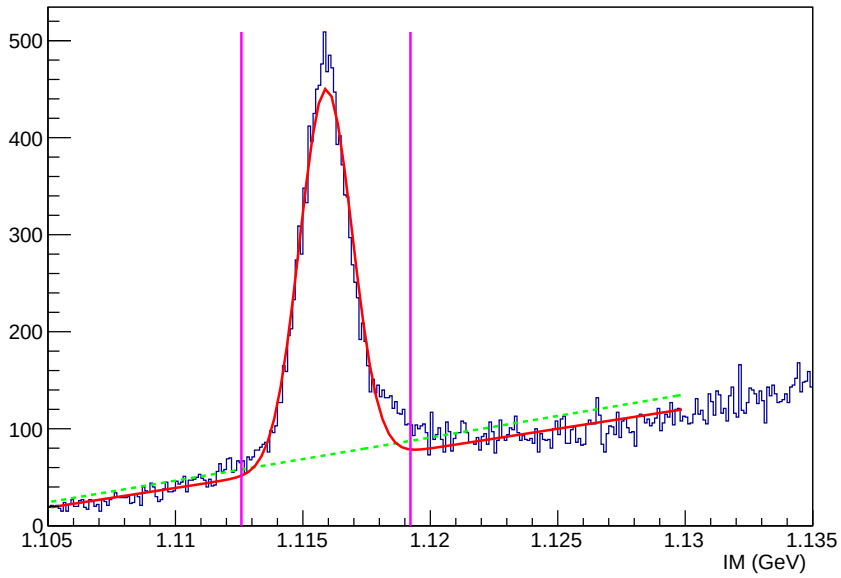

Figure 3.28: *Invariant mass of the proton and π^- for $ep\pi^-X$ events. Red line is the Gaussian plus polynomial combined. The magenta lines illustrate the 3σ Λ invariant mass cuts and the green dashed line the polynomial.*

The background region is determined by taking the integral of the polynomial (within $M \pm 3\sigma$ cuts). The signal region is defined by taking all events within the $M \pm 3\sigma$ cuts and subtracting the background from it. Therefore, the signal to background ratio is:

$$\frac{Signal}{Background} \approx 2.1 \tag{3.15}$$

The fraction of the background events was found not to vary as a function of kinematic variables and no strong dependence was found on the important polarisation extraction proton decay angle ($\cos(\theta_p^*)$), section 5.3. In Figure 3.29 the background fraction is plotted as a function of $\cos(\theta_p^*)$ for $x_F = -0.2 \rightarrow -0.1$. The black circles represent the total background, whilst red

and blue points illustrate the results for positive and negative beam helicity events respectively. The background proportion equates to 30% consistent with the signal to background ratio in Equation 3.15.

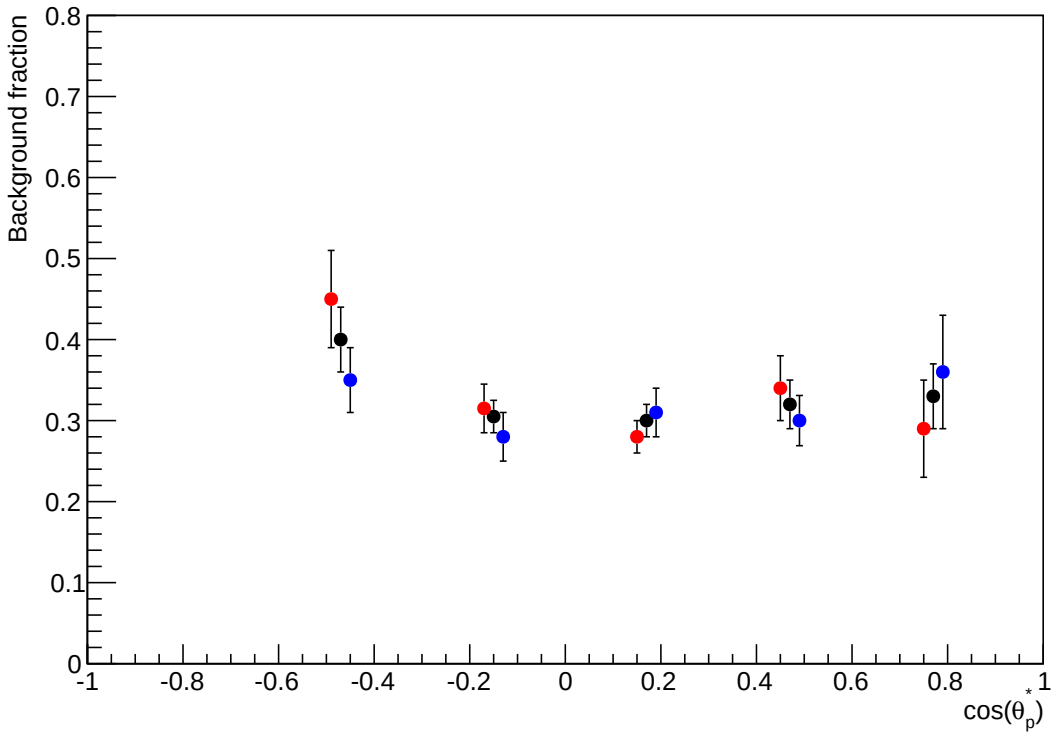

Figure 3.29: *Fraction of background events against* $\cos(\theta_p^*)$ *for* $-0.2 < x_F < -0.1$. *Black points are total, red are positive and blue are negative beam helicity events (x-position of points have been moved for clarity).*

3.4 Kinematic analysis

A series of kinematic distributions are displayed in Figures 3.30 and 3.31 after Λ invariant mass, DIS, MM, fiducial and particle identification cuts. These directly relate to the distribution, fragmentation and fracture functions (Appendix A and B) and are the observed kinematics that we measure from the e1f data. The Feynman-x (x_F) plot illustrates that most events are located in the Target Fragmentation Region (TFR), as $x_F < 0$. This is demonstrated with a mean value of $< x_F >= -1.802$. The Λ azimuthal angle (ϕ_Λ)) distribution in Figure 3.30 (d) highlights a peak at $\phi \approx \pm 180^\circ$ and a dip with almost no detection at $\phi_\Lambda \approx 0^\circ$. This behaviour is entirely due to the CLAS forward hole, producing zero acceptance at low Λ angles, Appendix C.

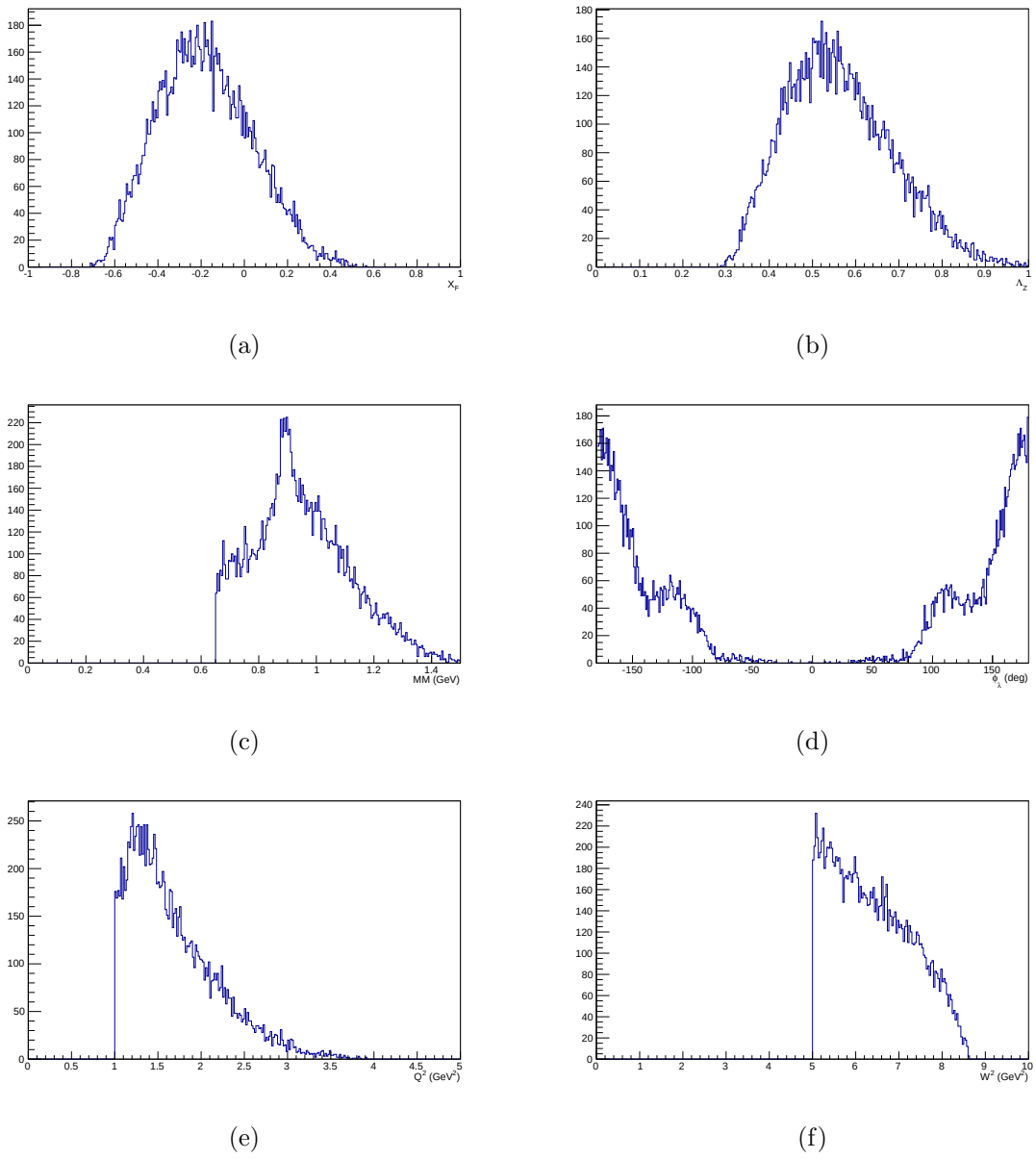

Figure 3.30: *Experimental data observed kinematics after all particle identification and detector acceptance cuts for a) Feynman-x (x_F), b) Λ_Z, c) MM ($p\pi^-$), d) ϕ_Λ, e) Q^2 and f) W^2.*

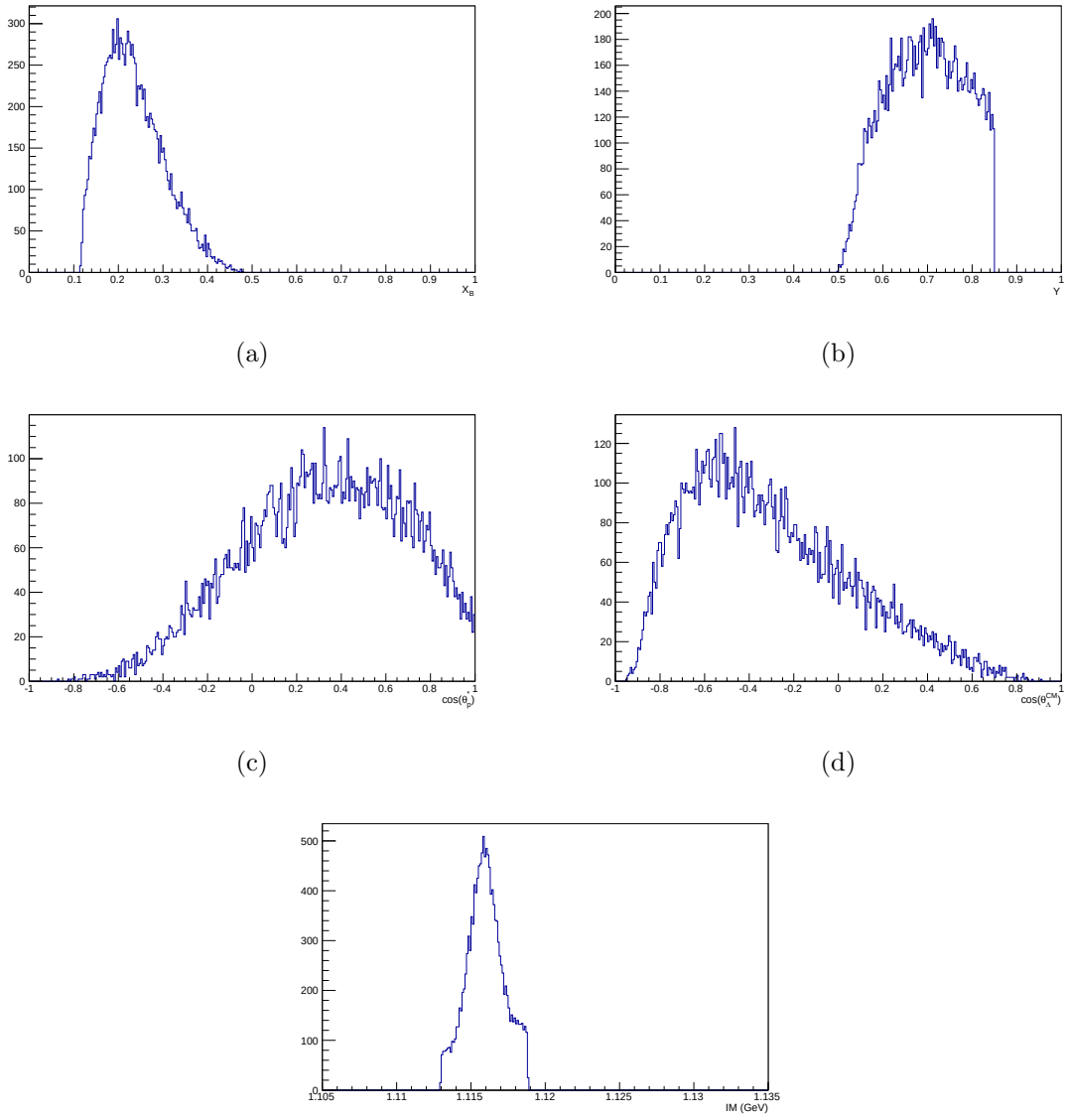

Figure 3.31: *Experimental data observed kinematics after all particle identification and detector acceptance cuts for a) Bjoerken-X (x_B), b) Y, c) $\cos(\theta_p^*)$, d) $\cos(\theta_\Lambda^{CM})$ and e) Λ invariant mass ($p\pi^-$).*

3.4.1 Kinematical Binning

For each observed kinematic, events are grouped into bins of specific ranges. The binning values used for this analysis, and more importantly the Beam Spin Asymmetry method of Λ polarisation extraction, are given in Tables 3.6 and 3.7. The bin widths are chosen to have approximately the same amount of events in each kinematical bin.

Kinematic Binning for Beam Spin Asymmetry (BSA)					
Kin	**Bin 1**	**Bin 2**	**Bin 3**	**Bin 4**	**Bin 5**
x_F	-0.7 $\rightarrow -0.5$	-0.5$\rightarrow -0.4$	-0.4 $\rightarrow -0.3$	-0.3 $\rightarrow -0.2$	-0.2 $\rightarrow -0.1$
Q^2	1.0 $\rightarrow$ 1.25	1.25$\rightarrow$ 1.51	1.51 $\rightarrow$ 1.91	1.91 $\rightarrow$ 3.9	-
W^2	5.0 $\rightarrow$ 5.6	5.6$\rightarrow$ 6.31	6.31 $\rightarrow$ 7.15	7.15 $\rightarrow$ 8.71	-
x_B	0.11 $\rightarrow$ 0.18	0.18$\rightarrow$ 0.22	0.22 $\rightarrow$ 0.27	0.27 $\rightarrow$ 0.48	-
Y	0.5 $\rightarrow$ 0.63	0.63$\rightarrow$ 0.7	0.7 $\rightarrow$ 0.78	0.78 $\rightarrow$ 0.91	-
Z_Λ	0.26 $\rightarrow$ 0.43	0.43$\rightarrow$ 0.5	0.5 $\rightarrow$ 0.55	0.55 $\rightarrow$ 0.61	0.61 $\rightarrow$ 0.69
MM	0.45 $\rightarrow$ 0.56	0.56$\rightarrow$ 0.72	0.72 $\rightarrow$ 0.84	0.84 $\rightarrow$ 0.91	0.91 $\rightarrow$ 0.99
$\cos(\theta_\Lambda^{CM})$	-1.0 $\rightarrow$ -0.7	-0.7$\rightarrow$ -0.5	-0.5 $\rightarrow$ -0.3	-0.3 $\rightarrow$ 0.0	0.0 $\rightarrow$ 0.4
ϕ_Λ	-180 $\rightarrow$ -170	-170$\rightarrow$ -160	-160 $\rightarrow$ -145	-145 $\rightarrow$ -119	-119 $\rightarrow$ -64

Table 3.6: *Binning parameters for different kinematics.*

Kinematic Binning for Beam Spin Asymmetry (BSA)					
Kin	**Bin 6**	**Bin 7**	**Bin 8**	**Bin 9**	**Bin 10**
x_F	-0.1 $\rightarrow$ 0.0	0.0$\rightarrow$ 0.1	0.1 $\rightarrow$ 0.2	0.2 $\rightarrow$ 0.5	-
Z_Λ	0.69 $\rightarrow$ 1.04	-	-	-	-
MM	0.99 $\rightarrow$ 1.1	1.1$\rightarrow$ 1.6	-	-	-
$\cos(\theta_\Lambda^{CM})$	0.4 $\rightarrow$ 1.0	-	-	-	-
ϕ_Λ	-64 $\rightarrow$ -115.3	115.3 $\rightarrow$ 144.17	144.17 $\rightarrow$ 160.5	160.5 $\rightarrow$ 170.9	170.9 $\rightarrow$ 180

Table 3.7: *Binning parameters for different kinematics.*

3.5 Number of Events

In Table 3.8 the number of events after each step on the analysis is reported. After background subtraction (After BKG sub) represents the number of events in the signal region of the Λ invariant mass. The state $(-+-X)$ illustrates the initial two negative, one positive particle skim of the data that was mentioned in chapter 2.

Final state	**Cut**	**Total Events**	**After BKG sub**
$-+-X$	None	232514210	-
$-+-X$	Fiducial	137579991	-
$ep\pi^-X$	PID	6599222	-
$e\Lambda X$	Λ ID	52900	37122
$e\Lambda X$	DIS	19408	13515
$e\Lambda X$	MM	13901	9418

Table 3.8: *Number of events after each step of the analysis.*

3.6 Summary

In this chapter methods to isolate SIDIS candidate events from data recorded in the e1f experiment were detailed. This event selection procedure incorporated the use of fiducial, target vertex and particle identification cuts to enable final particle candidates to be isolated in the channel $ep \rightarrow e\Lambda X$. The next chapter details a Monte Carlo simulation and explains how this is implemented in the analysis and why it is required.

Chapter 4

Monte Carlo simulation

The main purpose of the Monte Carlo simulation is to test the polarisation extraction method in the Beam Spin Asymmetry (BSA) analysis (section 5.1) with systematic studies and to normalise the Maximum Likelihood Extraction (MLE) method, section 5.2. For this analysis the Monte Carlo simulated the $ep \rightarrow e'p\pi^- X$ reaction using the standard CLAS simulation and reconstruction software packages. The procedure, as detailed in this chapter, was as follows:

- Generate Events with clasDIS.
- Simulate detector geometry and interaction using GEANT(GSIM).
- Simulate detector inefficiencies and resolutions using GSIM Post Processing (GPP).
- Reconstruction of particle tracks.

These generated and reconstructed events are then subject to the same analysis process as in the experimental data. What follows is a more detailed description of the process and a comparison between Monte Carlo and experimental kinematics. More in depth details relating to the BSA or MLE method can be found in chapter 5.

4.1 Event generation

A comparison of the experimental data to the simulation is required to fully understand the components of the analysis. This is performed by the development of a Monte Carlo. This procedure involves the generation of a random assortment of simulated data which is then passed to a simulation of the CLAS detector. Monte Carlo event generation simulations of the process have been performed using the clasDIS generator [87], which is based on the PYTHIA and JETSET [88] simulation codes. Some of the parameters of the JETSET contribution (governing the fragmentation of quarks into the final hadrons) have been tuned by comparison with experimental distributions. The modified parameters are:

- **PARJ(2)** , s quark pair suppression factor compared to u and d quarks.
- **PARJ(12)** , probability that a strange meson has spin 1.
- **PARJ(21)** , Gaussian width of the transverse momentum distribution of the primary hadron.
- **PARJ(21)** , cut-off (GeV) where the fragmentation process is stopped and the final hadrons are produced.

The above parameters have been listed for three sets of final state channels. Two of them correspond to the $e\Lambda K^+$ and $e\Lambda K^*(890)^+$ reaction channels and the final (inclusive) for all the remaining final states. The three sets of parameters are listed in Table 4.1, together with the default values.

PARJ	**default**	K^+	$K^*(890)$	**inclusive**
2	0.3	0.4	0.4	0.4
12	0.6	0.35	0.35	0.35
21	0.36	0.6	0.6	0.6
33	0.8	0.7	0.5	0.05

Table 4.1: *JETSET parameters modified for the simulation of three different final states.*

4.2 The CLAS response simulation

The output of the clasDIS event generator (above) is the direct input of the CLAS simulation and reconstruction packages. The CLAS response has been simulated through GSIM [89]:

- The CLAS simulation GSIM program was ran using the e1f calibration index RunIndexe1f.
- The GPP package [90] was operated to consider the actual performance of the CLAS detector. This was performed by setting the smearing factors (as explained after the bullet points) to 1.2 for the TOF system and to 2.5 for the three sets of drift chambers.
- The output of the CLAS simulation was then reconstructed [91] as for the experimental data.
- The reconstructed Monte Carlo data were then studied using the same skim and analysis programs used for the experimental data.

As stated in the MC a smearing factor is required, this is to better simulate the experimental distribution of data. The smearing parameters have been fixed by analysing the experimental resolution of the Λ peak in the invariant mass ($p\pi^-$) and the $K*$(892 MeV) peak in the missing mass distributions. The Monte Carlo Λ invariant mass distribution is illustrated in Figure 4.1 with the signal and background analysis repeated as in the experimental data case (section 3.3.7). The Λ mass is $M = (1115.69 \pm 0.006) MeV$ with a width $\sigma = (1.057 \pm 0.007) MeV$. The signal to background ratio $S/B = \approx 2.1$.

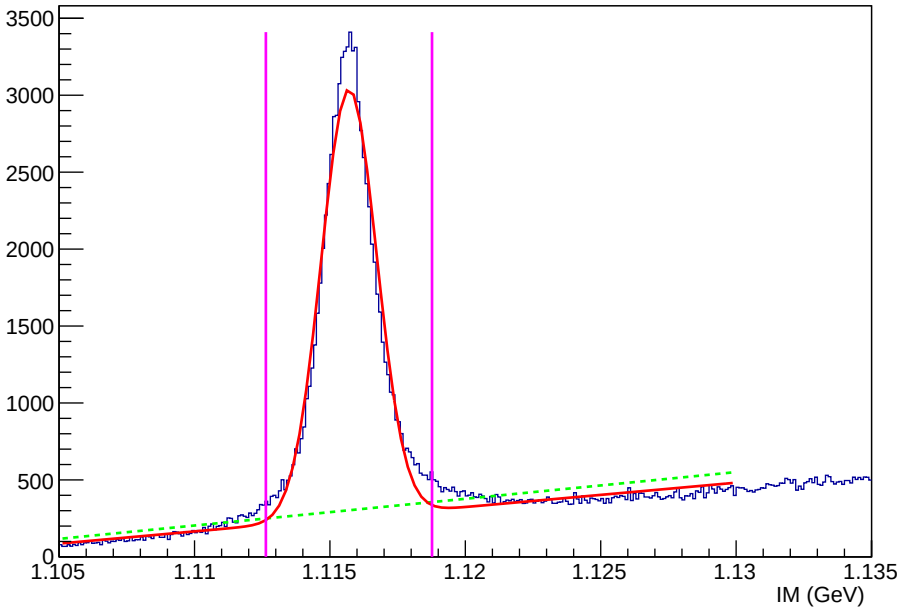

Figure 4.1: Λ *Invariant Mass (IM) distribution of proton and* π^- *for Monte Carlo* $e\Lambda X$ *events (after all event cuts). Red fitted line is a Gaussian and 2nd order polynomial, green dashed line is the background polynomial and the magenta lines indicate the three sigma cuts of the Gaussian.*

4.3 Normalisation of Monte Carlo Data Files

As explained in section 4.1 there are different final sets of Monte Carlo data that represent different final particle states. Thus, normalisation of the different sets have to be determined in order to get the final weight of the different Monte Carlo data sets. For this reason the Missing Mass (MM) distribution of $e\Lambda X$ events have been used. Figure 4.2 represents the K^* and *inclusive* MC contributions along with the final normalised sum of the two sets.

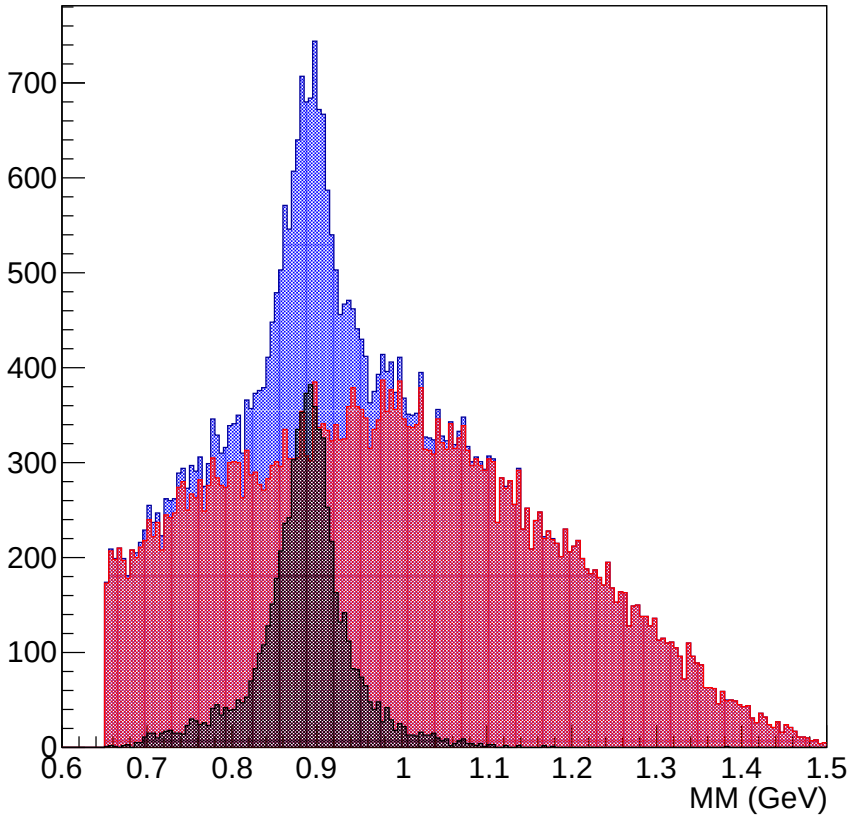

Figure 4.2: *Missing Mass (MM) distribution for Monte Carlo $e\Lambda X$ events (after all event cuts). Black histogram is the K^* MC data set, red is the inclusive and blue is the summed final MC data Missing Mass histogram.*

The normalisation factor of the *inclusive* and K^* data sets was calculated by minimising the difference in the final summed Missing Mass distribution to the experimental data. The procedure that was performed found the relative weight of each missing mass distribution in the K^* and *inclusive* data set by allowing a free parameter to scale the fit to the experimental:

$$MM_{EXP} = \alpha(MM_{K^*}) + \beta(MM_{inclusive}) \tag{4.1}$$

Where MM_{EXP} is the experimental missing mass, MM_{K^*} the K^* MC data set missing mass, $MM_{inclusive}$ the inclusive MC data set missing mass with α and β the free scaling parameters

for each MC data set. These scaling parameters were then used to scale the clasDIS files for each MC data set accordingly. It was found that for the K^* (α) there were 660 clasDIS files and 7x660 = 4640 files for the inclusive (β) data set respectively. This enabled the relative weight between the inclusive and K^* MC data set to equal to one. A comparison of the missing mass distribution for the MC data set, after normalisation and summation, and the experimental data is illustrated in Figure 4.3.

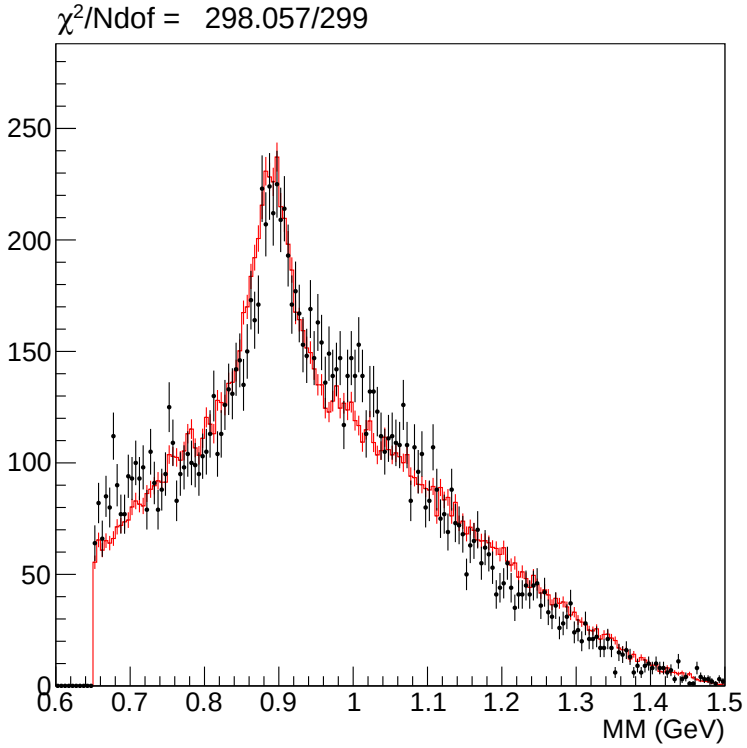

Figure 4.3: *Missing Mass (MM) distribution for Monte Carlo eΛX events (red) and experimental data (black) after all normalisation and summation MC procedures.*

4.4 Comparison of Monte Carlo and experimental data

Comparison between other kinematics for experimental and Monte Carlo data (after normalisation and summation) can be seen in Figures 4.4 and 4.5, with different kinematical distributions illustrating excellent agreement. The discrepancy in the Λ invariant mass distribution (Figure

4.5d) between experimental and Monte Carlo data is due to the different levels of background, as no invariant mass cuts are implemented for this distribution.

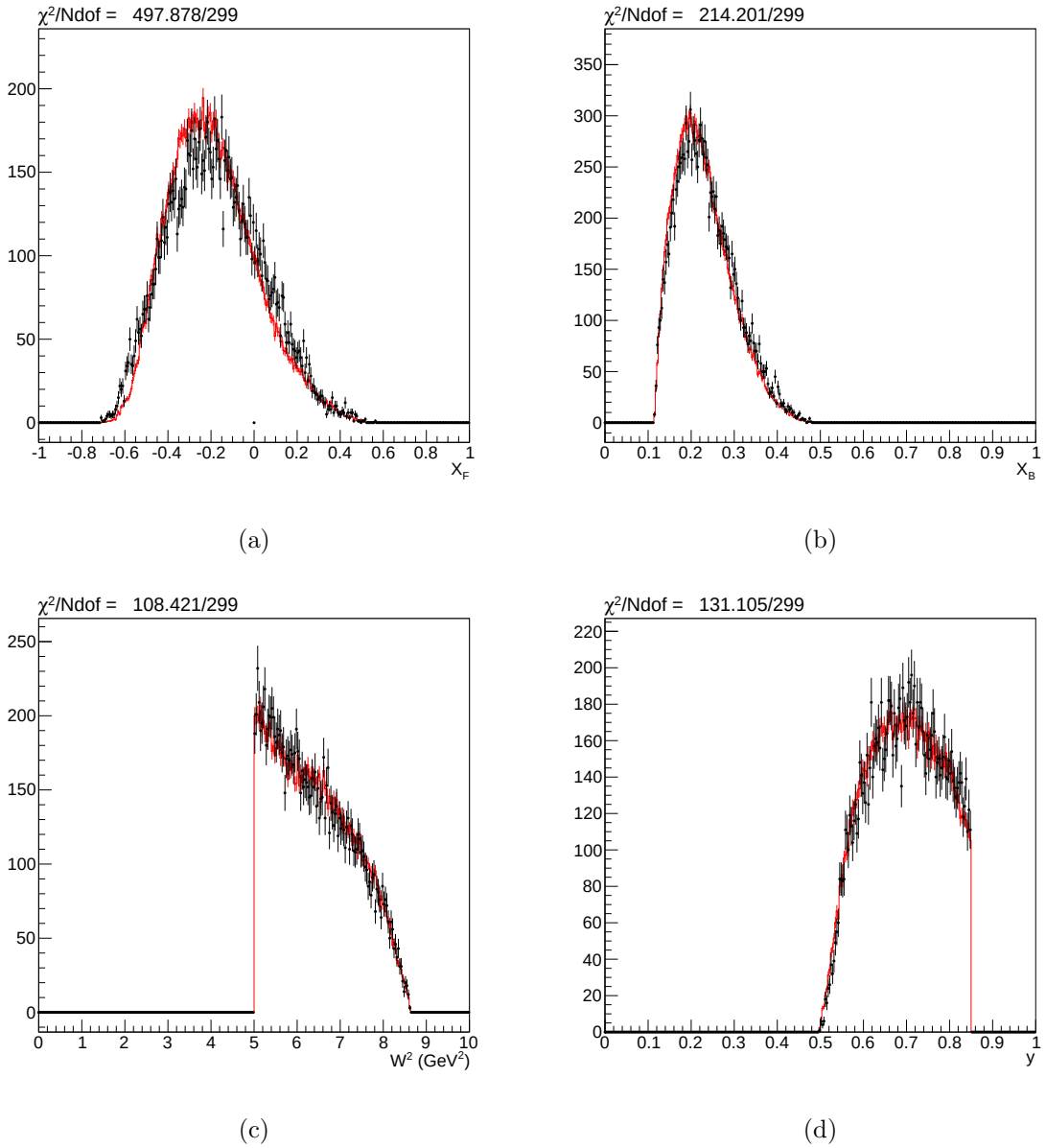

Figure 4.4: *Comparison of Monte Carlo (red) and experimental data (black) observed kinematics after all particle identification and detector acceptance cuts for a) Feynman-x (x_F), b) Bjorken-x (x_B), c) W^2 and d) y.*

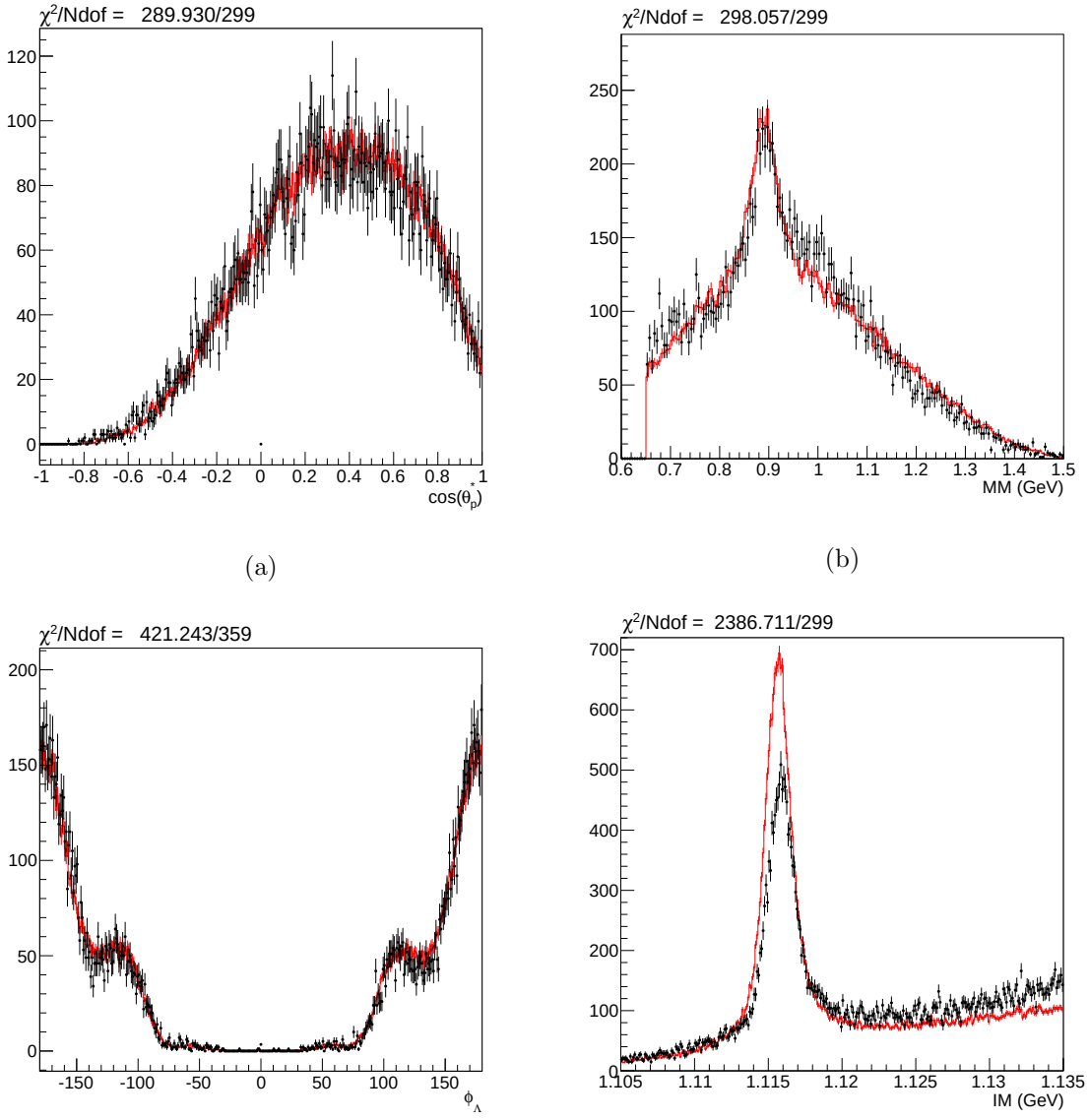

Figure 4.5: *Comparison of Monte Carlo (red) and experimental data (black) observed kinematics after all particle identification and detector acceptance cuts for a)* $\cos(\theta_p^*)$ *or* $\cos(\theta_z^p)$ *, b) Missing Mass (MM) c)* ϕ_Λ *and d)* Λ *invariant mass* $(p\pi^-)$ *.*

4.5 Summary

In this chapter the details of the Monte Carlo were introduced along with a comparison of observable Monte Carlo and experimental kinematics which illustrate excellent agreement, thus, demonstrating that the Monte Carlo effectively replicates real experimental conditions. The next chapter deals with the extraction of the Λ polarisation using the BSA and MLE methods with experimental and Monte Carlo data along with systematic studies.

Chapter 5

Measurement of Λ polarisation

In chapter 1 it was shown that the Λ polarisation coefficient (D^{LL}) is proportional to a ratio of Fracture Functions which directly relate to Transverse Momentum Distributions. This chapter is dedicated to discussing the means by which two polarisation extraction procedures (Beam Spin Asymmetry(BSA) and Maximum Likelihood(ML)) can extract this polarisation coefficient (D^{LL}). The methodologies of each will be discussed along with their results for various observable kinematics discussed in section 3.4. Finally systematic checks of the Λ background estimation for both procedures will be discussed along with a discussion of the Λ polarisation extraction method.

5.1 Beam Spin Asymmetry Method (BSA)

Subsequent to all particle identification and detector acceptance selection procedures all final state particles of interest are identified (electron, proton and π^-) in the laboratory rest frame.

Since the Λ polarisation can be directly measured through the angular distribution of its weak decay $\Lambda \to p\pi^-$, all proton angular distributions must be calculated in the Λ rest frame as this is the frame in which the Λ polarisation is defined. Thus, a set of Lorentz transformations are utilised to find the energy and momenta of all final state particles in the centre of mass frame

(CM) of the virtual photon and target proton. The proton angular distribution can be written as [92]

$$\frac{dN}{d\cos\theta_p^*} \propto 1 + \alpha P_\Lambda \cos\theta_p^* \tag{5.1}$$

Where $\cos\theta_p^*$ is the proton emission angle in the Λ rest frame and P_Λ the Λ polarisation, both projected onto the relevant axis with N the number of events. The used reference frame has the $\hat{z}$ axis along the virtual photon direction, the $\hat{y}$ axis normal to the scattering plane and $\hat{x} = \hat{y} \times \hat{z}$. The weak decay constant(α) is $\alpha = 0.642 \pm 0.013$ [93].

As mentioned in Section 1.1, the three components of the polarisation vector can be decomposed as an induced and transferred contribution

$$P_{\Lambda,i} = P_i^I + hP_i^T \tag{5.2}$$

Where $i = x, y, z$ and $h = \pm 1$ is the electron beam helicity.

The Λ polarisation can then be extracted via the forward-backward asymmetry from the proton angular distributions with respect to $\cos\theta_p^*$. The transferred part of the Λ polarisation can be measured by computing the beam spin asymmetry

$$A(\cos\theta_p^*) = \frac{N^+ - N^-}{N^+ + N^-} = \alpha P_i^T \cos\theta_p^* \tag{5.3}$$

Where, $\frac{N^+ - N^-}{N^+ + N^-}$ is the forward backward asymmetry and $N^{(+/-)}$ is the number of (positive/negative) helicity state events in the data set. Thus, fitting a $\cos\theta_p^*$ dependence on the asymmetry, P_i^T is able to be extracted.

A requirement of this procedure is that the events have to be grouped into bins with sufficiently high statistics. To implement Equation 5.3, the Λ invariant mass distribution (Figure 3.28) has to be grouped into $\cos(\theta_p^*)$ and x_F bins (specific values of these bins are given in Tables 3.6 and 3.7) for the different helicity conditions (positive or negative). Figures 5.1 and 5.2 represent the Λ invariant mass (IM) distributions for $\cos(\theta_p^*)$ bin = 4 and x_F bin = 5 for positive and

negative helicity states respectively. A full comparison of all the Λ IM distributions for different $\cos(\theta_p^*)$ bins and helicity states for all x_F bins can be found in Appendix D.

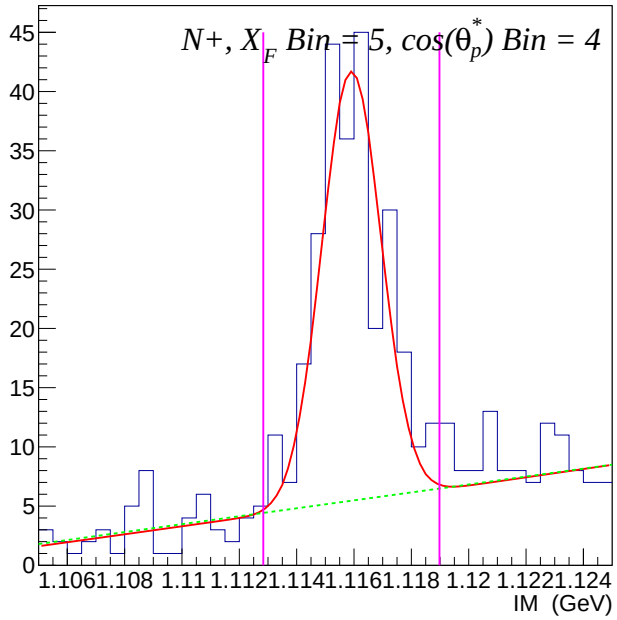

Figure 5.1: *Specific Λ invariant mass fit for Asymmetry calculation. This is for a positive helicity with* $\cos(\theta_p^*)$ *bin 5 and* x_F *bin 6. Red line is the combination of the Gaussian plus 2nd order polynomial with the green dashed line the background. Magenta lines illustrate the* 3σ *Λ invariant mass cuts.*

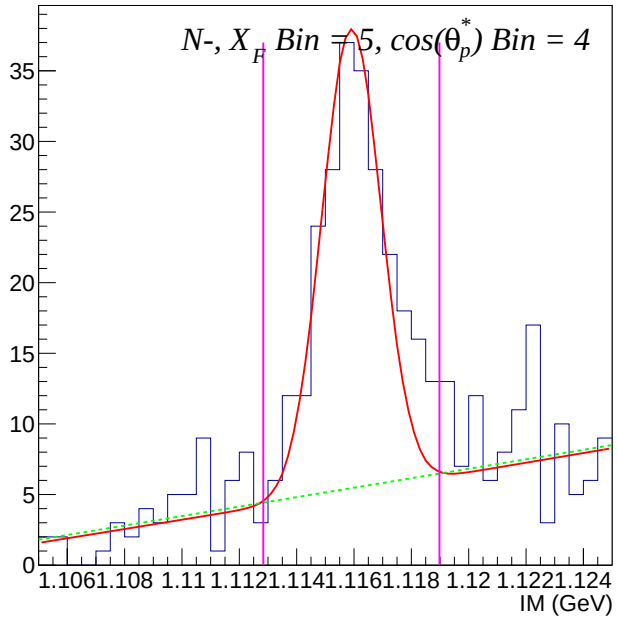

Figure 5.2: *Specific* Λ *invariant mass fit for Asymmetry calculation. This is for a negative helicity with* $\cos(\theta_p^*)$ *bin 5 and* x_F *bin 6. Red line is the combination of the Gaussian plus 2nd order polynomial with the green dashed line the background. Magenta lines illustrate the* 3σ Λ *invariant mass cuts.*

In order to extract a signal a Gaussian plus 2nd order polynomial is fitted to the invariant mass specific bin. The signal region is defined as the number of events within the 3 sigma cuts (the magenta lines) minus the integral of the polynomial (dashed green line) which equates to the background. However in the specific bin, either positive or negative helicity, if the contributions do not have high enough statistics the bin is is neglected. Therefore, a final signal event number for both positive (N^+) and negative (N^-) helicity states can be extracted to be used to calculate the forward-backward asymmetry component $A(\cos\theta_p^*)$ in Equation 5.3.

To convert from P_i^T to D^{LL}, Equation 1.27, the depolarisation factor $D(y)$ and beam polarisation P_B have to be considered. Figure 5.3 illustrates $D(y)$ against $\cos(\theta_p^*)$ for specific x_F bins. The beam polarisation was taken to be to be 0.74, section 2.2.

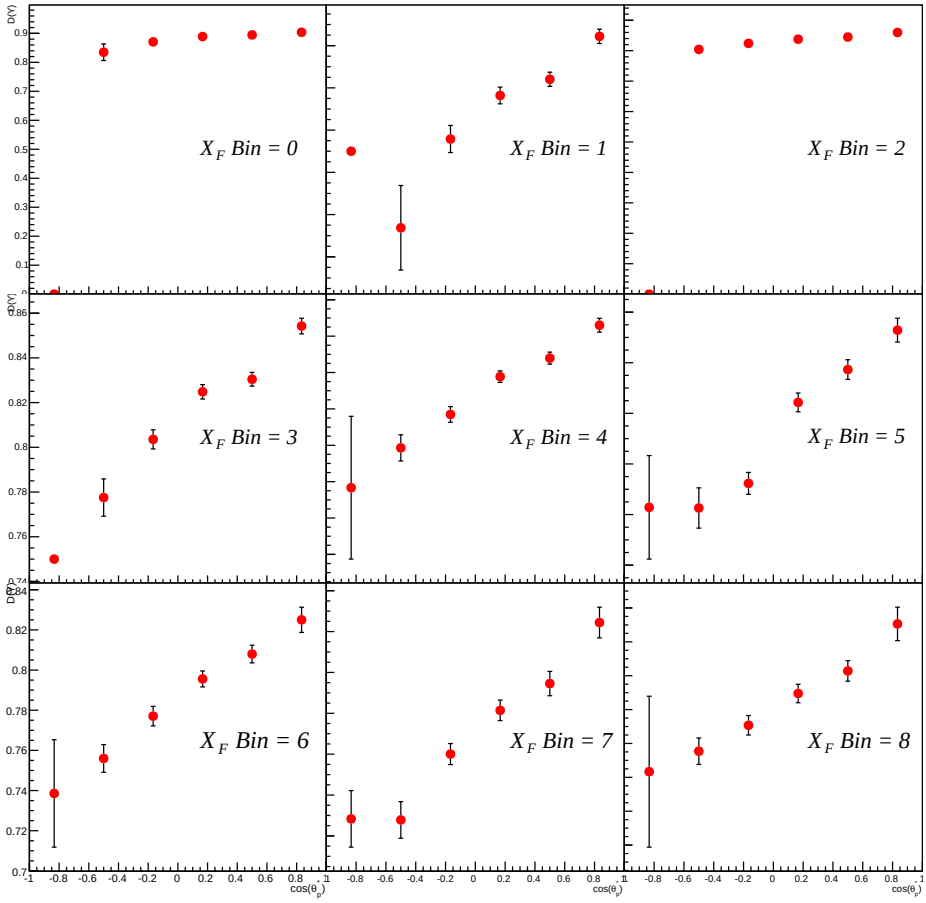

Figure 5.3: *Depolarisation factor $D(y)$ against $\cos(\theta_p^*)$ for specific x_F bins. Values of $D(y)$ for each $\cos(\theta)$ and x_F bin are used to covert from P_i^T to D^{LL}.*

After division by $D(y)$ and P_B for each asymmetry point for a specific $\cos(\theta_p^*)$ and x_F bin, Figure 5.4 is produced which illustrates the forward/backward asymmetry against $\cos(\theta_p^*)$ for various x_F bins. From Equation 5.3 a first order polynomial (with a fixed constant of zero) can be fitted to each x_F bin (red line) and the gradient extracted. This gradient represents the transferred polarisation component (D^{LL}) in Equation 1.36 and is illustrated in Figure 5.5 against x_F.

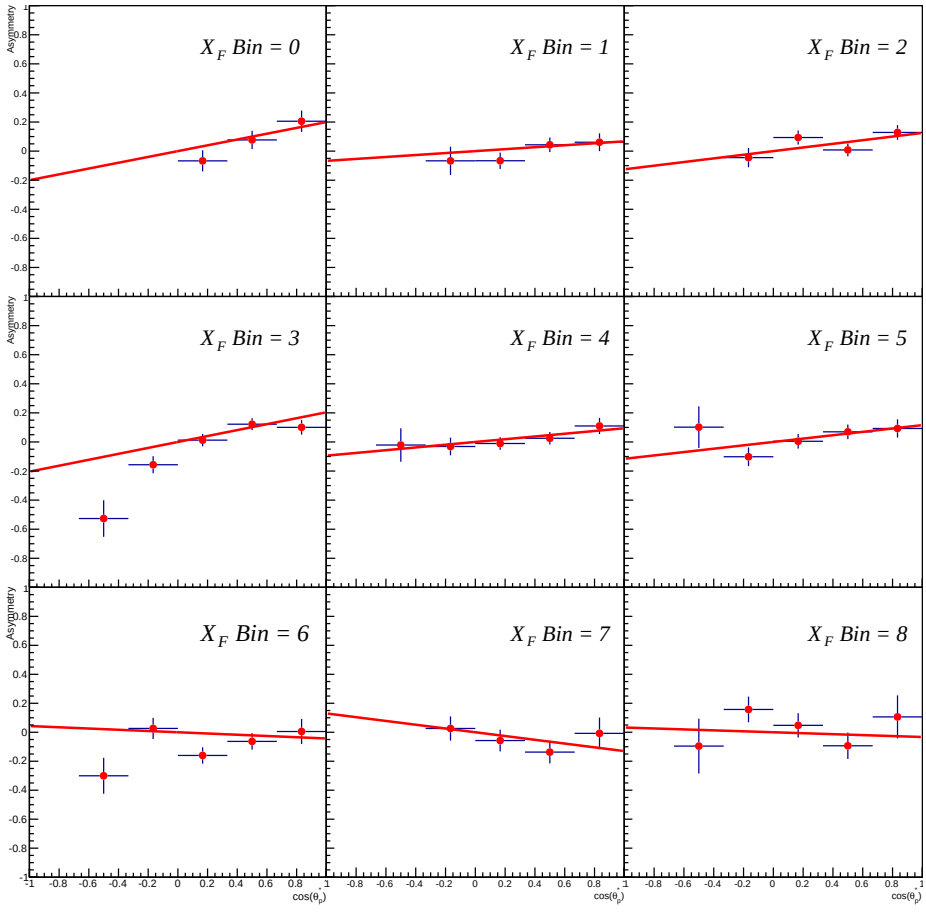

Figure 5.4: *Fit of 1st order polynomial (red line) to extract D^{LL} or gradient for all x_F bins.*

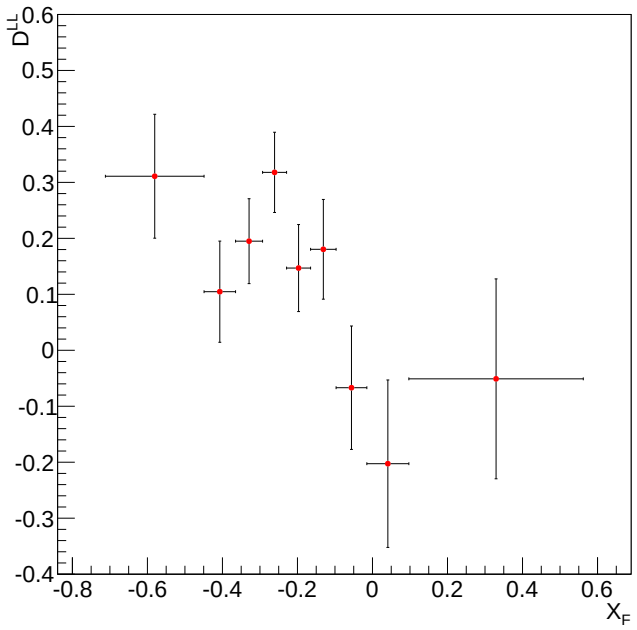

Figure 5.5: *Longitudinal transferred* Λ *polarisation coefficient as a function of* x_F.

We can note a large polarisation (up to 30%) in the TFR, while the polarisation is compatible with zero within 1σ in the CFR. The transferred polarisation against other observed kinematics (Section 1.3.2) are illustrated in chapter 6 with the plots for extracting the helicity component asymmetry parameters detailed in Appendix D.

5.1.1 Λ Transferred Polarisation in Missing Mass

Since the performed analysis is conducted via semi-inclusive channel one can select specific regions of interest in the Missing Mass and hence contributions from specific final states (namely K^+ or $K*$). This enables the missing mass region (X_{MM}) to also be examined using the same Beam Spin Asymmetry (BSA) method as detailed in Section 5.1.1. The particle and event selection procedure is consistent with chapter 3 with the Missing Mass cut:

•$MM > 0.3\ GeV$.

Therefore, using the same BSA procedure the transferred polarisation component against X_{MM} is illustrated below in Figure 5.6b with the Missing Mass distribution illustrated in Figure 5.6a. It is evident, from Figure 5.6b, that there is a high positive transferred polarisation for the K^+ the region and a less positive contribution for K^*.

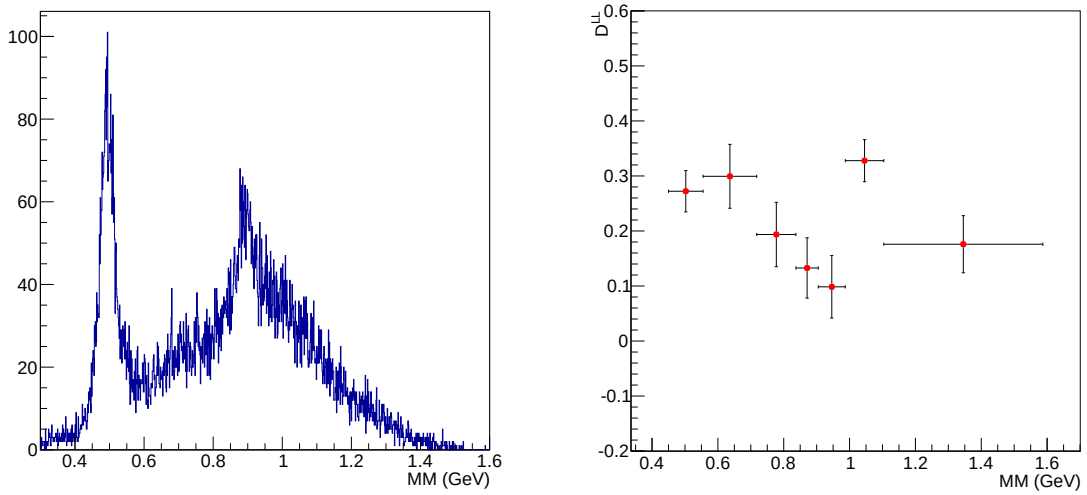

(a) (b)

Figure 5.6: *Missing Mass (MM) distribution (a) and transferred polarisation as a function of MM (b) integrated across all x_F.*

5.1.2 cos(ϕ) contribution to transferred polarisation

From Section 1.4 the transferred contribution for the $i = z$ component of the Λ polarisation is represented by (Equation 1.35):

$$P^T_{\Lambda,z} = D^0_z + D^c_z \cos\phi \tag{5.4}$$

Given Equation 5.4, integrating equates to D^0_z for uniform ϕ coverage. Since this is not the case (Figure 3.30d), the contribution from the z component of $\cos\phi$ in Equation 5.4 to

5.1.2 cos(ϕ) contribution to transferred polarisation

the transferred polarisation has be to studied. Since the statistics are low the procedure to evaluate this involved selecting two separate $\cos\phi$ regions (two kinematical bins) and the BSA method (Section 5.1.1) implemented to extract transferred polarisation against $\cos(\phi)$. The same method was conducted in both regions using the same particle identification and events selection procedure as stated in chapter 3. Figure 5.7 illustrates the selected regions termed A and B. The regions were defined as follows:

$$A = 90^\circ < |\phi_\Lambda| < 140^\circ \qquad\qquad B = 140^\circ < |\phi_\Lambda| < 180^\circ \tag{5.5}$$

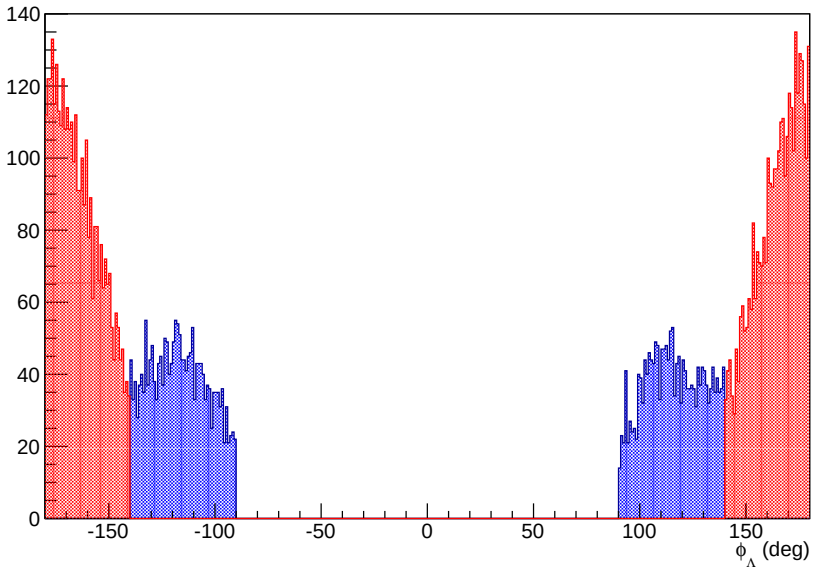

Figure 5.7: ϕ_Λ *distributions for Region A (blue histogram) and Region B (red histogram)*

Implementing the Beam Spin Asymmetry polarisation extraction on the two regions to extract the transferred z-component of Λ polarisation, as explained in Section 5.1.1, in the two regions (A and B) yields:

$$A : P^T_{\Lambda,z,A} = 0.18 \pm 0.04 \tag{5.6}$$

$$B : P^T_{\Lambda,z,B} = 0.21 \pm 0.029 \tag{5.7}$$

5.1.2 cos(ϕ) contribution to transferred polarisation

Therefore, from Equation 5.4 we have the series of equations for the different cos(ϕ) regions:

$$P^T_{\Lambda,z,A} = D^0_z + D^c_z < \cos\phi_A > \tag{5.8}$$

$$P^T_{\Lambda,z,B} = D^0_z + D^c_z < \cos\phi_B > \tag{5.9}$$

Where $< \cos\phi_A >$ = -0.44 and $< \cos\phi_B >$ = -1.0.

Hence, solving simultaneous equations (Equation 5.8 and 5.9), propagating errors through and rearranging for D^0_z and D^c_z:

$$D^0_z = 0.16 \pm 0.08 \tag{5.10}$$

$$D^c_z = -0.05 \pm 0.08 \tag{5.11}$$

From equations 5.10 and 5.11, the D^c_z component is zero within errors compared to D^0_z. It is therefore possible for us to note that $D^{LL} \propto D^0_z$ and the cos(ϕ) component of the transferred polarisation (Equation 1.35) is negligible compared to the first term D^0_z.

5.2 Maximum Likelihood Estimation method (MLE)

Another method of extracting the transferred components of the polarisation of the Λ is achieved through the unbinned Maximum Likelihood Estimation method (MLE). Since no binning is performed the MLE provides results with higher statistical precision, especially in the case of relatively limited statistics. This in combination with and event-by-event likelihood function overcomes some of the shortcomings of the binned beam spin asymmetry fit (BSA).

Maximum likelihood is a technique that calculates observable values that make fit the data most closely or maximise the probability of the fit [94] [95]. The method is determined by considering a set of M vectors $\vec{x_i}$, with each vector representing an event i. The method assumes the events are distributed according to a probability density function (pdf) $f(\vec{x_i};\vec{\psi})$ [96], where $\vec{\psi} = (\psi_1, ..., \psi_n)$ are a set of unknown parameters to be determined. The maximum likelihood technique then calculates the values of $\vec{\psi}$ by maximising the likelihood function (Equation 5.12) using the product of a sequence:

$$\mathcal{L}(\vec{\psi}) = \prod_{i=1}^{M} f(\vec{x_i};\vec{\psi}) \tag{5.12}$$

Maximum likelihood is a simple method of estimation, with no loss from binning, invariance under parameter transformation and suitable for calculations with multiple unknown parameters. The maximisation package utilised in this analysis was TMinuit found in the ROOT framework [97] to minimise the negative of the likelihood (or log(likelihood)) function -2 log $\mathcal{L}$. A benefit of the log(likelihood) function is that the product in Equation 5.12 can be replaced by a sum, making the calculation more simple.

In simple examples of the Maximum Likelihood extraction method [95] a normal distribution is used as the pdf, which has the property of being normalised to unity. In the case of an arbitrary pdf $f(\vec{x_i};\vec{\psi})$ and normalisation, the likelihood function can be expressed by:

$$\mathcal{L}(\vec{\psi}) = \frac{\prod_{i=1}^{M} f(\vec{x_i};\vec{\psi})}{[\mathcal{N}(\vec{\psi})]^M} \tag{5.13}$$

Where, the normalisation integral of the pdf is given by:

$$\mathcal{N}(\vec{\psi}) = \int f(\vec{x_i};\vec{\psi})d\vec{x} \tag{5.14}$$

In the example of the proton angular distribution being the pdf for the polarised Λ, it can therefore be written as:

$$f(\vec{x_i};\vec{\psi}) \propto 1 + \alpha P_{\Lambda}^{\vec{\psi}} \cos(\theta_p^*) \tag{5.15}$$

Where $\vec{\psi}$ describes the induced and transferred parameters of the Λ polarisation, section 1.4, and $\vec{x_i}$ contains all the observed kinematics variables such as x_F, the proton decay angle (θ_p^*) and the azimuthal angle (ϕ_Λ).

The Λ polarisation is extracted with a mixed procedure: fit the global ϕ_Λ dependence of the Λ polarisation into fixed kinematic bins. The chosen bins were the same as utilised in the BSA case (Tables 3.6 and 3.7) for consistency. Therefore, in each bin the pdf (not normalised) can be written as:

$$f(\cos(\theta_p^*)_i, \int (\phi_\Lambda)_i, \vec{\psi}) = 1 + \alpha P_{\Lambda}^{\vec{\psi}}((\phi_\Lambda)_i) \cos(\theta_p^*)_i \tag{5.16}$$

The log(likelihood) function can then be separated into two contributions: one from events with positive helicity states (M^+) and the other with negative helicity states (M^-) of the incident electrons. This is expressed by:

$$\log(\mathcal{L}) = \sum_{i=1}^{M^+} \log(f_i^+) + \sum_{i=1}^{M^-} \log(f_i^-) - M^+ \log(\mathcal{N}^+) - M^- \log(\mathcal{N}^-) \tag{5.17}$$

Where, $\mathcal{N}^{+,-}$ and $f^{+,-}$ are the normalisation integral and pdf from the two helicity states respectively.

5.2.1 Normalisation of the Probability Density Function (pdf) for MLE

For small datasets there can be a bias inflicted on the results which make the results either consistently above or below the true value, this can be fixed by incorporating a normalisation. If the data is unpolarised the number of positive and negative helicity events are the same and the normalisation integral (Equation 5.14) will not depend on the observed kinematics or parameters ($\vec{\psi}$) and can therefore be rejected from the likelihood equation. In our scenario this is not the case and the normalisation therefore has to be taken into account. The solution adopted [98] [99] was to calculate the pdf normalisation integral by using the Monte Carlo data in the manner:

$$\mathcal{N}^{+,-} = \sum_{i=1}^{M} f_i^{+,-} \tag{5.18}$$

Where this event by event procedure is ran over events i to total event number M for positive and negative $(+,-)$ helicity states for the pdf f for the Monte Carlo data.

5.2.2 Background estimation and incorporation into MLE

As demonstrated before, the Λ invariant mass peak (Figure 3.28) has a signal and background region lying on top of each other. This needs to be taken into consideration to extract the true Λ polarisation signal. The experimental likelihood product in Equation 5.12, can be separated into two distinct parts. One for the signal (true Λ events) and the other for the background (non Λ events). This enables the likelihood equation to be changed to:

$$\mathcal{L} = \mathcal{L}^{signal}.\mathcal{L}^{background} = \prod_{i=1}^{M_{signal}} f_i . \prod_{j=1}^{M_{background}} f_j \tag{5.19}$$

Where i are events in the signal region and j in the background with total event numbers M_{signal} and $M_{background}$.

5.2.2 Background estimation and incorporation into MLE

The procedure to subtract the background contamination from the likelihood product is performed by dividing out the contribution of $M_{background}$ events, which are taken from the side-band region of the Λ peak:

$$\mathcal{L} = \mathcal{L}^{signal}.\mathcal{L}^{background} = \prod_{i=1}^{M_{signal}} f_i. \prod_{j=1}^{M_{background}} f_j.(\prod_{k=1}^{M_{background}} f_k)^{-1} \tag{5.20}$$

Where the sum index over k are events located in the side band region. Figure 5.8 illustrates the side band region (red) which was defined as having the same number of events as in the background estimation of the BSA case, demonstrated in Figure 3.28 (namely the integral of the polynomial).

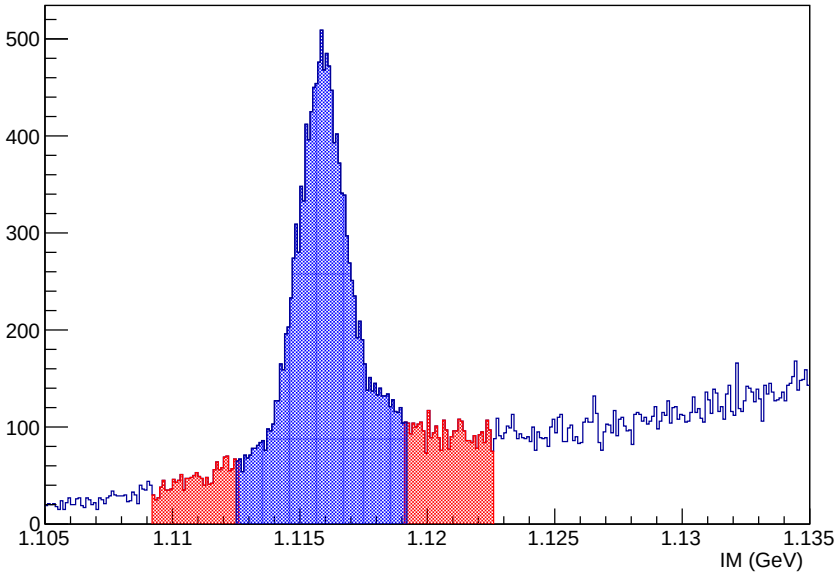

Figure 5.8: *Invariant Mass distribution of the proton and π^-, to be used in the background subtraction procedure for the maximum likelihood method. Side band region (red) was defined as having the same number of events as in the background subtraction procedure of the BSA which used the peak region (blue).*

The hypothesis is that the background events in the side band region (Figure 5.8, red) have the same distribution and make up of the background events in the peak region (Figure 5.8,

5.2.2 Background estimation and incorporation into MLE

blue) . Therefore utilising this method enables $\mathcal{L} = \mathcal{L}^{signal}$. The benefit of using logarithms is evident here as a division becomes a subtraction.

Finally, the log(likelihood) function with background subtraction and normalisation that is utilised in the Maximum Likelihood extraction procedure is written as:

$$\log(\mathcal{L}) = \sum_{i=1}^{M_P+M_{side}} w_i \log(f_i) - \Big(\sum_{i=1}^{M_P+M_{side}} w_i\Big) \log(\mathcal{N}) \tag{5.21}$$

Where the weight (w_i) is assigned +1 for events in the peak region (p) and -1 for events in the side band region ($side$), thus subtracting out the background contamination. As done for Equation 5.17, the log(likelihood) equation can be split further into contributions for the two helicity states.

Figure 5.9 below illustrates the final longitudinal transferred Λ polarisation coefficient (D^{LL}) (z-component in the γp centre-of-mass frame) as a function of x_F using the MLE procedure as detailed above. Chapter 6 details the longitudinal transferred Λ polarisation coefficient (D^{LL}) against various other observable kinematics as described in section 1.3.2.

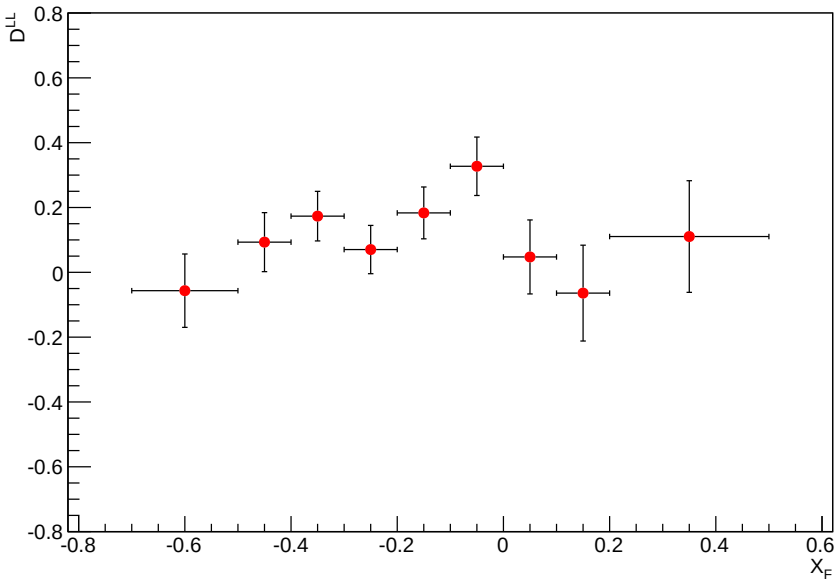

Figure 5.9: *Longitudinal transferred Λ polarisation coefficient (D^{LL}) as a function of x_F. Normalisation and background subtraction have both been incorportated*

5.3 Systematic studies and background analysis

The Monte Carlo allows systematic studies to be performed into the Beam Spin Asymmetry (BSA) polarisation extraction method. The method is tested by directly injecting a polarisation (helicity) into the reconstructed Monte Carlo and extracting the polarisation by the BSA procedure, section 5.1.1. This is performed by randomly generating a helicity dependent event, given the induced polarisation, and performing the Asymmetry calculation based on these synthetic events.

This is performed by defining the ratio ($R = \frac{N^+}{N^-}$) or probability (P) of the different helicity state events which unfolds from Equation 5.3 as:

$$P(\cos\theta_p^*) = R = \frac{1 + A(\cos\theta_p^*)}{1 - A(\cos\theta_p^*)} \tag{5.22}$$

Where,

$$A(\cos\theta_p^*) = \alpha P_{inj} \cos\theta_p^* \tag{5.23}$$

In Equation 5.23, P_{inj} is the injected polarisation and the other variables have their usual meaning.

Thus, by filling histograms dependent upon their $cos\theta_p^*$ and helicity dependence the probability (P) that the event was produced by an electron with helicity (h) is given randomly by extracting a number in the range -1 to 1. If the number is in the range -1 to 0 it is deemed to be negative ($h = -1$) and if it it is in the range 0 to 1 positive ($h = +1$) for that specific $cos\theta_p^*$ value.

This method was used to produce the distributions of the helicity and $\cos\theta_p^*$ dependent Λ invariant mass distributions that were subsequently used in the Beam Spin Asymmetry method (BSA) polarisation extraction, section 5.1. This polarisation extraction procedure enables the transferred longitudinal polarisation (D^{LL}) as a function of x_F to be determined. Performing this analysis multiple times, for the same injected polarisation, enables a systematic study of the BSA procedure to be conducted. In this analysis 100 trials were conducted, on an injected

polarisation of 0.4, 0.6 and 0.2, and to each a Gaussian is fitted to extract the mean(μ) and sigma(σ) for each specific x_F bin. Figure 5.10 illustrates the Gaussian fit for $x_F = 0.35$ for an injected polarisation of 0.4.

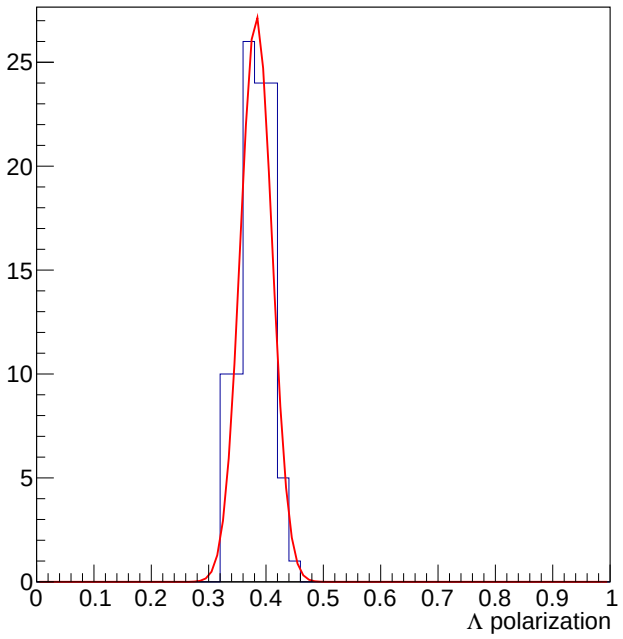

Figure 5.10: *Overall polarisation for* $x_F = 0.35$. *Gaussian is fitted to extract mean* ($\mu = 0.382$) *and sigma* ($\sigma = 0.027 \pm 0.002$).

From the mean(μ) from each x_F bin the average polarisation can be extracted. Figure 5.11 illustrates the average transferred polarisations against x_F with a zero order polynomial fitted to extract the average transferred polarisation. Comparison between the injected polarisation and extracted values highlights an excellent agreement and demonstrates that polarisation extraction with the BSA method is an appropriate technique to use.

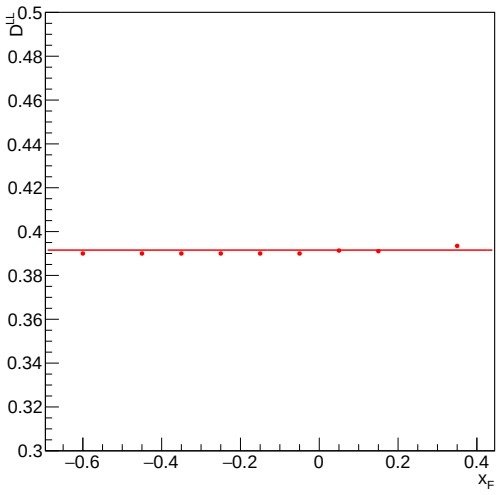

(a) *Systematic transferred polarisation against x_F for injected polarisation of 0.4. Fitted zero order polynomial:* 0.391 ± 0.006.

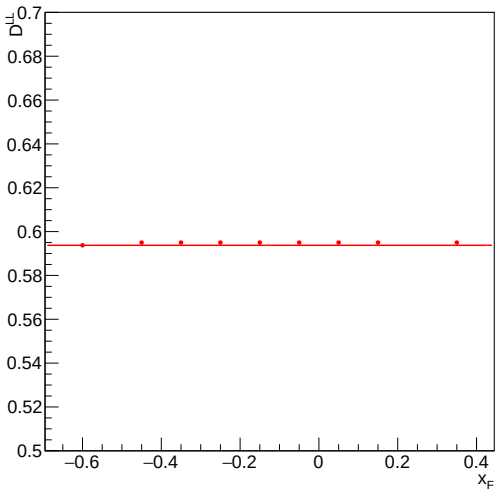

(b) *Systematic transferred polarisation against x_F for injected polarisation of 0.6. Fitted zero order polynomial:* 0.596 ± 0.007.

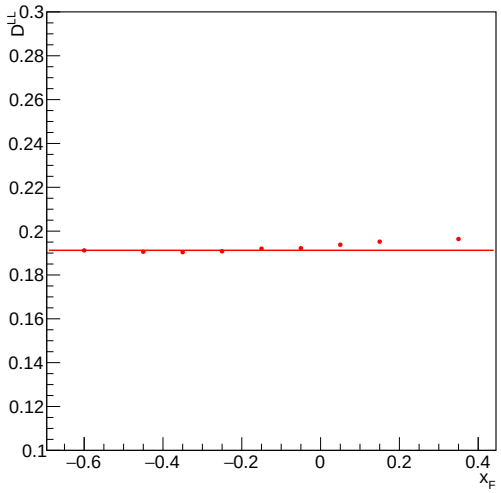

(c) *Systematic transferred polarisation against x_F for injected polarisation of 0.2. Fitted zero order polynomial:* 0.193 ± 0.001.

Figure 5.11: *Systematic transferred polarisation extractions using the BSA method for different injected polarisations.*

In both the BSA and MLE methods to extract the Λ polarisation a background subtraction had to be considered to take into account the non-Λ events under the peak, Figure 3.28. In the BSA case this was performed by fitting the invariant mass peak with a polynomial and integrating. In the case of the maximum likelihood this was performed by a side band analysis, section 5.2.2. A comparison of the two methods will now be made enabling the background estimation procedure for both techniques to be demonstrated, Figure 5.12. A zero order polynomial was fitted to both techniques to evaluate the average polarisation coefficient (D^{LL}) in all x_F, Equation 5.24. The results illustrate that for both the MLE and BSA methods the polarisation is negligible in the background regions.

$$BSA : 0.08 \pm 0.06 \qquad MLE : -0.03 \pm 0.05 \tag{5.24}$$

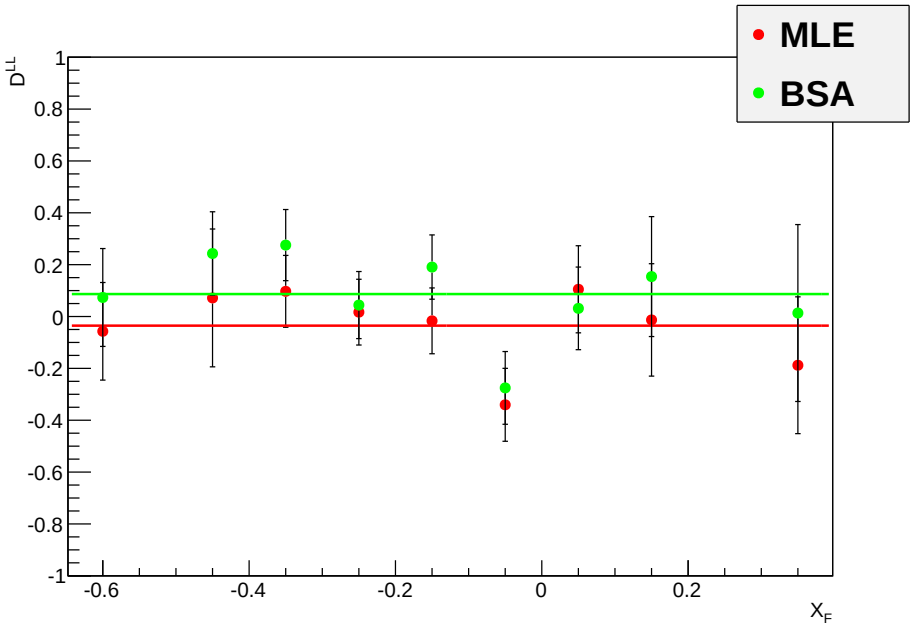

Figure 5.12: *Longitudinal transferred* Λ *polarisation coefficient* (D^{LL}) *as a function of* x_F *in the background (non-*Λ*) region for the two procedures: BSA (Green) and MLE (Red).*

5.4 Summary

In this chapter, two different methods of polarisation extraction were discussed and compared: Beam Spin Asymmetry (BSA) and Maximum Likelihood Estimation (MLE). These methods were both shown to provide a suitable framework for extracting the polarisation coefficient D^{LL}. In addition, systematic checks were performed that showed that the proton angular distribution function is excellent in representing the polarisation extraction function. Concluding this chapter was a comparison of the two background estimation procedures implemented in both techniques. In the final chapter results will be compared with theoretical predictions and previous measurements along with a discussion and overview of the analysis.

Chapter 6

Results and Conclusion

The current analysis has been explained by discussing the theoretical framework of nucleon structure, in particular the proton, and more specifically a semi-inclusive Λ electroproduction polarisation extraction in the TFR. In this chapter the final results are presented and compared to theoretical model predictions and previous measurements with a summary concluding the work.

6.1 Results

The Beam Spin Asymmetry (BSA) and Maximum Likelihood Extraction (MLE) methods used to extract the transferred Λ polarisation coefficient D^{LL} were detailed in chapter 5. A comparison of those results with previous measurements and theoretical predictions, namely the Intrinsic Strangeness Model (ISM) [100] will be illustrated. In the ISM the hadronisation of the quarks and the target nucleon remnants into hadrons are modelled with the Lund string model as implented in the JETSET 7.4 code [101] [102]. Deep-inelastic lepton-nucleon scattering is simulated using the LEPTO 6.1 package [103] with parton distributions provided by the PDFLIB package [104].

Figures 6.1 to 6.7 illustrate the transferred Λ coefficient (D^{LL}) as a function of various observable measurable kinematics detailed in section 1.3.2. The measurements in this analysis for the BSA are given in green (circles), with the MLE in red (circles).

In Figure 6.1 the measurements for the TFR are generally consistent with the Intrinsic Strangeness Model (ISM) predictions within errors. For $x_F = -0.6$, even with the large statistical errors, the results seem inconsistent for the two polarisation extraction methods. This is not understood, however, the other points are similar for the two methods within errors. In the CFR the measurements are consistently below the ISM prediction but in most cases within errors. In comparison to previous results in the TFR the measurements from this analysis are compatible with Nomad's [60] predictions again except the MLE measurement for $x_F = -0.6$. In the CFR the MLE measurements are more negative than the BSA, but comparable within errors and generally more compatible with the measurement from Hermes [62]. However, it should be noted that statistics in the CFR for this analysis were limited, Figure 3.31a, and as such the primary objective was a TFR measurement.

In Figure 6.2 the polarisation coefficient D^{LL} is illustrated against x_B, with measurements compared to the ISM. Again results are comparable to the ISM except for $x_B = 0.245$ for the BSA method. In the subsequent Figures 6.3 to 6.7, no theoretical models or previous measurements are present and they are a direct comparison of the two polarisation extraction techniques.

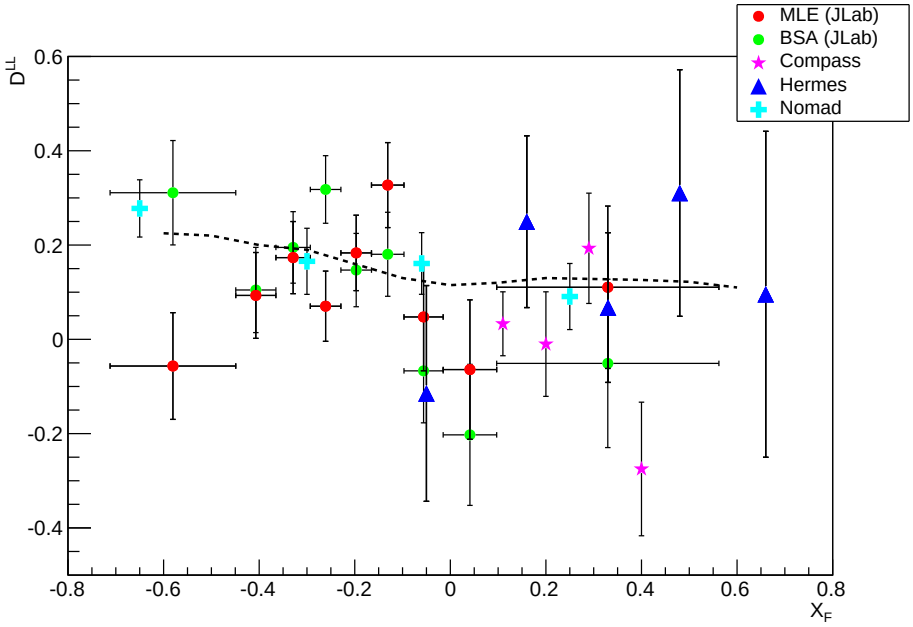

Figure 6.1: *Comparison of longitudinal transferred* Λ *polarisation coefficient* (D^{LL}) *as a function of* x_F *for the two procedures: BSA (Green) and MLE (Red). Black dashed line is the Intrinsic Strangeness Model (ISM) prediction [100] along with previous experimental measurements from Nomad (turquoise) [60], Hermes (blue) [62] and Compass (magenta) [63].*

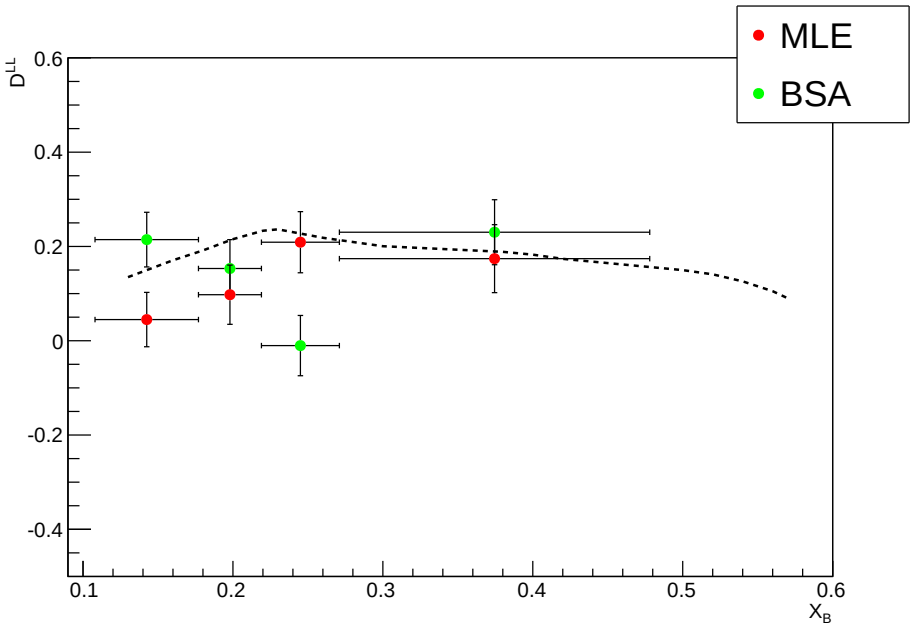

Figure 6.2: *Comparison of longitudinal transferred* Λ *polarisation coefficient* (D^{LL}) *as a function of* x_B *for the two procedures: BSA (Green) and MLE (Red). Black dashed line is the Intrinsic Strangeness Model (ISM) prediction.*

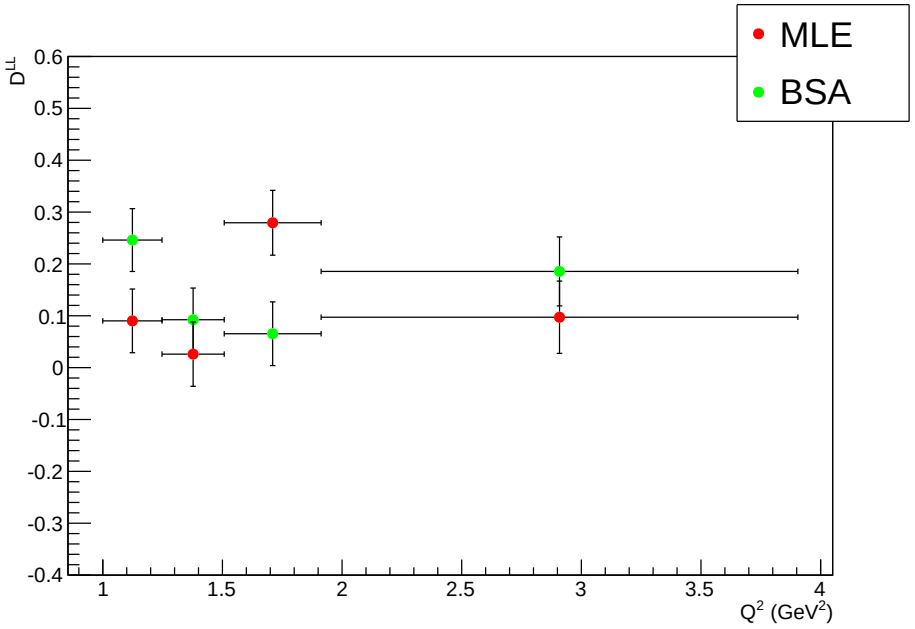

Figure 6.3: *Comparison of longitudinal transferred* Λ *polarisation coefficient* (D^{LL}) *as a function of* Q^2 *for the two procedures: BSA (Green) and MLE (Red).*

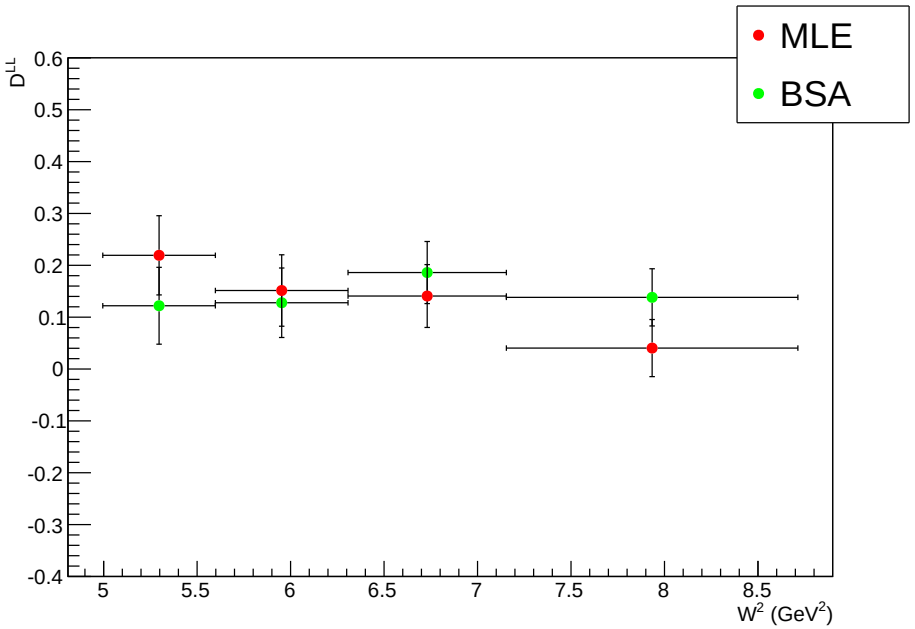

Figure 6.4: *Comparison of longitudinal transferred* Λ *polarisation coefficient* (D^{LL}) *as a function of* W^2 *for the two procedures: BSA (Green) and MLE (Red).*

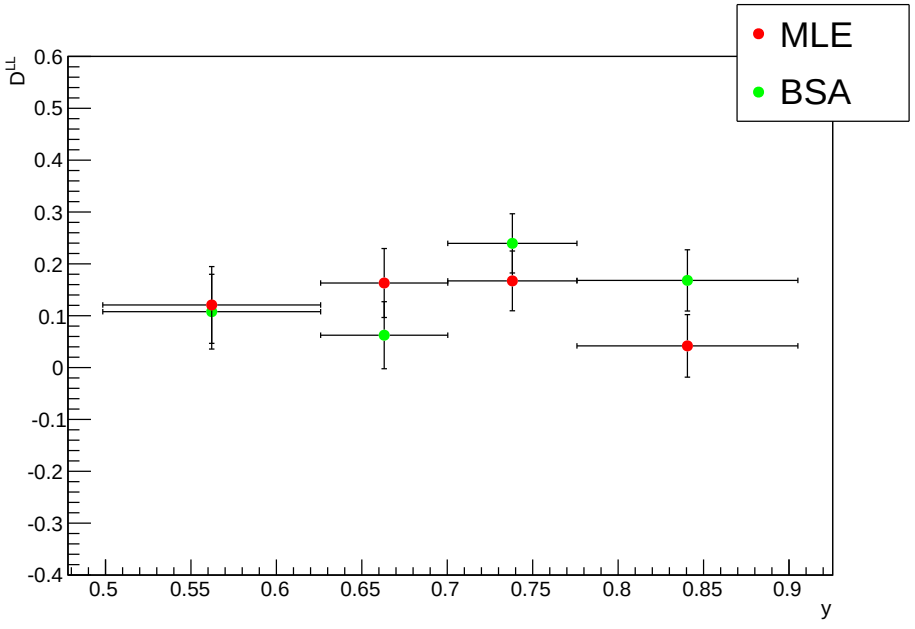

Figure 6.5: *Comparison of longitudinal transferred* Λ *polarisation coefficient* (D^{LL}) *as a function of* y *for the two procedures: BSA (Green) and MLE (Red).*

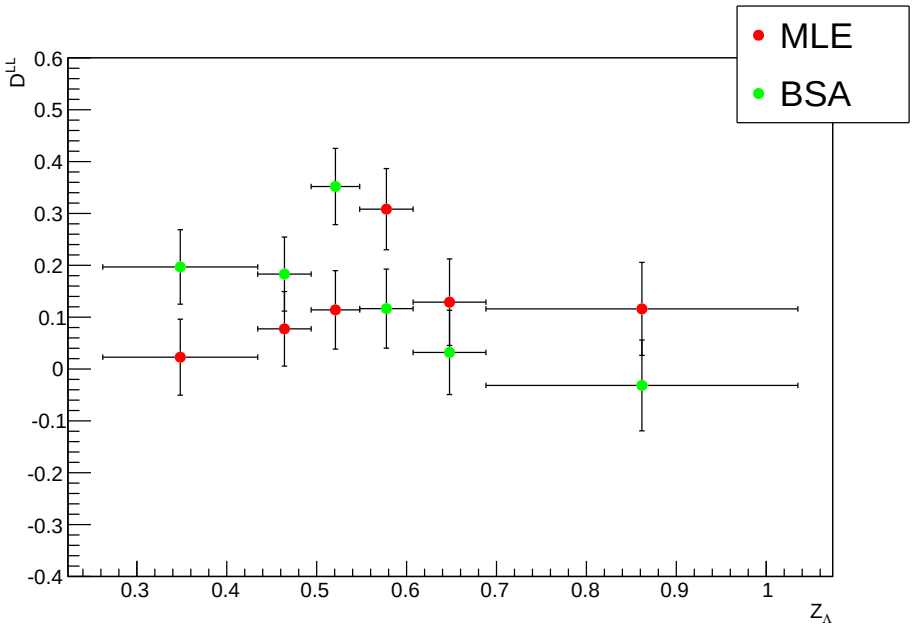

Figure 6.6: *Comparison of longitudinal transferred* Λ *polarisation coefficient* (D^{LL}) *as a function of* z_Λ *for the two procedures: BSA (Green) and MLE (Red).*

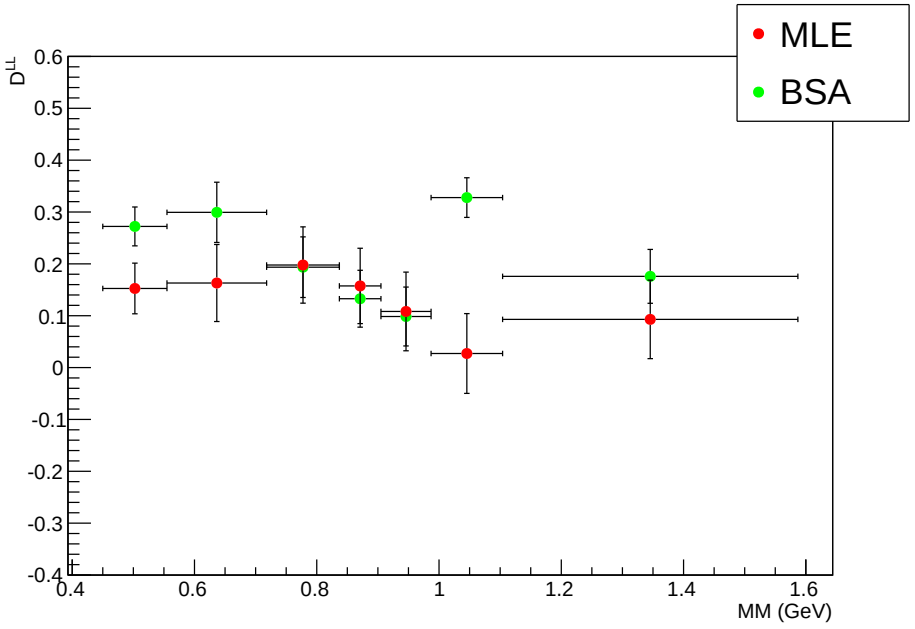

Figure 6.7: *Comparison of longitudinal transferred* Λ *polarisation coefficient* (D^{LL}) *as a function of MM for the two procedures: BSA (Green) and MLE (Red).*

6.2 Conclusion

This thesis presents the measurements of the transferred Λ polarisation coefficient D^{LL} in Semi Inclusive Deep Inelastic Scattering (SIDIS) using the Beam Spin Asymmetry (BSA) and Maximum Likelihood Extraction (MLE) methods. Measurements of the Λ polarisation in SIDIS experiments can provide information not only on the spin structure of the different baryons, but also on the nucleon strange sea. The polarisation extraction results are used to understand nucleon structure through the formalism of fracture functions.

The primary objective was to understand how D^{LL} varies with x_F, as this is the kinematic variable that separates the Target Fragmentation Region (TFR) from the Current Fragmentation Region (CFR). In the TFR the physics formalism is understood via Fracture Functions, which connect to D^{LL} via a ratio (Equation 1.36), whilst in the CFR it is illustrated with Transverse Momentum Dependent (TMD) Parton Distribution Functions (PDFs) and Fragmentation Functions (FFs). The results were shown in this chapter (Figures 6.1-6.7) along with model predictions and previous measurements. Comparison of the two polarisation techniques with the ISM model (Figure 6.1) highlights a relatively good comparison (neglecting the first x_F bin). With regards to previous measurements in the TFR, the only notable comparison comes in the form of data from Nomad [60], which is consistent with the findings from this analysis.

The data was recorded with the CLAS detector, chapter 2, at Thomas Jefferson National Laboratory in a dedicated run period titled e1f which was taken in 2003. The work conducted to reduce this data to a form suitable for this analysis i.e. $ep \rightarrow e'p\pi^- X$ was detailed in chapter 3 by identifying the final state particles and rejecting background processes by imposing certain restrictions.

The theoretical framework and background was detailed in Chapter 1 which gave an overview of nucleon structure and in particular the proton. This was described by introducing Wigner distributions which illustrate the three dimensional picture of the proton in terms of position

and momentum. Also evident was how Wigner distributions relate to TMDs and subsequently Fracture Functions via a SIDIS analysis. This thesis offers a new source of input into the Λ polarisation data set by offering a significant insight into the TFR which is not currently well analysed compared to the CFR. It is understood that work such as presented here will give a deeper insight and a more thorough understanding into the structure of the proton and may aid in the underlying questions of how the distributions of quarks and gluons inside the proton are composed. This is acheived through an anaylis of the polarisation coefficent D^{LL} which is related to proton composition through the theory of Fracture Functions. The final results in this thesis were incorporated into a proposal [110] for a future analysis studying the Λ polarisation using data from the upgraded CLAS12 detector [111] [112]. CLAS12, which will operate at an order of magnitude higher luminosity (10^{35}) to CLAS, will enable a deeper insight into nucleon structure by offering a wider range of experimental programs into regions of currently unexplored phase space and kinematics (i.e. X_B or Q^2).

Appendix A: TMD Parton distribution and Fragmentation Functions

TMD parton distribution functions (PDFs) (Table 1.1) are defined via the unintegrated quark-quark correlation function ($\Phi^q_{ij}(x, \mathbf{k}_\perp, \mathbf{S})$) [105] for a polarised nucleon (with spin $\mathbf{S}$, longitudinal fraction of the nucleon's momentum x and transverse momentum $k_\perp$). By Dirac projections the eight TMD PDFs for the nucleon [106] [107] [108] are:

$$\frac{1}{2}tr[\gamma^+\Phi^q_{ij}(x, \mathbf{k}_\perp, \mathbf{S})] = f^q_1(x, k_\perp) - \frac{\epsilon^{jk}k^j_\perp S^k_T}{M} f^{\perp q}_{1T}(x, k_\perp) \tag{6.1}$$

$$\frac{1}{2}tr[\gamma^+\gamma_5\Phi^q_{ij}(x, \mathbf{k}_\perp, \mathbf{S})] = S_L g^q_1(x, k_\perp) + \frac{\mathbf{k}_\perp \cdot \mathbf{S}_T}{M} g^q_{1T}(x, k_\perp) \tag{6.2}$$

$$\begin{aligned}\frac{1}{2}tr[i\sigma^{j+}\gamma_5\Phi^q_{ij}(x, \mathbf{k}_\perp, \mathbf{S})] = S^j_T h^q_1(x, k_\perp) + S_L\frac{k^j_\perp}{M}h^{\perp q}_{1L}(x, k_\perp) \\ + \frac{(k^j_\perp k^k_\perp - \frac{1}{2}\mathbf{k}^2_\perp\delta^{jk})S^k_T}{M^2}h^{\perp q}_{1T}(x, k_\perp) + \frac{\epsilon^{jk}k^k_\perp}{M}h^{\perp q}_1(x, k_\perp)\end{aligned} \tag{6.3}$$

The gamma structures signal the quark polarisations, γ^+ for unpolarised quarks, $\gamma^+\gamma_5$ for longitudinally polarised quarks and $i\sigma^{j+}\gamma_5$ for transversely polarised quarks with M the mass of the proton. The quark-quark correlator function is a forward matrix of elements of quark fields with explicit Dirac indices i and j in a hadronic state.

Similarly, for the Fragmentation Functions a matrix element called the quark decay function is introduced($\Delta(z, \mathbf{k}^{'}_\perp)$), this is similar to Φ in the PDFs. The arguements of this function are z and the transverse momentum $\mathbf{k}^{'}_\perp = -z\mathbf{k}_\perp$ which is the perpendicular momentum of the hadron h with respect to the quark momentum. Dy Dirac projections the TMD FFS for the nucleon [107] are:

$$\gamma^-\Delta(z, \mathbf{k}^{'}_\perp) = D_1(z, \mathbf{k}^{'2}_\perp) + \frac{\epsilon^{ij}k^i_\perp S^j_T}{M} D^\perp_{1T}(z, k^{'2}_\perp) \tag{6.4}$$

$$\gamma^+\gamma_5\Delta(z, \mathbf{k}^{'}_\perp) = G_{1L}(z, \mathbf{k}^{'}_\perp) \tag{6.5}$$

$$i\sigma^{i-}\gamma_5\Delta(z, \mathbf{k}^{'}_\perp) = S^i_T H_{1T}(z, \mathbf{k}^{'2}_\perp) + \frac{k^i_\perp}{M}H^\perp_{1L}(z, k^{'}_\perp) + \frac{\epsilon^{ij}k_\perp}{M}H^\perp_1(x, \mathbf{k}^{'2}_\perp) \tag{6.6}$$

Appendix B: TMD Fracture Functions

The general expressions for Fracture Functions (M) for unpolarised, longitudinally polarised (Δ) and transversely polarised ($\Delta_T M$) quarks are represented [109]:

$$M = \hat{M} + \frac{\mathbf{P}_{h\perp} \times \mathbf{S}_\perp}{m_h} \hat{M}_T^\perp + \frac{\mathbf{k}_\perp \times \mathbf{S}_\perp}{m_N} \hat{M}_T^\perp + \frac{S_L(\mathbf{k}_\perp \times \mathbf{P}_{h\perp})}{m_N m_h} \hat{M}_L^{\perp h} \tag{6.7}$$

$$\Delta M = S_L \Delta \hat{M}_L + \frac{\mathbf{P}_{h\perp}}{m_h} \Delta \hat{M}_T^h + \frac{\mathbf{k}_\perp}{m_N} \Delta \hat{M}_T^\perp + \frac{\mathbf{k}_\perp \times \mathbf{P}_{h\perp}}{m_N m_h} \Delta \hat{M}^{\perp h} \tag{6.8}$$

$$\begin{aligned} \Delta_T M = S_\perp^i \Delta_T \hat{M}_T + \frac{S_L P_{h\perp}^i}{m_h} \Delta_T \hat{M}_L^h + \frac{S_L k_\perp^i}{m_N} \Delta_T \hat{M}_L^\perp + \frac{(\mathbf{P}_{h\perp} \cdot \mathbf{S}_\perp) P_{h\perp}^i}{m_h^2} \Delta_T \hat{M}_T^{hh} \\ + \frac{(\mathbf{k}_\perp \cdot \mathbf{S}_\perp) k_\perp^i}{m_N^2} \Delta_T \hat{M}_T^{\perp\perp} + \frac{(\mathbf{k}_\perp \cdot \mathbf{S}_\perp) P_{h\perp}^i - (\mathbf{P}_{h\perp} \cdot \mathbf{S}_\perp) k_\perp^i}{m_N m_h} \Delta_T \hat{M}_T^{\perp h} \\ + \frac{\epsilon_\perp^{ij} P_{h\perp j}}{m_h} \Delta_T \hat{M}^h + \frac{\epsilon_\perp^{ij} k_{\perp j}}{m_N} \Delta_T \hat{M}^\perp \end{aligned} \tag{6.9}$$

Appendix C: CLAS acceptance and ϕ coverage

The Λ azithumal angle ($\cos(\phi_\Lambda)$) distribution in Figure 55 (d) highlights a peak at $\phi \approx \pm 180°$ and a dip with almost no detection at $\phi \approx 0°$. This behaviour is entirely due to the CLAS forward hole, producing zero acceptance at low Λ angles. The cross section of the CLAS detector is represented in Figure 24. In this schematic the beam line is exiting the paper. The forward hole of the detector is illustrated by the inner green circle and the maximum θ coverage by the outer black circle. In the SIDIS process, the scattered electron is detected, at some point, by the upper blue dot with the virtual photon at the lower blue dot. These two directions indicate the electron scattering plane, which is perpendicular to the paper and represented by the blue line. The two red dots represent two examples of the intersection of the Λ with the CLAS plane and, together with the virtual photon direction, define the hadron plane. The azimuthal angle ϕ is the angle between the two planes. It is noted that the direction of a Λ produced at $\phi \approx 0°$ is pointing toward the CLAS forward hole. Thus making the probability to detect a Λ impossible. This schematic illustrates the ϕ distribution in Figure C.1.

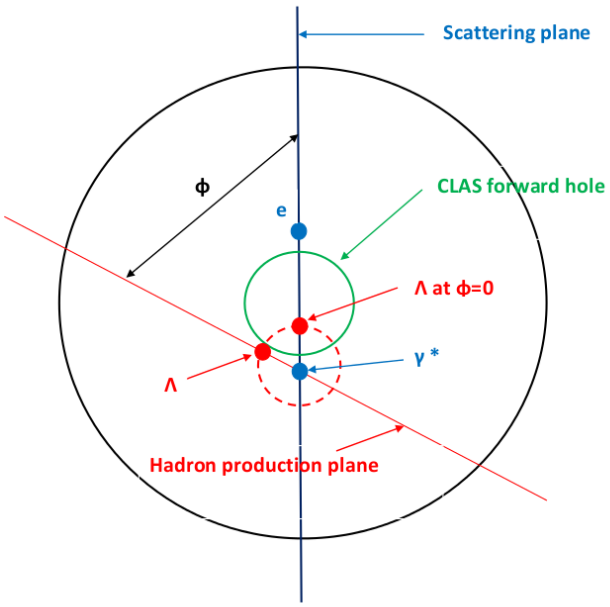

Figure C.1: *Cross section of the CLAS detector. The beam is exiting the paper.*

Appendix D: Transferred Λ Polarisation with other Kinematics for BSA

Appendix D: Invariant mass fits for BSA calculation

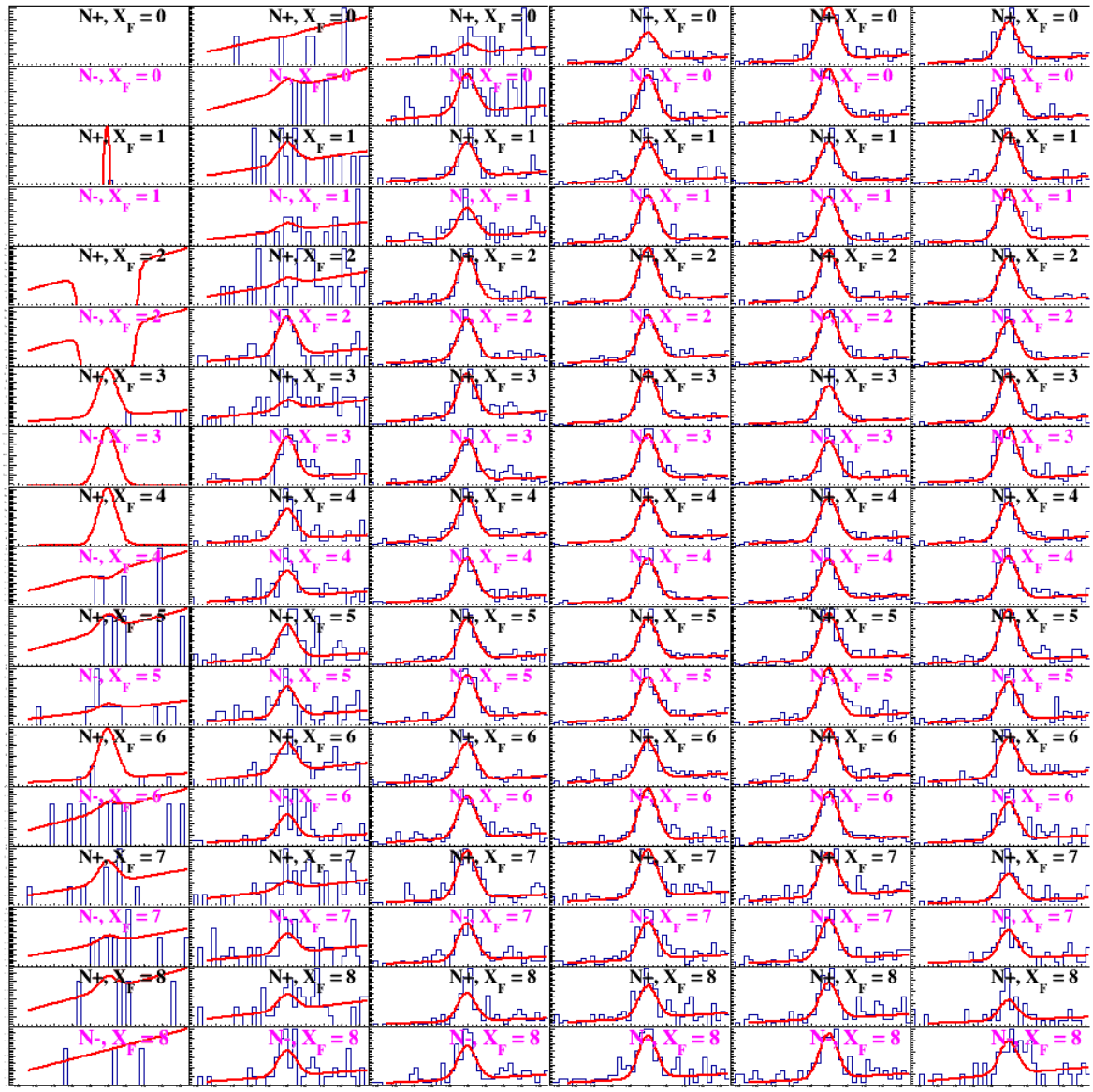

Figure D.1: Λ *invariant mass fit for Asymmetry calculation. This is for all helicities (+ve/-ve) and* x_F *bins (Y-axis) against* $\cos(\theta_p^*)$ *(X-axis). Positive helicities (N+) have the black embedded text, negative (N-) the magenta. Red line illustrates the Gaussian plus 2nd order polynomial fit to extract the signal.*

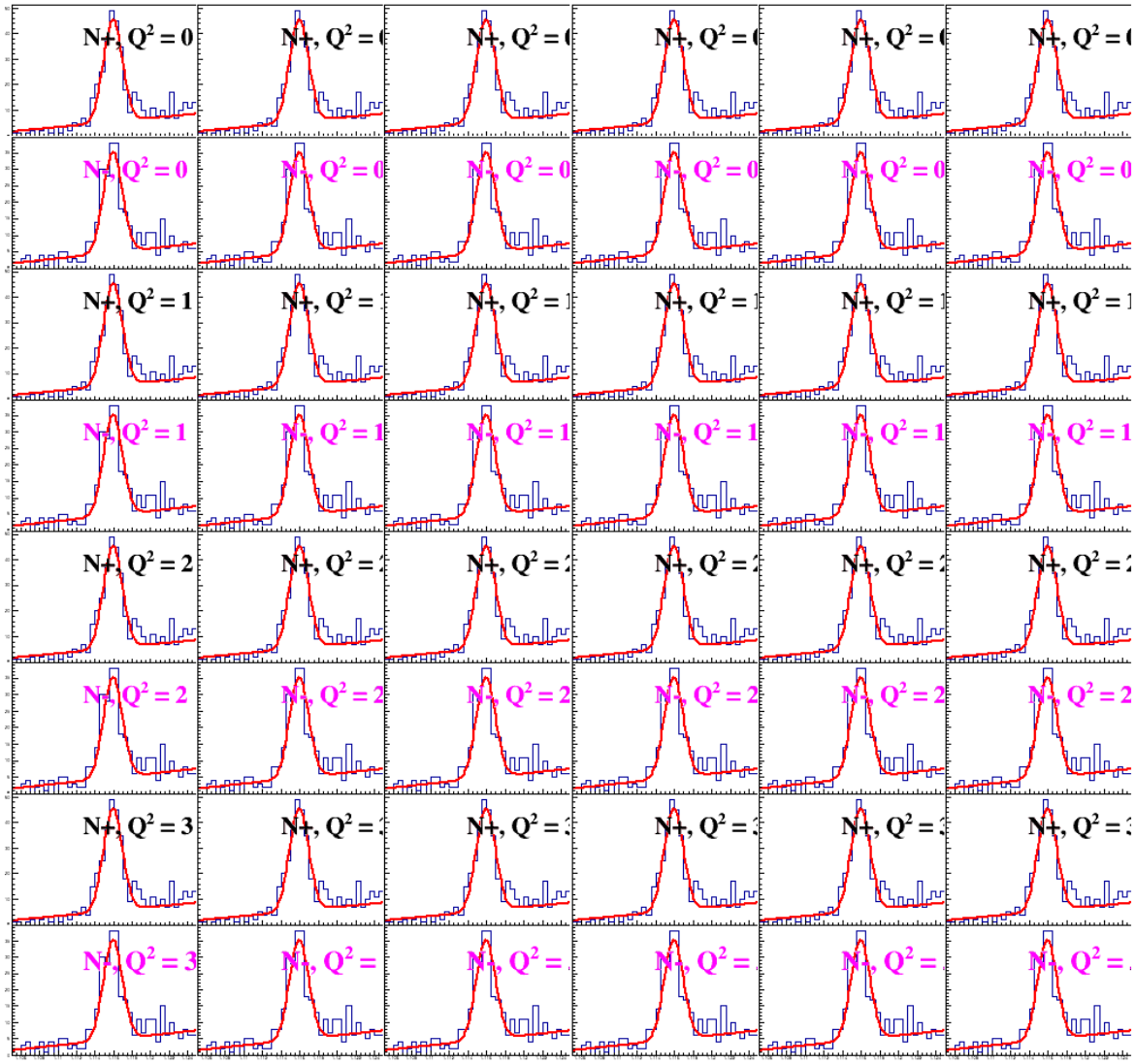

Figure D.2: Λ *invariant mass fit for Asymmetry calculation. This is for all helicities (+ve/-ve) and* Q^2 *bins (Y-axis) against* $\cos(\theta^*_p)$ *(X-axis). Positive helicities (N+) have the black embedded text, negative (N-) the magenta. Red line illustrates the Gaussian plus 2nd order polynomial fit to extract the signal.*

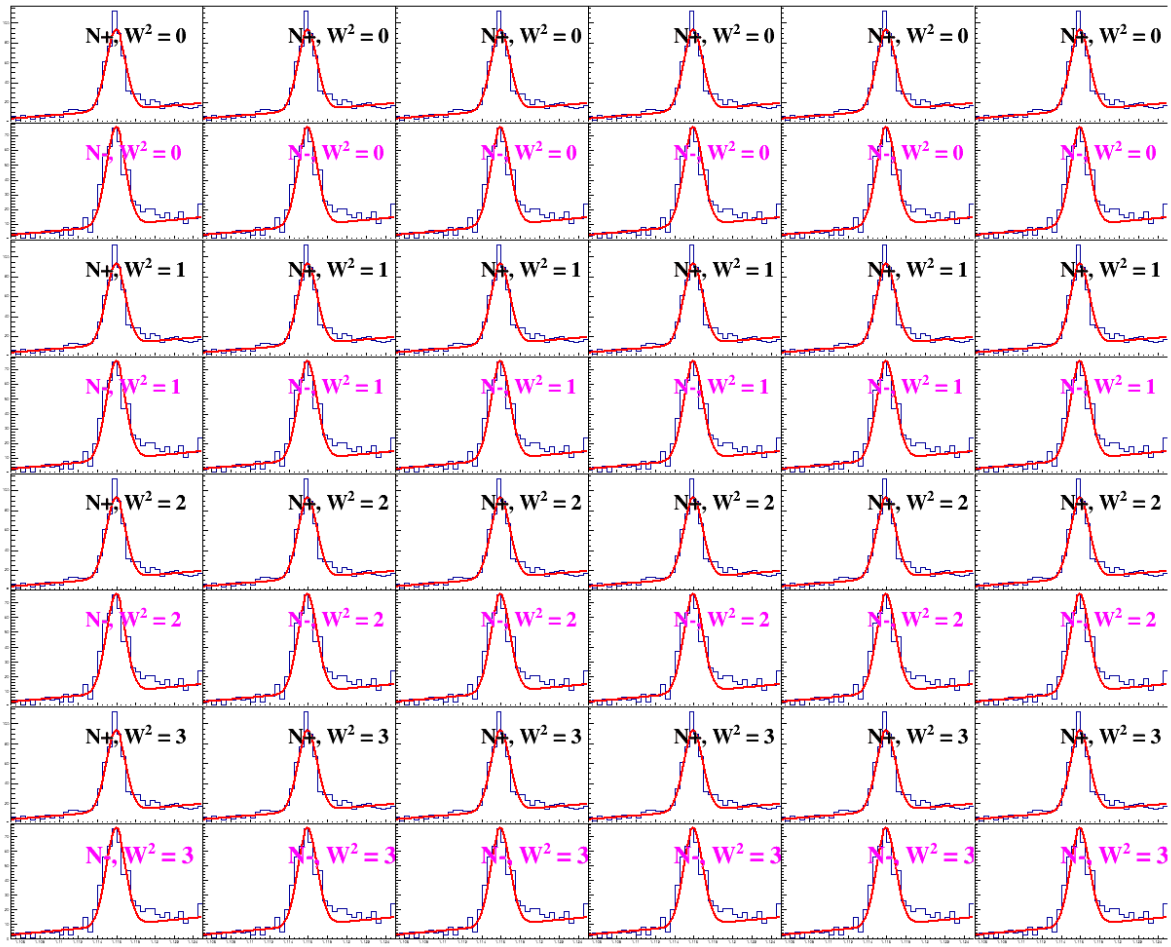

Figure D.3: Λ *invariant mass fit for Asymmetry calculation. This is for all helicities (+ve/-ve) and* W^2 *bins (Y-axis) against* $\cos(\theta_p^*)$ *(X-axis). Positive helicities (N+) have the black embedded text, negative (N-) the magenta. Red line illustrates the Gaussian plus 2nd order polynomial fit to extract the signal.*

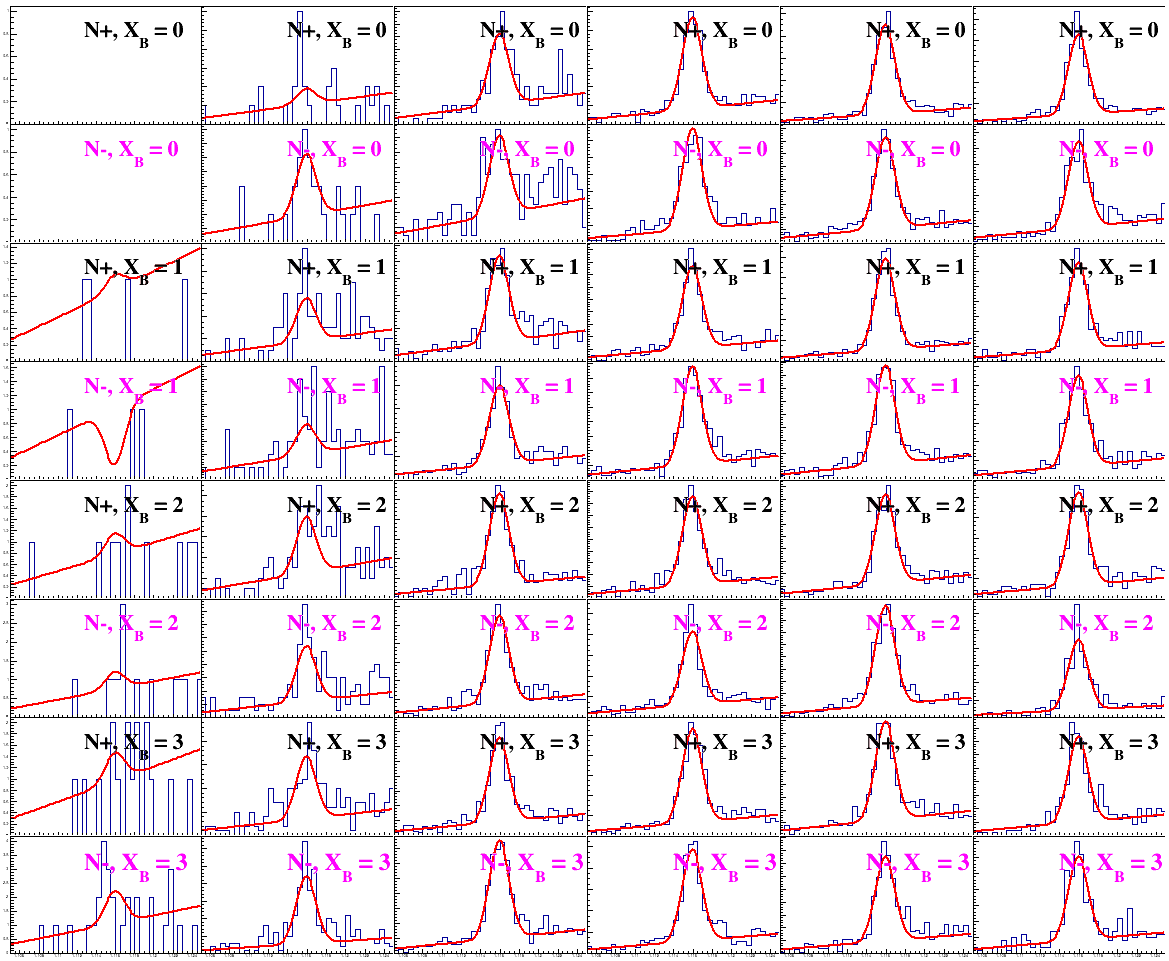

Figure D.4: Λ *invariant mass fit for Asymmetry calculation. This is for all helicities (+ve/-ve) and* x_B *bins (Y-axis) against* $\cos(\theta_p^*)$ *(X-axis). Positive helicities (N+) have the black embedded text, negative (N-) the magenta. Red line illustrates the Gaussian plus 2nd order polynomial fit to extract the signal.*

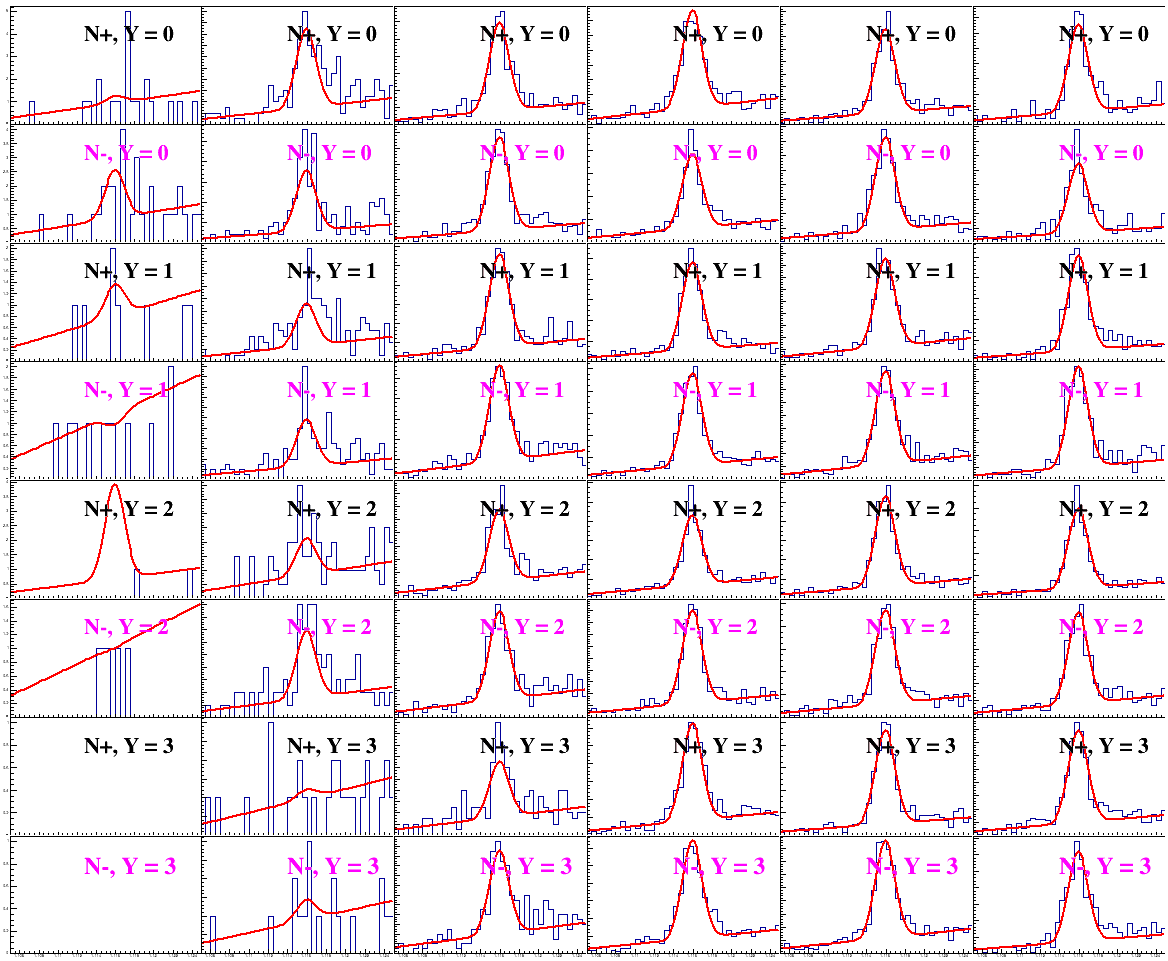

Figure D.5: Λ *invariant mass fit for Asymmetry calculation. This is for all helicities (+ve/-ve) and Y bins (Y-axis) against* $\cos(\theta_p^*)$ *(X-axis). Positive helicities (N+) have the black embedded text, negative (N-) the magenta. Red line illustrates the Gaussian plus 2nd order polynomial fit to extract the signal.*

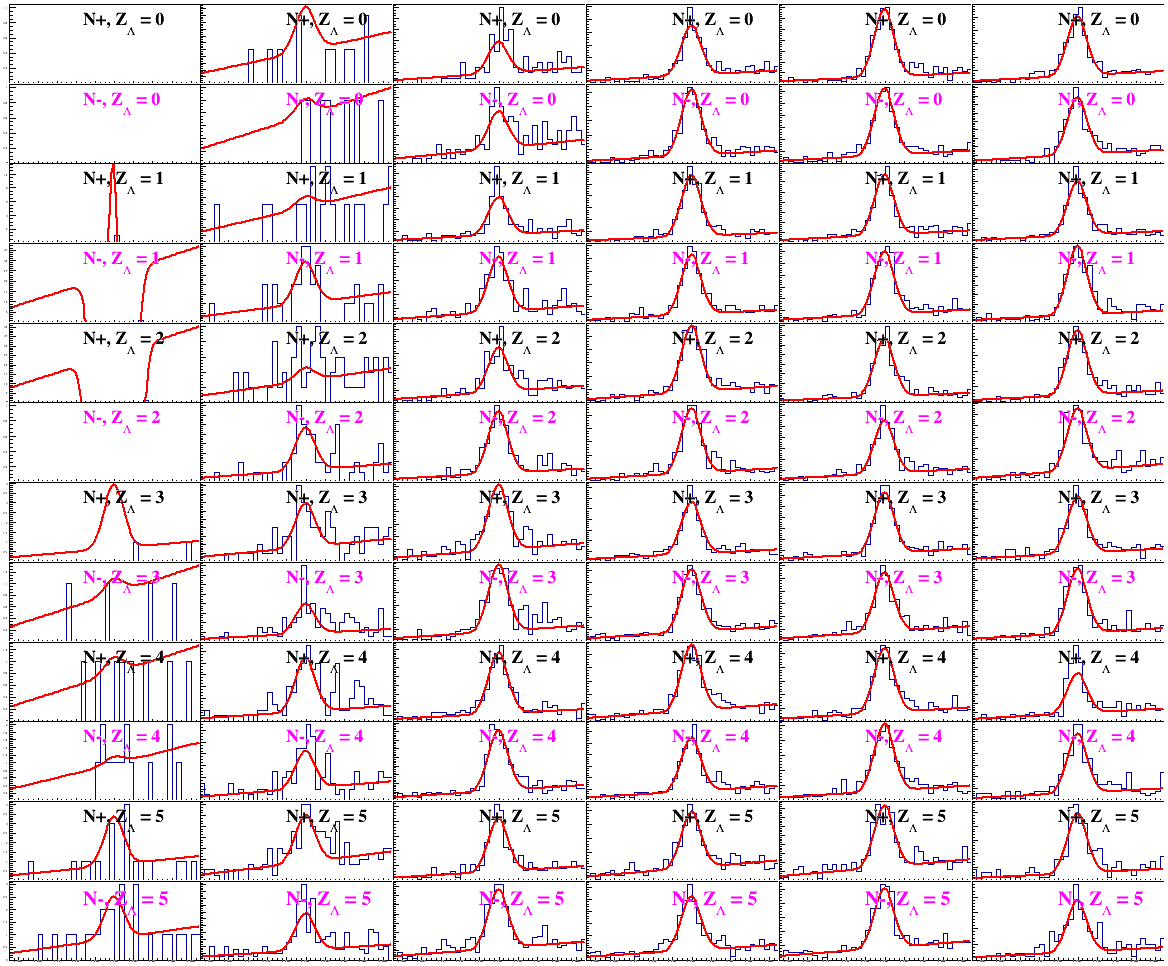

Figure D.6: Λ *invariant mass fit for Asymmetry calculation. This is for all helicities (+ve/-ve) and* Z_Λ *bins (Y-axis) against* $\cos(\theta_p^*)$ *(X-axis). Positive helicities (N+) have the black embedded text, negative (N-) the magenta. Red line illustrates the Gaussian plus 2nd order polynomial fit to extract the signal.*

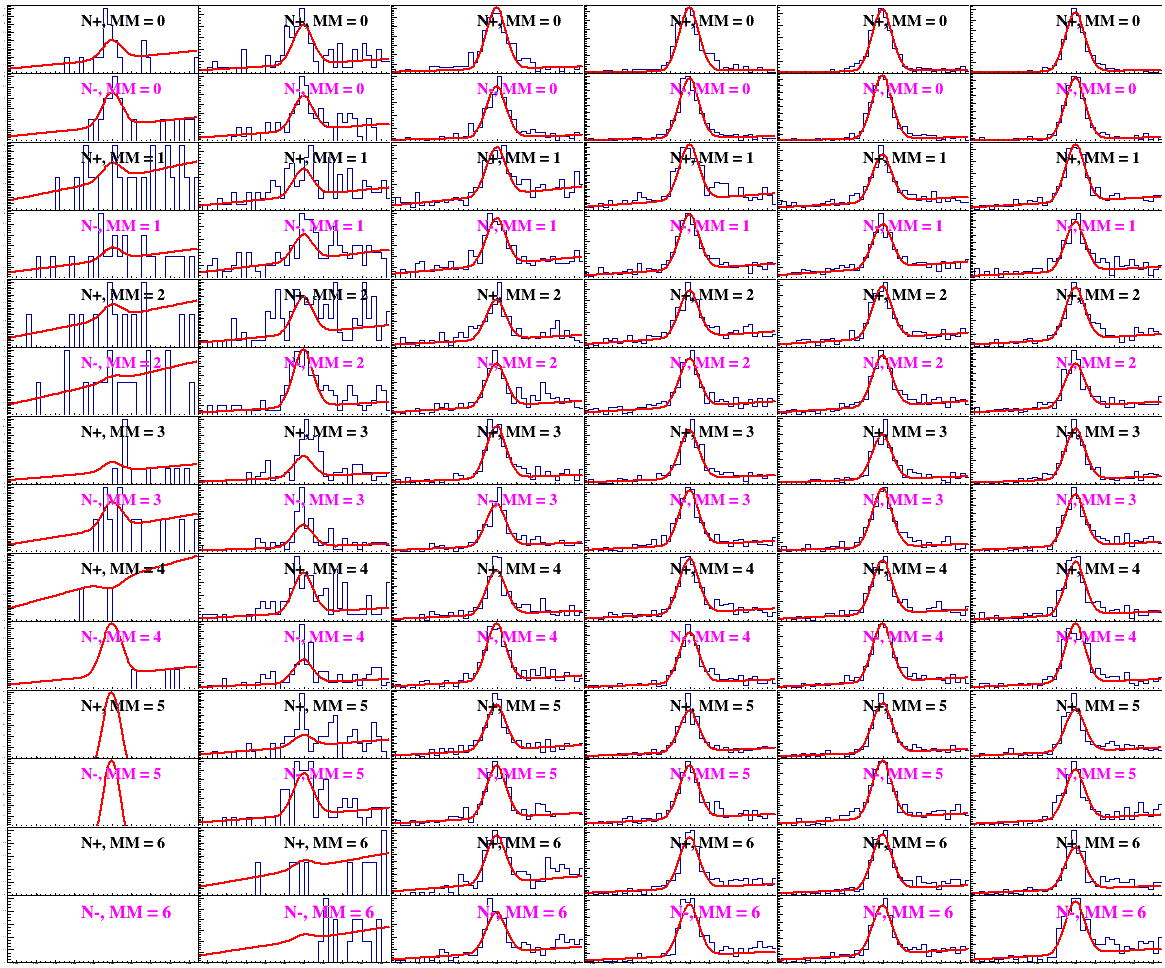

Figure D.7: Λ *invariant mass fit for Asymmetry calculation. This is for all helicities (+ve/-ve) and MM bins (Y-axis) against* $\cos(\theta_p^*)$ *(X-axis). Positive helicities (N+) have the black embedded text, negative (N-) the magenta. Red line illustrates the Gaussian plus 2nd order polynomial fit to extract the signal.*

Appendix D: Binned Asymmetry polarisation extraction

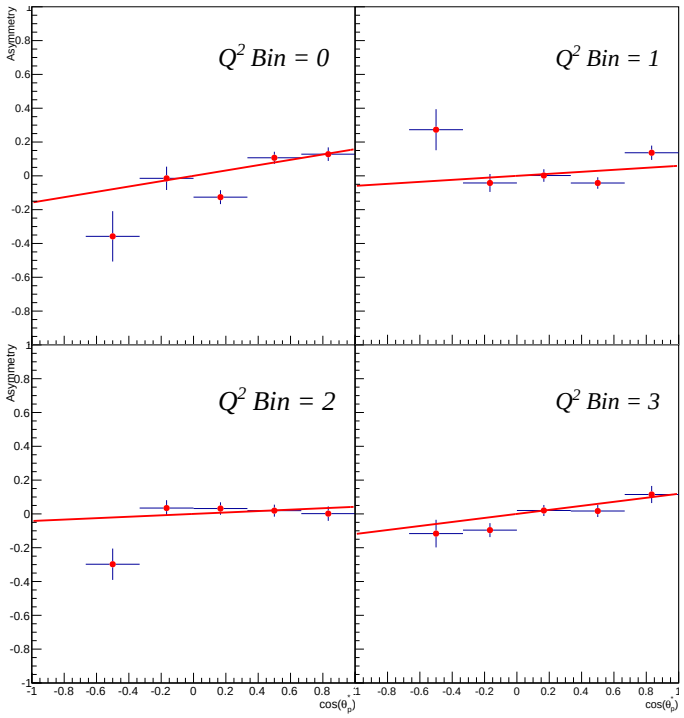

Figure D.8: *Fit of 1st order polynomial to extract P_T or gradient in all Q^2 bins.*

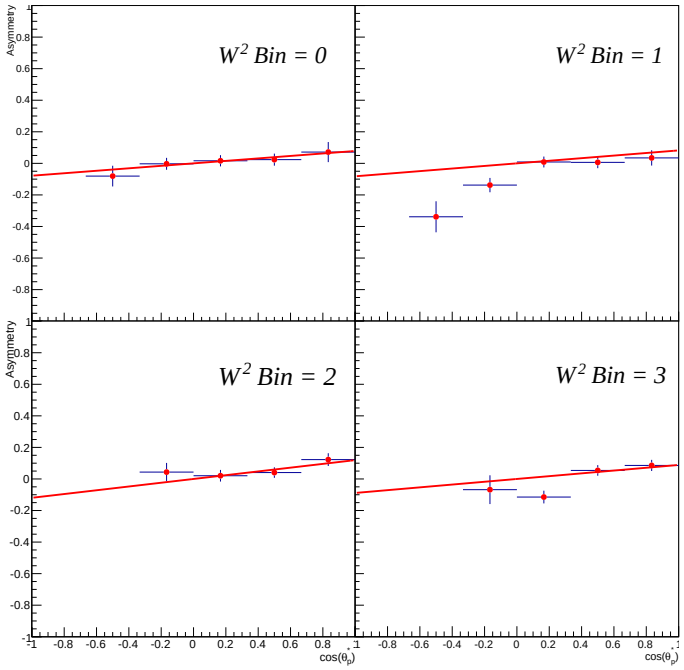

Figure D.9: *Fit of 1st order polynomial to extract P_T or gradient in all W^2 bins.*

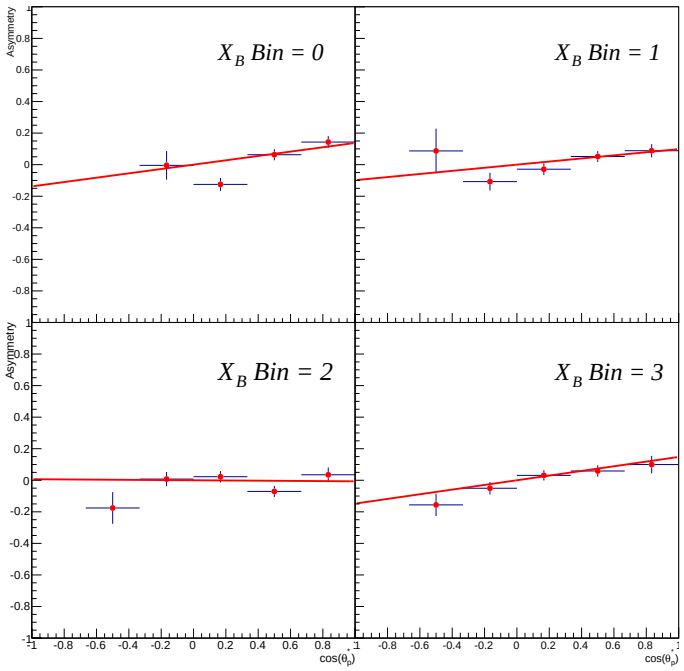

Figure D.10: *Fit of 1st order polynomial to extract P_T or gradient in all x_B bins.*

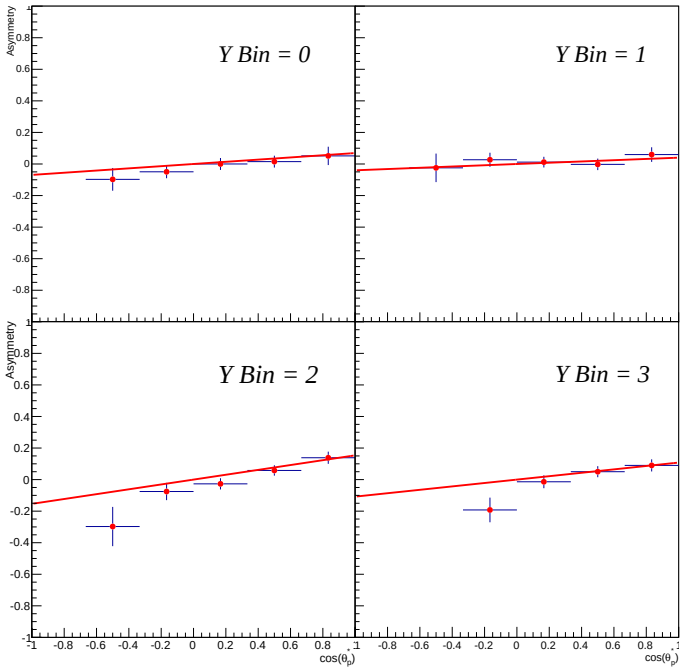

Figure D.11: *Fit of 1st order polynomial to extract P_T or gradient in all Y bins.*

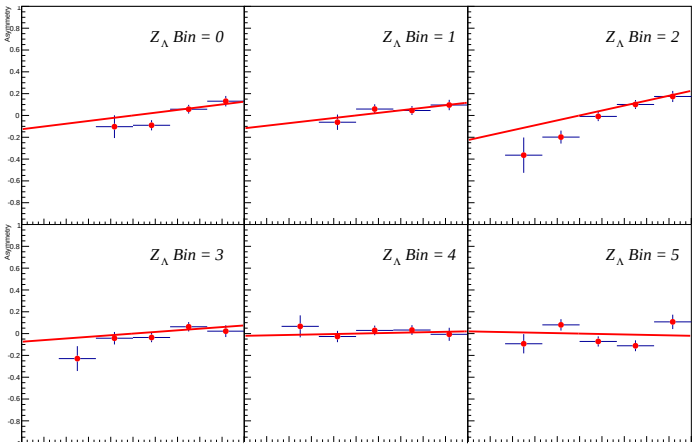

Figure D.12: *Fit of 1st order polynomial to extract P_T or gradient in all Z_Λ bins.*

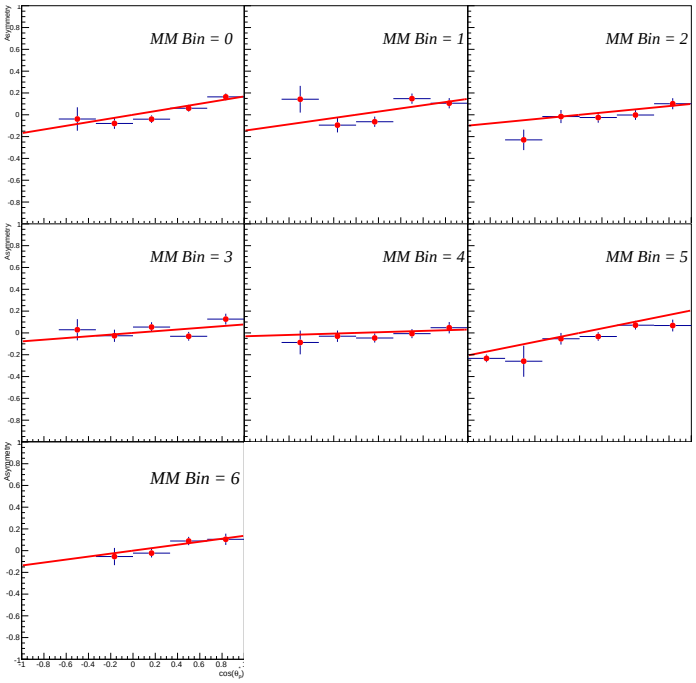

Figure D.13: *Fit of 1st order polynomial to extract P_T or gradient in all MM bins as described by the cuts in Section 5.1.1.*

Appendix D: Final transferred Λ polarisation

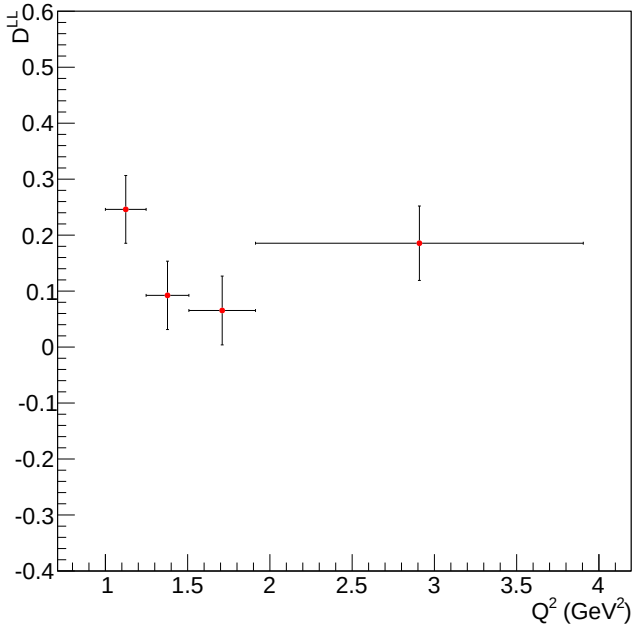

Figure D.14: *Longitudinal transferred Λ polarisation coefficient as a function of Q^2.*

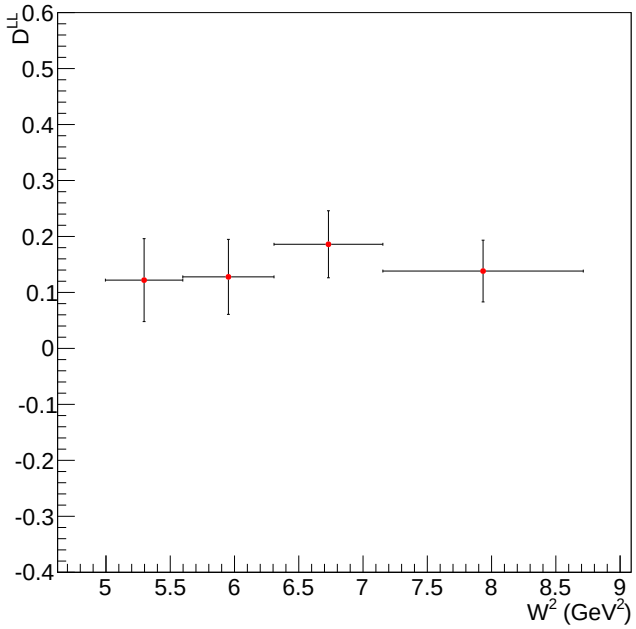

Figure D.15: *Longitudinal transferred Λ polarisation coefficient as a function of W^2.*

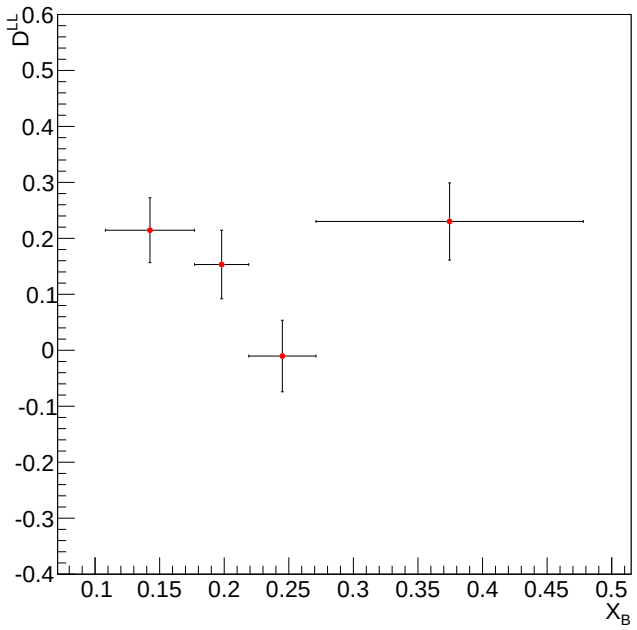

Figure D.16: *Longitudinal transferred* Λ *polarisation coefficient as a function of* x_B.

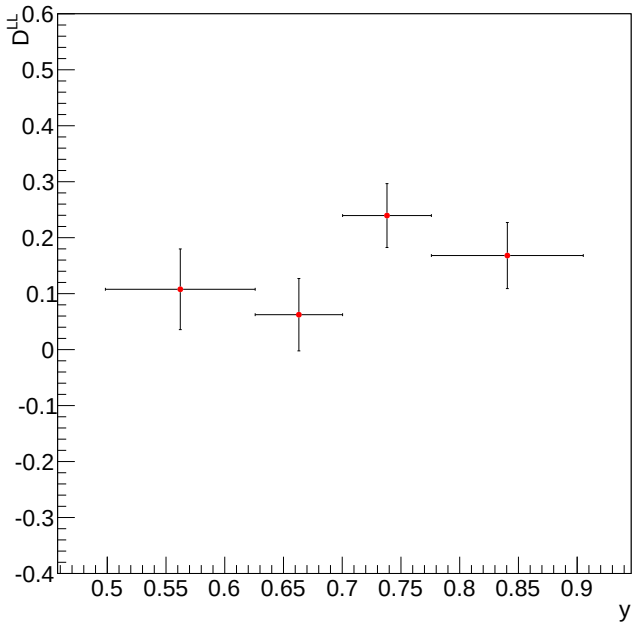

Figure D.17: *Longitudinal transferred* Λ *polarisation coefficient as a function of* y.

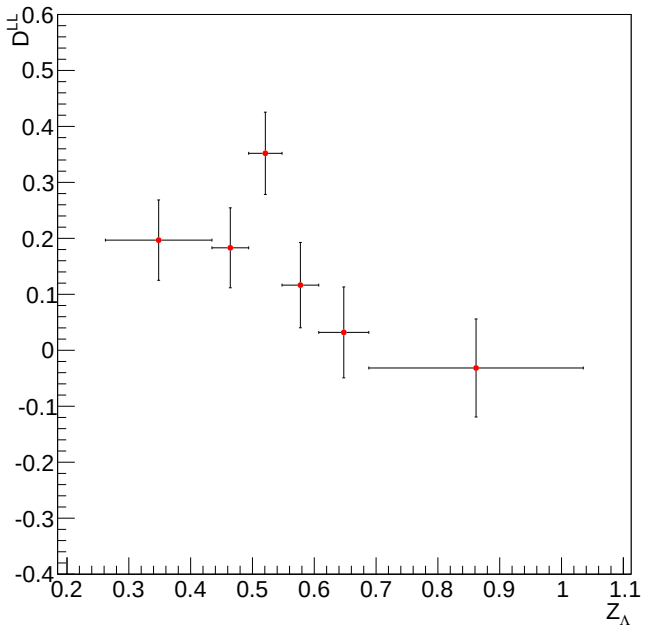

Figure D.18: *Longitudinal transferred* Λ *polarisation coefficient as a function of* Z_Λ.

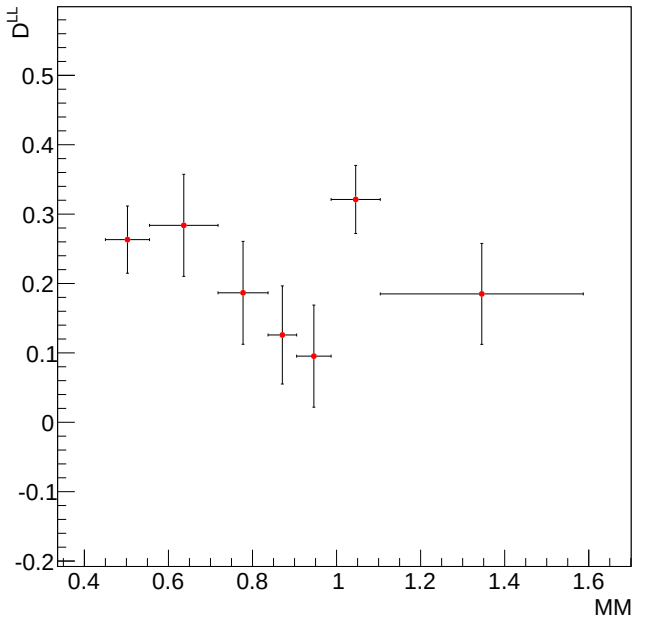

Figure D.19: *Longitudinal transferred* Λ *polarisation coefficient as a function of* MM *as described by the cuts in Section 5.1.1.*

Appendix E: Transferred Λ Polarisation with other Kinematics for MLE

Appendix E: Final transferred Λ polarisation

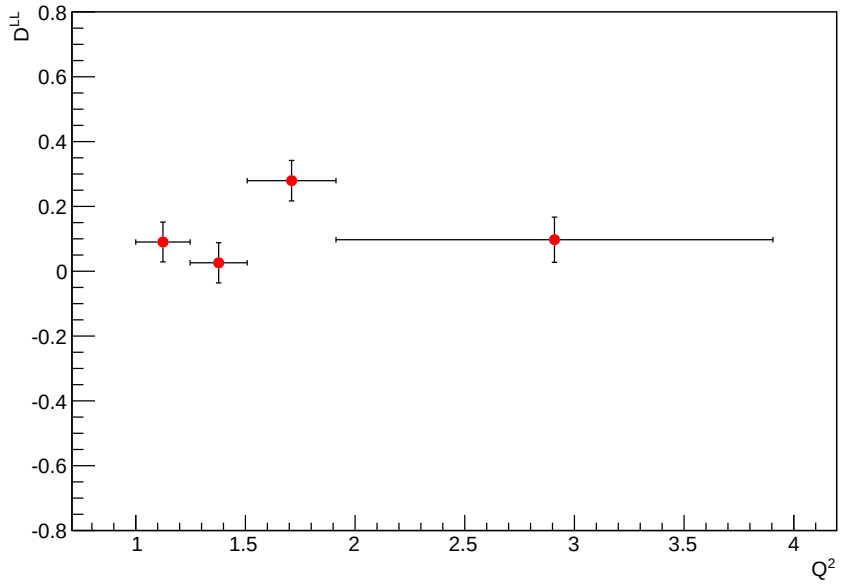

Figure E.1: *Longitudinal transferred* Λ *polarisation coefficient as a function of* Q^2.

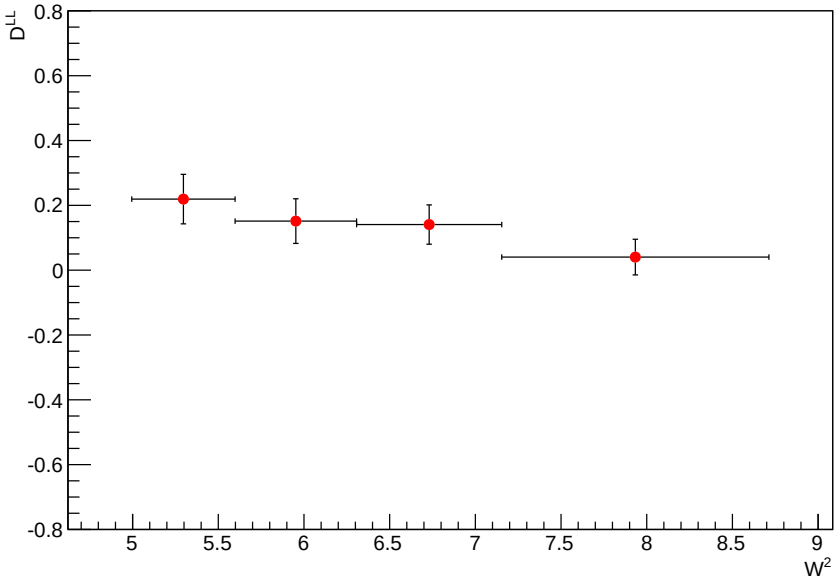

Figure E.2: *Longitudinal transferred* Λ *polarisation coefficient as a function of* W^2.

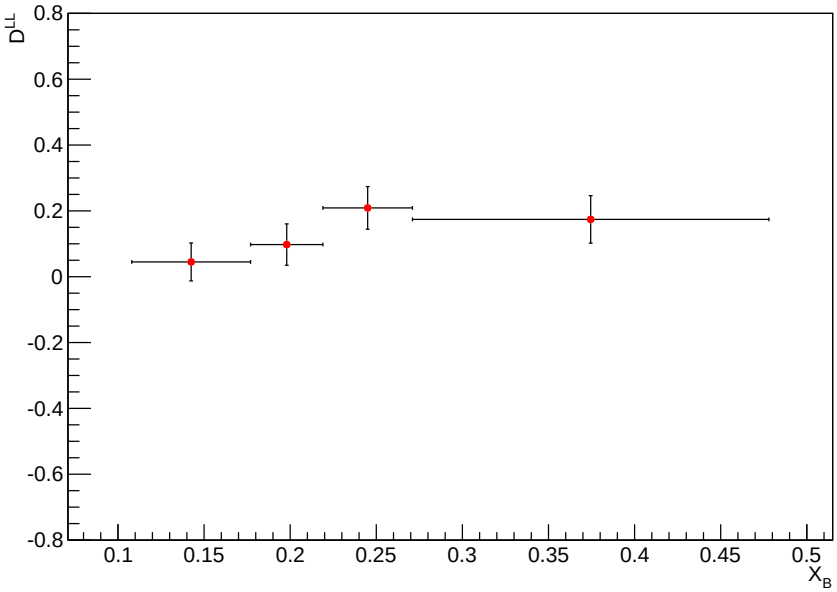

Figure E.3: *Longitudinal transferred* Λ *polarisation coefficient as a function of* x_B.

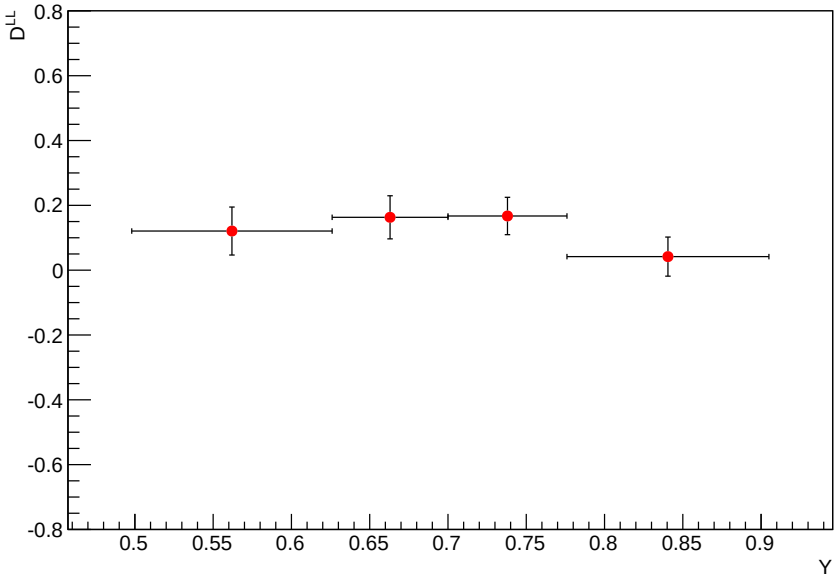

Figure E.4: *Longitudinal transferred* Λ *polarisation coefficient as a function of* y.

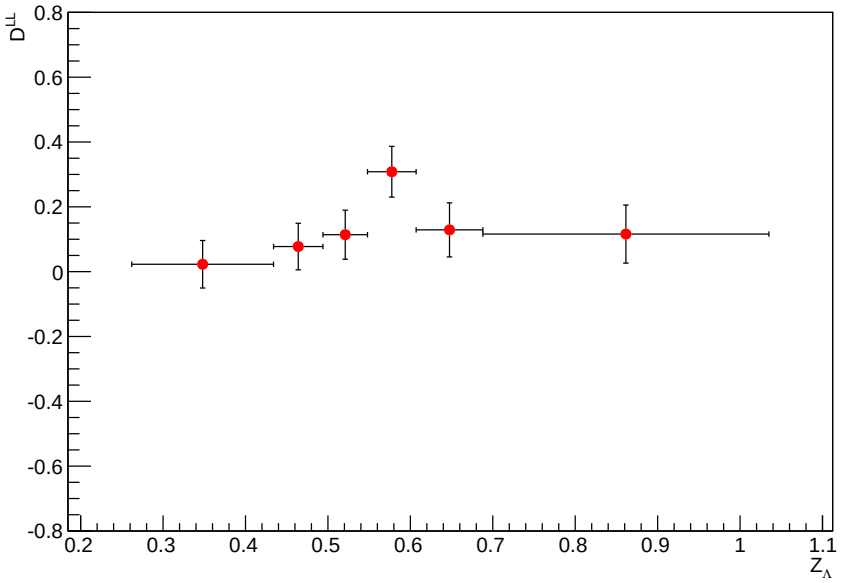

Figure E.5: *Longitudinal transferred* Λ *polarisation coefficient as a function of* Z_Λ.

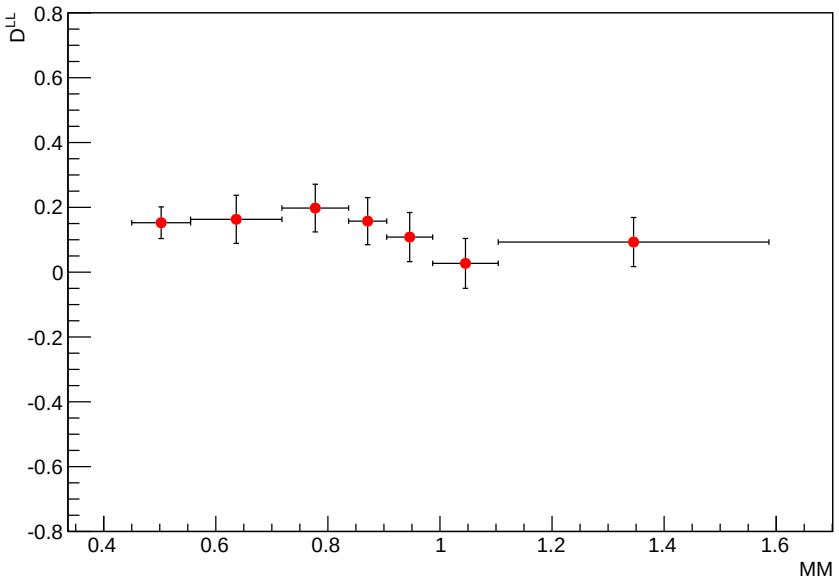

Figure E.6: *Longitudinal transferred* Λ *polarisation coefficient as a function of* MM *as described by the cuts in Section 5.1.1.*

Bibliography

[1] E. Rutherford, The scattering of α and β particles by matter, and the structure of the atom, *Phil. series 6.*, 21(125):669 - 688, 1911.

[2] Physics at the British Association, *Nature*, 106 (2663), pp 357-358 , 1920.

[3] H.E. Anderson, E. Fermi, E.A Long, Total Cross Sections of Positive Pions in Hydrogen, *Phy Rev* , 85, pp 928.

[4] K.A Brueckner, Muon-Nucleon Scattering , *Phy Rev* , 86, pp 106.

[5] M. Gell-mann and Y. Ne'eman, The eightfold way, *Prog Theoret Phys*, 27 (1962:949-966).

[6] G. Zweig, An SU_3 model for strong interaction symmetry and its breaking, *No Cern*, 412, CM-D00047884.

[7] S. Narison, QCD as a theory of hadrons from partons to confinement, *Cam Phy Press* , vol 17.

[8] D.J. Gross, E. Wilnek, Ultra violet behaviour of non-abelian gauage theories, *Phy Rev Lett*, 30, pp 1346 - 1396.

[9] R. Hoftstader and R McAllister, *Phy Rev*, 98, 217, 1955.

[10] M.K. Jones et al, G_E/G_M Ratio by polarization Transfer in $ep \rightarrow ep$, *Phy Rev Lett*, 84: 1398-1402, 2000.

[11] D. Bayor et al, Measurements of the elastic electromagnetic form factor ratio with polarization transfer, *Phy Rev C*, 64: 038202, 2001.

[12] O. Gayou et al, Measurements of G_{E_p}/G_{M_p} in $ep \rightarrow ep$ to $Q^2 = 5.6(GeV)$, *Phy Rev Lett*, 88: 092301, 2002.

[13] B. Milbrath et al, *Phy Rev Lett*, 80, 452 (1998).

[14] C.F. Perdrisat, V. Panjabi, M. Vanderhaeghen, Nucleon Electromagentic Form Factors, *Arxiv: hep-ph*, 0612014, 2007.

[15] L.W. Mo and Yun-Su Tsui, Radiative corrections to Elastic and Inelastic ep and up scattering, *Rev. Mod Phys*, 41, 205, 1969.

[16] L.I. Maximon and J.A Tjon, Radiative corrections to electron proton scattering, *Phys Rev C*, 62, 054320, 2000.

[17] P.G. Blunden, M. Melnilchouk and J.A Tjon, Two photon exchange and elastic electron-proton scattering, *Phys Rev C*, 72, 034612, 2005.

[18] P.A.M. Guchon and M. Vanderhaegen, How to reconcile the Rosenbluth and polarisation transfer method in a measurement of the proton form factors, *Phys Rev Lett*, 91, 142303, 2003.

[19] A.V. Aranasev, S.J. Brodsky et al, Two photon exchange contribution to elastic eletron-nucleon scattering at large momentum transfer, *Phys Rev D*, 72, 013098, 2005.

[20] J.D. Bjorken, Asymptotic sum rules at infinite momentum, *Phys Rev* , 179, pp 1547 - 1553, 1969.

[21] T. Gehrmann and W.J. Stirling, Spin-dependent parton distributions from polarised structure function data, *Phys ReV C*, 65, pp 461 - 470, 1995.

[22] J.Beringer et al, Review of Particle Physics, *Phys Rev D*, 86:010001, 2012.

[23] NA48 collaboration, A. Lai, P. Marras, Measurement of k^0_{e3} Form Factors, *Phys Lett B*, 604, pp 1-10, 2004.

[24] A.S Leuchenko et al, *Phys at Nucl*, 65, 2002.

[25] A.A akimenko et al, *Phys Lett B*, 259, 1991.

[26] V. Lingliano et al, *Eur Phys J.C*, 35 (2004) 53.

[27] J. Ashman et al, A measurement of the spin asymmetry and determination of the structure function g_1 in deep inelastic muon-proton scattering, *Phys. Lett. B.*, 206:364-370, 1988.

[28] A. Airapetian et al, Precise determination of the spin stucture function g_1 of the proton,deuteron and neutron, *Phys. Rev. D*, 75:012007, 2007.

[29] A.Airapetian et al, Single-spin asymmetries in semi-inclusive deep-inelastic scattering on a transversely polarized hydrogen target, *Phys. Rev. Lett.*, 94:012002, 2005.

[30] R. Jaffe and A. Manohar, *Nucl. Phys. B*, 337, 1990.

[31] D. de Florian, R. Sassot, M. Stratman and W. Vogelsang, *Phys. Rev. Lett*, 101, 072001, 2008.

[32] R.D Ball, S. Forte et al, *Nucl. Phys. B*, 874, 36(2013).

[33] E.C Aschenauer et al, *arxiv:1304.0079.*

[34] G. Agakishieu et al, *Eur. Phys. J. A*, 50, 81 (2004).

[35] E.P Wigner, *Phys. Rev.*, 40, 749 (1932).

[36] M. Burkardt, Impact parameter Dependent Parton Distributions and Off-Forward Parton Distributions for $\zeta \to 0$, *Phys. Rev. D*, 62:071503, 2000.

[37] E.P Wigner, On the Quantum correction for Thermodynamic Equilibrium, *Phys. Rev.*, 40:749-759, 1932.

[38] C. Lorce, B. Pasquini and M. Vanderhaeghen, *JHEP.*, 05, 041 (2011), 11024704.

[39] S. Meissner, A. Metz, M. Schlegal and K. Goeke, Generalized parton correlation functions for a spin-0 hadron, *JHEP.*, 0808, 038, 2008.

[40] A. Bacchetta et al, Semi Inclusive Scattering at small tranverse momentum, *JHEP.*, 02:093, 2007.

[41] C. Lorce, B. Pasquini and M. Vanderhaeghen, United framework for generalized and transverse momentum dependent parton distributions within a 3Q light-cone picture of the hadron . *JHEP*, 05, pp 1-40, 2012.

[42] J.I. Friedman and H.W. Kendall, Deep inelastic electron scattering, *Ann. Rev. Nucl. Part. Sci*, 22, pp. 203 - 254, 1972.

[43] G. Parsi and R. Petronzio, On the breaking of Bjorken Scaling, *Phys. Lett. B.*, 62, 1976.

[44] A.W. Thomas and W. Weise, The structure of the nucleon, *Wiley*, 2001.

[45] M. Anselmino, M.Boglione, U. D'Alesio, A. Kotzinian, F. Murgia and A. Prokudin, *Phys. Rev. D*, 75, 054032, 2007.

[46] M. Anselmino, M.Boglione, U. D'Alesio, S. Melis, F. Murgia, E. Npcera and A. Prokudin, *Phys. Rev. D*, 83, 114019, 2011.

[47] G. knochlein, D. Drechsel and L.Tiator, Phys. Rev. A.353, 115 (1995).

[48] V. Barone, F. Bradamante, A. Martin, Nucl. Phys. Rev, 66, 267 (2010).

[49] A. Anselmino, V. Barone and A. Kotzinian, *Phys. Lett. B.*, 699, 108(2011).

[50] L. Trentadue and G. Veneziano, *Phys. Lett. B*, 323, 201 (1994).

[51] F.A. Ceccopieri and L. Trentadue, *Phys. Lett. B.*,310 (2006).

[52] D. Sivers, Single-spin production asymmetries from the hard scattering of pointlike constituents, *Phy. Rev. D.*, 41(1):83-90, January 1990.

[53] J.C. Collins, Fragmentation of transversely polarized quarks probed in transverse momentum distribtions, *Nucl. Phys. B.*, 396:161-182, 1993.

[54] A. Anselmino, V. Barone and A. Kotzinian, *Phys. Lett. B.*, 706, 46 (2012).

[55] J.Ellis, D.E. Kharzeev and A. Kotzinian, On the breaking of Bjorken Scaling, *Phys. Lett. B.*, 69, 467 (1996).

[56] W. Melnitchouk and A.W Thomas, *Phys. Lett. A.*, 353, 311 (1996).

[57] R. Jaffe, Polarized $\Lambda's$ in the Current Fragmenation Region, *Phys. Rev.*, p54, 6581 (1996).

[58] EMC Collaboration (M.Arneado et al), *Phys. Lett. D.*, 150, 458 (1985).

[59] D.S. Carman, K. Loo, L.kramer and B. Raue. *JLab Proposal. E*, pp99-006.

[60] P. Astier et al, *Nucl. Phys. B.*, 605, 3 (2001).

[61] M.R. Adams et al, *Eur. Phys. C.*, 263 (2000).

[62] A. Airapetian et al, *Phys. Rev. D.*, 74, 072004 (2006).

[63] M. Alekseev et al, *Eur. Phys. C.*, 64, 171 (2009).

[64] M. Mirazita, http://www.jlab.org/Hall-B, 1994

[65] M. Amarian, et al, The CLAS forward electromagnetic calorimeter, *NIM A*, 2001.

[66] B.A. Mecking ey al, The CEBAF large acceptance spectrometer (CLAS), *NIM A*, 503, pp513-553, 2003.

[67] E. Anciant et al, Tagger hit reconstruction software and tagger calibration overview, *CLAS-note*, 1999-04, 1999.

[68] M. Mestayer et al, *NIM A*, 449, 81 (2000).

[69] G. Adams et al, *NIM A*,465, 414 (2001).

[70] G. Adams et al The CLAS Cherenkov detector, *NIM A*, 465, pp414-427, 2001.

[71] E. Smith et al, *NIM A*, 432, 265 (1999).

[72] M. Amarian et al, *NIM A*,460, 239 (2001).

[73] J.J. Manak, E.S. Smith, S. McAleer et al, e1, g1 and g6 Data Processing Procedures, *CLAS-Note, JLab* ,60, pp 1909-016.

[74] http://www.jlab.org/Hall-B/mss/clas/e1f/production/pass2/v1/root/e/.

[75] M. Mirazita, Semi-inclusive Λ electroproduction with e1f data set, *CLAS Note*, 2011.

[76] CERN, library, Geant detector description and simulation tool, http://www.asd.web.cern.ch/wwwasd/geant/.

[77] E. Wolin, http://www.jlab.org/HallB/document/gsim/userguide.html, 1996.

[78] S. Seema, EC Geometrical Fiducial Cuts, private communication.

[79] Bad SC paddles, private communication.

[80] S. Stepanyan, Subroutine EC-fid-46, private communication.

[81] W. Gohn, Probing the Proton's Quark Dynamics in Semi-Inclusive Pion Electroproduction, *JLAB-E*, 99-006, 2012.

[82] P. Khetarpal et al, Near-threshold neutral pion electroproduction at high momentum transfers and generalized form factors, *Phys. Rev. C*, 87, 045205, 2013.

[83] K. Egigan, Determination of the electron energy cut due to the CLAS EC threshold, *CLAS-Note*, 99-007 (1999).

[84] D. Carmin, Hyperon Electroproduction at CLAS: Polarization Transfer in the reactions at 6 GeV, *CLAS-Note*,E00-112, 2007.

[85] M. Mirazita, Energy Loss Corrections, http://www.jlab.org/Hall-B/secure/e1f/mirazita/eloss, 2006.

[86] M. Mirazita, Momentum Corrections, http://www.jlab.org/Hall-B/secure/e1f/mirazita/momcorr, 2006.

[87] H. Avakian, http://www.jlab.org/ avakian/tmp/clasdid$_2$010.$january.tar.gz$, 2006.

[88] T. Sjostrand, Pythia and JETSET Physics Manual, *arxiv:hep-ph*, 9508391.

[89] http://www.jlab.org/Hall-B/infn2/lhows/GSIM/bin/LinuxRHFC8/gsim.

[90] http://www.jlab.org/Hall-B/group/clasbuilds/release-f8-1/bin/LinuxRHFC8/gpp.

[91] S. Gohn http://www.jlab.org/ Gohn/bin/user$_a na_p ass1_f c8$.

[92] G. Gabrielyan et al, Measurement of the induced polarization of Lambda(1116) in kaon electroproduction with CLAS, *JLAB-PHY*, 09-1104, 2010.

[93] C. Caso et al, Eur. Phys. J. C, 3, 1993.

[94] R.J. Barlow, Statistics: A guide to the use of statistical methods in the physical science, *Wiley*, pp81-90, 1989.

[95] J.H. Pollard, Numerical and statistical techniques, *Cam. Uni. Press*, pp211.

[96] R.J. Barlow, Extended Maximum Likelihood, *NIM. A*, 297(3), pp496-508, 10.

[97] Root Manual:TMinuit (online), http://root.cern.ch/root/html/TMinuit.

[98] L. Pappalardo, Private communication.

[99] T. Hauschild and M.Jentschel et al, Comparison of maximum likelihood estimation and chi-square statistcsapplied to counting experiments, *NIM A*, 457, pp384-401, 2001.

[100] J. Ellis, A. Kotzinian, D. Naumou and M. Supozhnikov, *Eur. Phys. J. C*, 52283, 2007.

[101] T. Sjostrand, *Comput. Phys. Commun*, 39, 347, 1986.

[102] T. Sjostrand, *Comput. Phys. Commun*, 39, 367, 1987..

[103] A. Edin, G. Ingelman, J. Rathsman, *Comput. Phys. Commun*, 101, 108, 1997..

[104] H. Plothow-Besch,, *PDFLIN*, w5051, 2000.

[105] U.D Alessio, TMDs universality and factorization, arxiv:1151.5995v1 (hep-ph)), 2011.

[106] A. Kotzinian, Nuc. Phys. B., 441, 234 (1995).

[107] P. Moulders and R. Tangerman, Nuc. Phys. B., 461, 197 (1996).

[108] D. Boer and P. Moulders, Phys. Rev. D., 57, 5780 (1998).

[109] M. Anselmino, V. Barone and A.Kotzinian, Phys. Lett. B., 699, 108 (2011).

[110] M. Mirazita, H. Avakian, J. Phillips et al, *JLab Proposal*, E12-06-11A/E12-09-008A.

[111] V. Burket, CLAS12 and its science program at the Jefferson Lab Upgrade. *Arxiv: hep-ph*, 0810.4718v1, 2008.

[112] M. Contalbrigo, E. Cisbani, P. Rossi et al, The CLAS12 large are RICH detector, *NIM A*, 639, pp302-306, 2011.